

*Russian Original Vol. 54, No. 3, March, 1983*

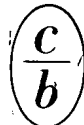
September, 1983

44  
707  
AER  
SATEAZ 54(3) 165-242 (1983)  
File

# SOVIET ATOMIC ENERGY

АТОМНАЯ ЭНЕРГИЯ  
(АТОМНАЯ ЭНЕРГИЯ)

TRANSLATED FROM RUSSIAN



CONSULTANTS BUREAU, NEW YORK

# SOVIET ATOMIC ENERGY

*Soviet Atomic Energy* is abstracted or indexed in *Chemical Abstracts*, *Chemical Titles*, *Pollution Abstracts*, *Science Research Abstracts*, *Parts A and B*, *Safety Science Abstracts Journal*, *Current Contents*, *Energy Research Abstracts*, and *Engineering Index*.

*Soviet Atomic Energy* is a translation of *Atomnaya Energiya*, a publication of the Academy of Sciences of the USSR.

An agreement with the Copyright Agency of the USSR (VAAP) makes available both advance copies of the Russian journal and original glossy photographs and artwork. This serves to decrease the necessary time lag between publication of the original and publication of the translation and helps to improve the quality of the latter. The translation began with the first issue of the Russian journal.

## Editorial Board of *Atomnaya Energiya*:

**Editor:** O. D. Kazachkovskii

**Associate Editors:** N. A. Vlasov and N. N. Ponomarev-Stepnoi

**Secretary:** A. I. Artemov

I. N. Golovin	V. V. Matveev
V. I. Il'ichev	I. D. Morokhov
V. F. Kalinin	A. A. Naumov
P. L. Kirillov	A. S. Nikiforov
Yu. I. Koryakin	A. S. Shtan'
E. V. Kulov	B. A. Sidorenko
B. N. Laskorin	M. F. Troyanov

E. I. Vorob'ev

Copyright © 1983, Plenum Publishing Corporation. *Soviet Atomic Energy* participates in the program of Copyright Clearance Center, Inc. The appearance of a code line at the bottom of the first page of an article in this journal indicates the copyright owner's consent that copies of the article may be made for personal or internal use. However, this consent is given on the condition that the copier pay the stated per-copy fee through the Copyright Clearance Center, Inc. for all copying not explicitly permitted by Sections 107 or 108 of the U.S. Copyright Law. It does not extend to other kinds of copying, such as copying for general distribution, for advertising or promotional purposes, for creating new collective works, or for resale, nor to the reprinting of figures, tables, and text excerpts.

Consultants Bureau journals appear about six months after the publication of the original Russian issue. For bibliographic accuracy, the English issue published by Consultants Bureau carries the same number and date as the original Russian from which it was translated. For example, a Russian issue published in December will appear in a Consultants Bureau English translation about the following June, but the translation issue will carry the December date. When ordering any volume or particular issue of a Consultants Bureau journal, please specify the date and, where applicable, the volume and issue numbers of the original Russian. The material you will receive will be a translation of that Russian volume or issue.

Subscription (2 volumes per year)

Vols. 52 & 53: \$440 (domestic); \$489 (foreign)

Single Issue: \$100

Vols. 54 & 55: \$500 (domestic); \$555 (foreign)

Single Article: \$7.50

## CONSULTANTS BUREAU, NEW YORK AND LONDON



233 Spring Street  
New York, New York 10013

Published monthly. Second-class postage paid at Jamaica, New York 11431.

Mailed in the USA by Publications Expediting, Inc., 200 Meacham Avenue, Elmont, NY 11003.

**POSTMASTER:** Send address changes to *Soviet Atomic Energy*, Plenum Publishing Corporation, 233 Spring Street, New York, NY 10013.

# SOVIET ATOMIC ENERGY

A translation of *Atomnaya Énergiya*

September, 1983

Volume 54, Number 3

March, 1983

## CONTENTS

	Engl./Russ.	
<b>ARTICLES</b>		
Operating Experience with the VVÉR-1000 Reactor Fuel-Element Assemblies of the Fifth Unit of the Novovoronezh Nuclear Power Station - Yu. V. Vikhorev, V. A. Voznesenskii, V. V. Goncharov, K. P. Dubrovin, V. N. Proselkov, V. A. Sidorenko, V. N. Siryapin, N. L. Fatieva, and N. S. Fil' . . . . .	165	163
Use of the Thermal Coolant Noise in Flow Rate Measurement for RBMK Channels - V. M. Selivanov, N. P. Karlov, A. D. Martynov, V. V. Prostyakov, B. V. Lysikov, B. A. Kuznetsov (USSR), D. Pallagy, S. Horany, T. Hargitai, and S. Toszer (Hungary) . . . . .	169	166
Acoustic Effects from Water Leaking into Sodium - V. S. Yugai, R. F. Masagutov, and F. A. Kozlov . . . . .	173	170
Features of the Behavior of the Boundary Regions of Interchannel Pulsations - V. N. Komysnyi, Yu. N. Kornienko, B. I. Kulikov, V. M. Selivanov, O. A. Sudnitsyn, V. I. Sharypin, and A. N. Yarkin . . . . .	178	173
Asymptotic Expansion of the Solution of Kinetic Equations for Slowly Varying Reactivity - A. A. Shepelenko . . . . .	181	175
Reversible Reduction in the Shear Moduli of Iron Alloys during Irradiation - É. U. Grinik and V. S. Karasev . . . . .	184	177
Mechanism of the Tubular Diffusion of Helium - A. V. Subbotin . . . . .	187	179
Atomization of Gold Targets by Fission Fragments - I. A. Baranov and V. V. Obnorski . . . . .	192	184
Radiation Testing and Thermal Testing of Compton-Emission Neutron Detectors Having a Hafnium-Containing Emitter - I. Ya. Emel'yanov, Yu. I. Volod'ko, O. K. Egorov, S. B. Zlokazov, V. V. Postnikov, Yu. A. Safin, and V. I. Uvarov . . . . .	198	189
Local Radiation Action of Atmospheric Emissions Associated with the Operation of a Radiochemical Plant - I. N. Ruzhentsova and E. N. Teverovskii . . . . .	203	192
Allowance for Economic Discounting in Estimation of the Harm Done by Radioactive Contamination of the Biosphere by Nuclear Energy Facilities - V. F. Demin, E. I. Ermakova, and Ya. V. Shevelev . . . . .	207	195
<b>LETTERS TO THE EDITOR</b>		
Experimental Data on the Neutron Fields of the VVÉR-440 - S. S. Lomakin, A. G. Morozov, G. G. Panfilov, Kh. Ya. Bondars, and A. A. Lapenas . . . . .	213	200
Effects of Preliminary Few-Cycle Loading on the Radiation Embrittlement of 15Kh2MFA Steel - L. A. Vainer and B. T. Timofeev . . . . .	215	201
Generating Pure Beams of Nuclei in the Synchrophasotron of the Joint Institute of Nuclear Research - Yu. D. Beznogikh, V. P. Vadeev, M. A. Voevodin, V. I. Volkov, E. D. Donets, V. G. Dudnikov, L. P. Zinov'ev, V. A. Monchinskii, A. I. Pikin, I. N. Semenyushkin, V. M. Slepnev, S. A. Khorozov, and A. P. Tsarenkov . . . . .	217	202
Local Analysis of $^3\text{He}$ by Track Autoradiography of the $^3\text{He}(n, p)^3\text{H}$ Reaction - E. E. Goncharov, G. G. Ryabova, and D. A. Sorochan . . . . .	220	204
Approximate Solution of the $\gamma$ -Quanta Transfer Equation in Straight-Ahead Scattering - V. P. Zhemchugov . . . . .	222	205

**CONTENTS**

(continued)

Engl./Russ.

Temperature Dependence of the Scattering Cross Section of Cold Neutrons in Ditolylmethane - Yu. M. Berzilov, V. E. Zhitarev, A. M. Motorin, S. B. Stepanov, and Yu. V. Sharanin.....	224	206
Discrepancy of the Results of $\bar{\nu}_p$ Measurements in the Fission of $^{237}\text{Np}$ Nuclei by Neutrons - V. V. Malinovskii, V. G. Vorob'eva, B. D. Kuz'minov, V. M. Piksaikin, N. N. Semenova, S. M. Solov'ev, and P. S. Soloshenkov.....	226	208
Average Number of Prompt Neutrons in the Fission of $^{232}\text{Th}$ Nuclei by Neutrons - V. V. Malinovskii, V. G. Vorob'eva, B. D. Kuz'minov, V. M. Piksaikin, N. N. Semenova, V. S. Valyavkin, and S. M. Solov'ev.....	229	209
Adjustment of the Neutron Flux with the Aid of Adsorption Systems - I. G. Gverdtsiteli, A. G. Kalandarishvili, M. N. Korotenko, S. D. Krivonosov, A. V. Nikonov, and N. N. Parkhomenko.....	231	211
$^{169}\text{Yb}$ Gamma Sources - A. V. Klinov, A. V. Mamelin, and Yu. G. Toporov.....	233	212
Comparison of the One-Group Constants of the Actinides in a Test Model of a Fast Reactor - A. I. Voropaev, V. V. Vozyakov, A. I. Zinin, and A. G. Tsikunov.....	236	214
Purification of the BR-10 Sodium Coolant from Cesium Radionuclides - V. P. Vaizer, I. A. Efimov, É. E. Konovalov, A. I. Lastov, and V. S. Shereshkov.....	238	215

The Russian press date (podpisano k pechati) of this issue was 2/25/1983.  
Publication therefore did not occur prior to this date, but must be assumed  
to have taken place reasonably soon thereafter.

## ARTICLES

OPERATING EXPERIENCE WITH THE VVÉR-1000 REACTOR  
FUEL-ELEMENT ASSEMBLIES OF THE FIFTH UNIT  
OF THE NOVOVORONEZH NUCLEAR POWER STATION

Yu. V. Vikhorev, V. A. Voznesenskii,  
V. V. Goncharov, K. P. Dubrovin,  
V. N. Proselkov, V. A. Sidorenko,  
V. N. Siryapin, N. L. Fatieva, and N. S. Fil'

UDC 621.039.566

The fifth unit of the Novovoronezh nuclear power station, with a VVÉR-1000 reactor, was switched into the grid system on May 30, 1980 and it was brought to nominal power on February 20, 1981. It was a pilot unit for the third generation of pressure-vessel water-cooled/water-moderated reactors with an electrical capacity of 1000 MW. The development of the VVÉR from the first unit of the Novovoronezh nuclear power station took place via the path of optimization of the fuel and thermal power cycles, with improvement of the specific technicoeconomic indices. The demands for safety of nuclear power stations have been increased constantly. Subsequent development of the VVÉR-1000 provides for transition from the base to the adjustable operating cycle. The requirements for adjustable characteristics of nuclear power station plants are formulated mainly by the requirements of the consumer. The nuclear power station must ensure a drop and rise of power at the rate of 1 to 4% of the running value per minute, depending on the lower level.

The results of the startup operations and the bringing to power of the fifth unit are discussed in [1]. The present paper contains an analysis of the results of the operation of the fuel element assemblies (FEA) of the fifth unit according to the situation in April, 1982.

Principal Characteristics of the Reactor Facility, Core, Fuel Element Assemblies, and Fuel Elements.

The principal characteristics of the fuel were determined with optimization of the fuel cycle, taking account of the limitations imposed by the conditions of transportability of the reactor vessel, the limiting working temperature of the zirconium alloy of the fuel element cans, the coolant flow rate, etc.

Optimization of the coolant cycle parameters and the fuel characteristics related with them by comparison with the VVÉR-440 was conducted on the basis of more-profound concepts about the thermal and physical processes in the reactor core, the subsequent development of intrareactor measurements, and the increase of reliability of heat removal [2]. Increase of the thermal capacity of the VVÉR-1000 has been achieved because of the reduction of the nonuniformity of the heat release in the core. The cartograms of the first and second fuel changes of the core are shown in Fig. 1.

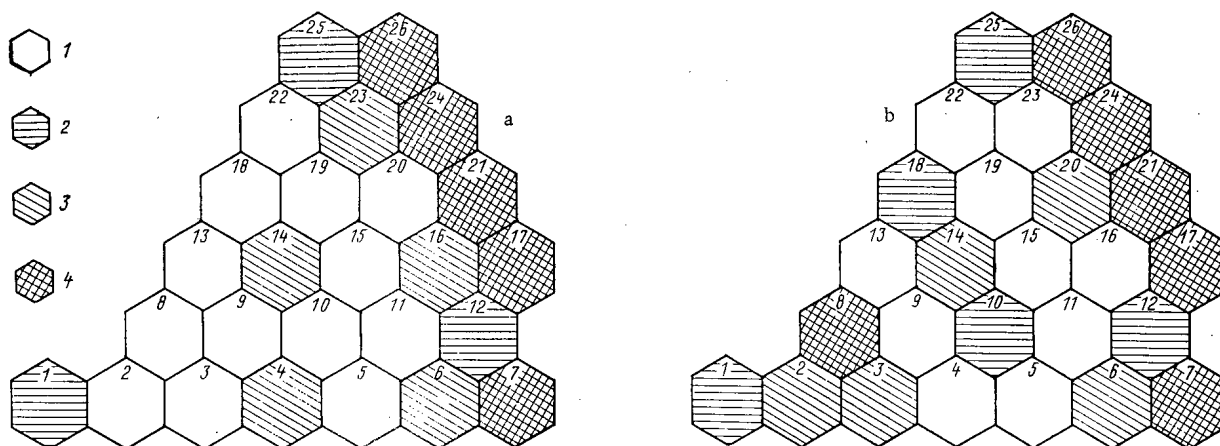


Fig. 1. Cartograms of the first (a) and second (b) fuel charges (1/6 of the core): 1, 4) enrichment of the FEA, 2.0 and 3.3%, respectively (317 fuel elements); 2) FEA with profiling conforming to enrichment 3.3, 3.0, and 2.4% (251, 48, and 18 fuel elements, respectively); 3) FEA with profiling conforming to enrichment 3.0 and 2.4% (251 and 66 fuel elements, respectively).

Translated from *Atomnaya Énergiya*, Vol. 54, No. 3, pp. 163-166, March, 1983. Original article submitted September 16, 1982.

The principal design characteristics of the reactor core of the fifth unit for a two-yr run are given below:

Nominal thermal capacity, MW	3000
Nominal coolant pressure at the reactor outlet, MPa	15.7
Average coolant temperature, deg C:	
at reactor inlet:	
design	290
actual	
at reactor outlet:	
design	322
actual	317
Coolant flow through reactor, m <sup>3</sup> /h:	
design	80,000
actual	88,000
Calculated average fuel burnup, MW · days/kg U:	
for fuel element assemblies of first charge	12
for fuel element assemblies of second charge	23.3
for steady-state recharging conditions	30
Average power intensity of the core, kW/liter	111
UO <sub>2</sub> charge in core, tons	75.5
Running time, yr	2
No. of rechargings during run	2
Fuel enrichment (first fuel charge), %	2, 3, and 3.3 (78, 18, and 55 FEA)
Fresh fuel enrichment in steady-state recharging conditions, %	3.3
No. of fuel element assemblies	151
No. of fuel element assemblies with bundles of absorbing elements	109
No. of absorbing elements per bundle	12
Coefficient of nonuniformity of energy release over the core volume, Ky	2.79
Coefficient of nonuniformity of energy distribution over all fuel elements of the core, K <sub>FE</sub>	1.48
Average coolant flow rate, m/sec:	
at inlet to bundles:	
design	5.1
actual	5.4
at outlet from bundles:	
design	5.8
actual	6.1

The first period of operation provides for an annual recharging of one half of the fuel during a two-yr run of the fuel with an average burnup of 30 MW · days/kg U and a 3.3% enrichment of the makeup fuel. Subsequently, transition to a four-yr run with a 4.4% makeup fuel enrichment and an average burnup of MW · days/kg U is foreseen.

The characteristics of the FEA and fuel elements of the fifth unit are given below (fuel element cladding material - Zr + 1% Nb alloy; fuel - pellets of sintered uranium dioxide with a central hole; pressurization of the fuel elements is effected by electron-beam welding; gas below fuel element cladding - helium, pressure 1.96-2.45 MPa at room temperature):

Maximum temperature of fuel element cladding from the coolant side, deg C	350
Linear power of fuel element, W/cm:	
average	176
maximum design	525
maximum actual	465
Gauge of FEA below key, mm	238
No. of fuel elements in each FEA	317
Height of fuel column in operating state, mm	3560
Minimum fuel density, g/cm <sup>3</sup>	10.4
External diameter of fuel element, mm	9.1

Thickness of fuel element cladding, mm	0.63-0.68
Size of fuel-element-cladding diametral gap, mm	0.19-0.32
Diameter of central hole, mm	1.4-1.6
Volume of fuel element gas collector, cm <sup>3</sup>	11

During bringing to power and subsequent operation, conformity between the thermal loading distribution in the core and the design values was established. The maximum coefficients of nonuniformity of energy release in the FEA ( $K_Q$ ) and the core volume ( $K_V^{phys} = K_Q K_Z$ ) achieved during operation, taking account of the effect of the control elements, did not exceed 1.35 and 2.0, respectively. The experimentally determined coefficient of nonuniformity over the core volume ( $K_V^{phys}$ ) is a part of the total volume nonuniformity, calculated as

$$K_V = K_{FE} K_Z K_{eng},$$

where  $K_{FE} = 1.48$  is determined from physics calculations;  $K_{FE} = K_Q K_k$  ( $K_k$  is the nonuniformity of energy release with respect to the fuel elements of a single FEA);  $K_Z$  is the nonuniformity of energy release with respect to height ( $K_Z = K'_Z K_{Xe} = 1.48 \cdot 1.1 = 1.63$ );  $K_{eng} = 1.16$ , engineering safety factor, taking account of tolerances in manufacture and calculation errors; and  $K_{Xe} = 1.1$ , margin on the onset of xenon fluctuations.

By calculation,  $K_V = 2.79$ . The maximum calculated (design) linear power of a fuel element  $q_{fd}^{max} = q_l K_V K_N = 176 \cdot 2.79 \cdot 1.07 = 525$  W/cm, where  $K_N = 1.07$  is a coefficient, taking account of the error of determining (4%) and maintaining (3%) the reactor power.

Since the actual error in determining and maintaining the reactor power does not exceed 4%, and  $K_{Xe}$ , in view of the measures to suppress xenon fluctuations, reduces to 1.0, the actual maximum linear power of a fuel element does not exceed  $q_{fd}^{max} = 465$  W/cm.

Operating Conditions of the Fuel Element Assemblies. During the operation of the FEA of the fifth unit, the number of regions of reactor power change was increased. This was related with both the conditions of operation of the grid system and with breakdowns of the nuclear power station plant in the initial period of operation.

The systematic heating up of the facility from the cold state to the hot state was effected with a rate not exceeding 20°C/h. Up to the level of 40-45% of the nominal power value, the rate of increase amounted to not more than 6% per min; further increase was conducted with a rate of 1% per min, and with obligatory holding at the 75-85% level during 3 h. In the case of systematic cooling down, the rate of reduction of the coolant temperature did not exceed 30°C/h.

Before the first recharging the reactor operated for 258 effective days. The average and maximum burnup by the FEA in the core achieved amounted to 11.9 and 14.8 MW·days/kg U, respectively. These values are somewhat lower than the design values for the first reactor charge. The incomplete fuel burnup is due to the necessity for the premature recharging of the reactor before the onset of the fall-winter maximum demand for electric power. Operation of the reactor with the second fuel charge started on November 23, 1981. After operation of the reactor over 120 effective days from the time of recharging, the fuel burnup throughout the core on the average, was 13.3 MW·days/kg U, for a maximum burnup in the FEA of 21.4 MW·days/kg U.

The total number of different reactor operating cycles during the time of operation from May 30, 1980 to May 1, 1982 is given below:

Startup from cold state	9
Power reduction from nominal to minimum, corresponding to the hot state of the reactor	12
Power increase from minimum, corresponding to the hot state of the reactor, to nominal	15
Systematic power reduction with subsequent cooling of the reactor	8
Load dumping by 20-50% of the actual reactor power	90
Stepwise load increases: at intervals up to 50% by 20%, and from 50 to 100% by 10% of the actual reactor power	117
Disconnection of one loop of the four operating, and connection of one loop to three operating loops	44
Disconnection and connection of two loops	9

Actuation of the scram system of the first species with emergence of the reactor into the hot state	28
Actuation of the scram system of the second species (switching-off one turbogenerator)	3

During the first operating cycle of the reactor, i.e., up to the first fuel recharging, 64 power reductions to zero were carried out, of which 27 were the actuation of the scram system of the first and second species. A large part of the scram system actuations was effected in the course of carrying out the development of a program of regimes with actuation of the scram system. During the second operating cycle (after the first fuel recharging), 4 scram system actuations and 12 power reductions by 50% occurred, according to the situation at April 1, 1982.

It can be seen from Table 1 that during the time of operation, of the 398 transitional regimes (power shedding and drawing), the major part fell within the first cycle and the first fuel charge. An analysis of the coolant activity of the primary circuit and the results of monitoring the hermeticity of the fuel element cans of the first fuel charge show that the considerable number of power variations did not affect the working efficiency of the fuel elements.

The investigation of the fuel operating regimes and the activity of the coolant of the primary circuit has great importance from the point of view of studying the fuel reliability, since one of the problems arising during the solution of the question of increasing the adjustability of nuclear power stations is the stability of the fuel elements in variable power conditions [3-5]. The main cause of rupture of the fuel elements in this case is the mechanical action on the fuel cladding as the result of thermal expansion. The state of pressurization of the fuel element cans for the period of debugging of the plant, which can be characterized by the increased number of failures, it is important information for studying the reliability of the fuel elements.

Analysis of the Condition of the Fuel Element Cans from the Activity of the Water of the Primary Circuit and during Recharging. During the first cycle of operation, a radiochemical analysis of the coolant in the operating reactor (relative to the activity of the fission products) and monitoring of the pressurization of the fuel element cans in the shut-down reactor (by the method of digestion in a hermetically sealed box) were carried out.

The activity of the primary circuit coolant from the dry residue and the sum of the iodine isotopes did not exceed  $2.7 \cdot 10^7$  and  $9.6 \cdot 10^6$  Bq/kg, respectively, at nominal power ( $1 \text{ Ci} = 3.7 \cdot 10^{10}$  Bq), which is significantly below the maximum permissible values. In the analysis of the composition of the coolant activity, it was established that at the time of recharging there were no fuel elements in the core with large-scale defects, and that the number of depressurized fuel elements with gas leakage (microdefects) was significantly less than the design value. No grouping of depressurized fuel elements was noted in any part of the core, which indicated an identical level of activity in all loops.

When monitoring the pressurization of the fuel element cans in the shut-down reactor, 48 FEA were checked, of which one FEA (06-04), intended for routine removal from the reactor, was found to be depressurized. During the period of operation of the reactor, the mid-monthly discharge of radioactive noble gases into the atmosphere amounted to about  $6.3 \cdot 10^{12}$  Bq.

TABLE 1. Number of Power Variations (increase/decrease) during the Period of Operation of the Fifth Unit from June, 1980 to March, 1982

Range of reactor thermal power, in which its variation was effected, MW	Range of thermal power variation, MW											Total
	up to 150	150-300	300-600	600-900	900-1200	1200-1500	1500-1800	1800-2100	2100-2400	2400-2700	2700-3000	
0-1000	7/6	12/11	12/7	15/10	—	—	—	—	—	—	—	46/34
1000-2000	12/13	17/12	10/5	8/11	9/9	12/15	7/6	3/2	—	—	—	78/73
2000-3000	21/18	7/7	9/8	7/9	9/10	12/7	4/0	5/2	3/7	2/1	9/10	88/79
Overall total	40/37	36/30	31/20	30/30	18/19	24/22	11/6	8/4	3/7	2/1	9/10	212/188

## CONCLUSIONS

The initial operation of the fifth unit was characterized by an increased number of transitional regimes, the number of which did not exceed the design values. No effect of the considerable number of power variations on the working efficiency of the fuel elements was observed. An analysis of the primary circuit coolant activity with respect to fission products shows that operation of the fifth unit is characterized by a low degree of depressurization of the fuel element cans. The number of fuel elements with microdefects is significantly lower than the limiting value, which confirms the high reliability of the fuel elements. After attaining nominal power level, no marked depressurization of the fuel elements develops.

## LITERATURE CITED

1. Yu. V. Vikhorev et al., *At. Energ.*, 50, No. 2, 87 (1981).
2. V. A. Sidorenko, *Problems of the Safe Operation of VVER Reactors* [in Russian], Atomizdat, Moscow (1977).
3. F. G. Reshetnikov, *At. Energ.*, 50, No. 2, 118 (1981).
4. V. V. Zverkov et al., in: *Nuclear Power Stations* [in Russian], 3rd ed., *Énergiya*, Moscow (1980), p. 66.
5. F. G. Reshetnikov et al., in: *Proceedings of an IAEA Symposium on the Fabrication of Water Reactor Fuel Elements*, Vienna (1979), p. 107.

USE OF THE THERMAL COOLANT NOISE IN FLOW RATE  
MEASUREMENT FOR RBMK CHANNELS

V. M. Selivanov, N. P. Karlov,  
A. D. Martynov, V. V. Prostyakov,  
B. V. Lysikov, B. A. Kuznetsov (USSR),  
D. Pallagy, S. Horany,  
T. Hargitai, and S. Toszer (Hungary)

UDC 621.039.564.2.5

The coolant flow rate in the core is one of the basic parameters of a reactor. The current level of electronic engineering makes it possible to measure the flow rate by statistical analysis of the coolant noise. The method is based on the correlation between the random signals propagating in the moving medium and the time characteristics of the flow [1]. The random signals, in particular, may be coolant temperature fluctuations. The coolant speed is then calculated as the ratio of the distance between two thermoelectric transducers TET in the flow to the transport time for fluctuations to travel this distance [2]. The advantages of the correlation (thermometric) method of determining speed (flow rate) are that the result is independent of the coolant temperature, there is minimal pressure difference, and there are no moving parts in the primary transducer (correlation flowmeter).

Here we consider the use of the thermometric correlation method to measure coolant flow rates in RBMK channels. Particular attention is given to the physical nature of the temperature fluctuations and to estimating the effects of the primary-transducer parameters on the results.

Experimental studies [3] indicate that the structure of a turbulent flow can be represented as the combined motion of interacting turbulent eddies differing in speed. These eddies differ also in temperature if there are temperature gradients in the flow.

The speed and temperature fluctuations have a wide spectrum in a turbulent flow, which indicates that perturbations differing in scale and energy are present. The correlations for the temperature fluctuations in developed turbulent flow are determined mainly by the scales of the perturbations [4].

When the flow rate is measured by a correlation method, it is undesirable to use the entire spectrum of the thermal noise. Natural convection may influence the measured speed in the infralow frequency range. Also,

---

Translated from *Atomnaya Énergiya*, Vol. 54, No. 3, pp. 166-169, March, 1983. Original article submitted September 3, 1982.

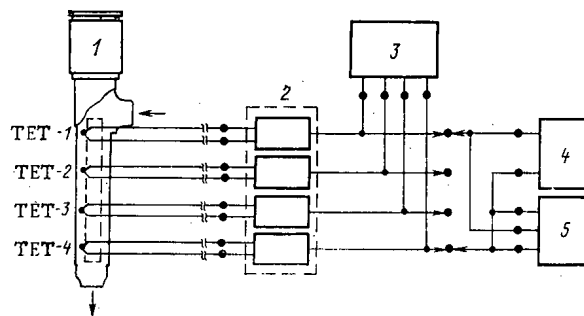


Fig. 1. Structural diagram of the equipment: 1) TCF; 2) four-channel amplifier; 3) tape recorder; 4) double-beam oscilloscope; 5) correlator.

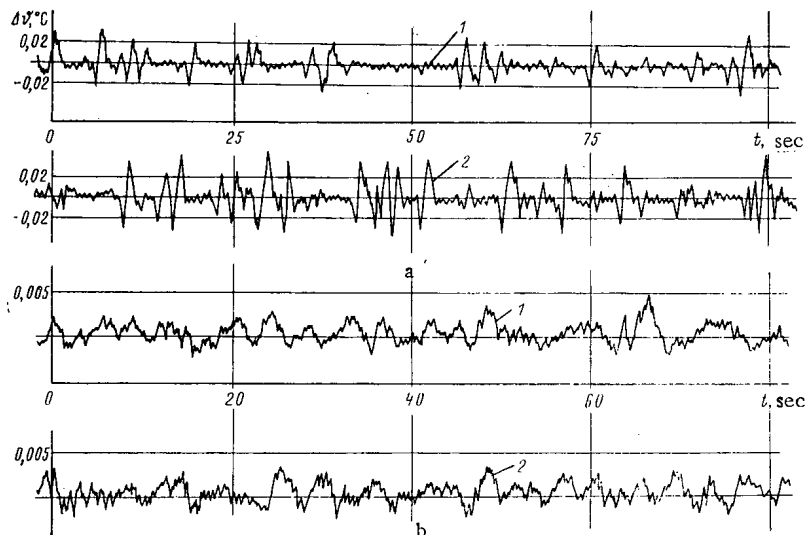


Fig. 2. TEP-1 signals from TCF in cells 25-64 (a) and 11-40 (b) for flow rates of 10 (1) and 30 m<sup>3</sup>/h (2).

the dispersal in the probability characteristics increases [5] as the frequency of a stochastic process is reduced. Therefore, the low-frequency part of the spectrum must be cut off. The upper boundary to the spectrum is set by the natural fall in the temperature fluctuations and also by the frequency response of the TET.

The temperature fluctuations at the points of flow rate measurement arise in the multichannel RBMK on account of the temperature gradient between the coolant and the surrounding medium and also because the thermally inhomogeneous mixture is transported along the system, this being formed by mass transfer between flows differing in temperature within the large volumes of the branched circulation loop (in the collectors). The intensity of the temperature fluctuations is dependent on the position of the flowmeters in the group collectors [6] and is determined by the superposition of turbulent and mixing fluctuations.

During reactor research, studies have been made on the distribution of the thermal noise at the flow-rate measurement points, and the intensity and physical nature have been determined, along with the effects of various parameters in the primary transducer (lag in the TET and baseline distance between them) as regards the accuracy of measurement.

A thermometric correlation flowmeter TCF was devised for the purpose, which consisted of four TET placed in the body of a tachometric spherical flowmeter of Storm type. The TET assembly was made as a hollow plate welded to the body. The TET were placed within the plate, and the leads were brought out through the flowmeter plug. The shell diameter of a TET was 3 mm, while the diameter of the working junctions was 1.5 mm. The TET junctions projected from the plate on the side opposite to the inlet tube. This disposition was used for the TET working junctions because of the more-stable coolant flow in this part of the flowmeter. The distance between the TET-1 and TET-2 junctions was 40 mm, that between TET-2 and TET-3 80 mm, and between TET-3 and TET-4 80 mm, which when used in various combinations enabled one to measure flow rates with baseline distances of 40, 80, 120, 160, and 200 mm.

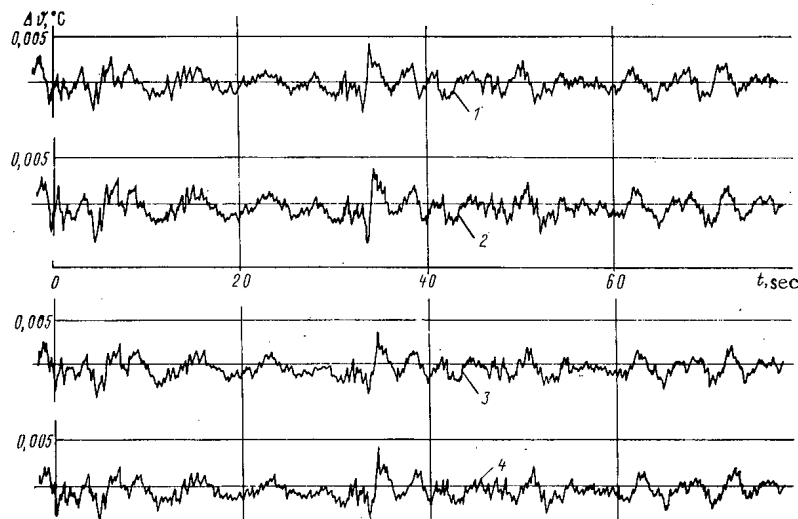


Fig. 3. Change in the signals from TET-1 (1), TET-2 (2), TET-3 (3), and TET-4 (4) over the height of the TCF in cell 11-40 for  $Q = 50 \text{ m}^3/\text{h}$ .

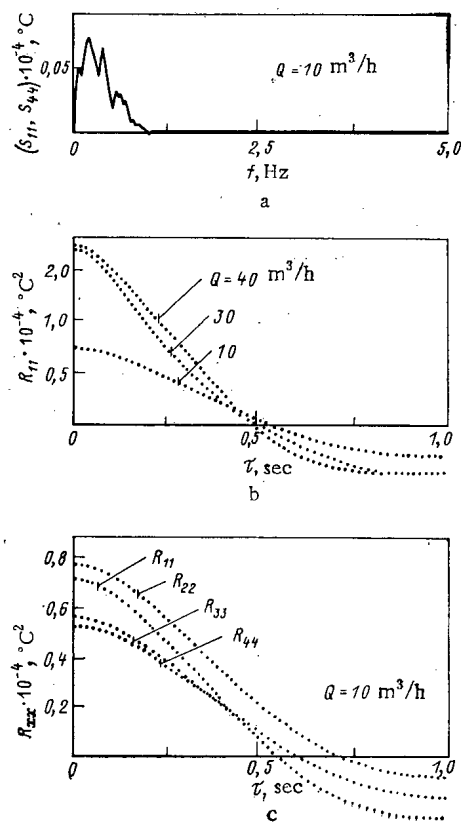


Fig. 4. Spectral density (a) and autocorrelation functions (b, c) for TET signals from the TCF in cell 25-64.

Experimental specimens of the correlation assemblies were placed in the bodies of standard installed flowmeters in the channels of cells 25-64 and 11-40 (Fig. 1). The measurements were made in the frequency band 0.5-5.0 Hz with amplifiers whose inherent noise level was not more than  $0.05 \mu\text{V}$  at a coolant temperature of about  $270^\circ\text{C}$  and a pressure in the pressurized collector of about 8.0 MPa. The coolant flow rates in these channels were controlled in the range 10-50  $\text{m}^3/\text{h}$  and were monitored by duplicating flowmeters of differential-manometer type.

The TET signals from two correlation flowmeters (Fig. 2) showed that throughout the flow-rate range there were differences in the character of the temperature fluctuations. The temperature fluctuations for TCF

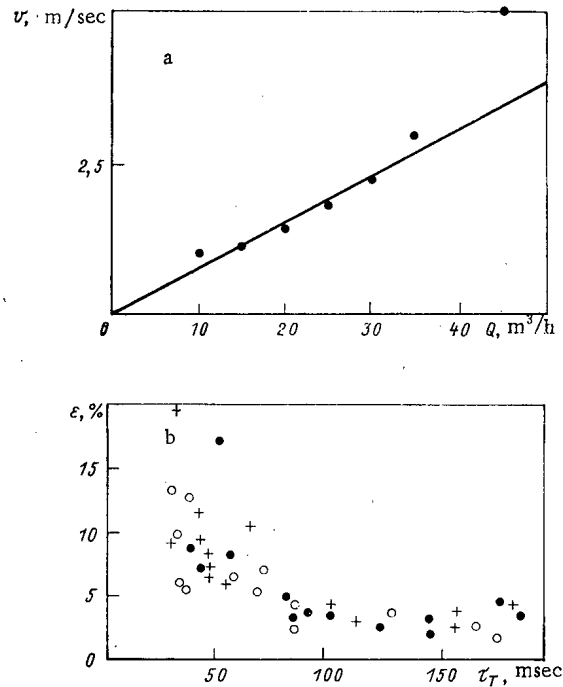


Fig. 5. Comparison of the correlation speed measurements on a baseline  $S = 200$  mm with data from the differential-manometer flowmeter (a) and dependence of the relative error in measuring water speed (on a test bed) in relation to transport time (b) for  $S = 200$  (●),  $120$  (+), and  $80$  (○) mm.

in cell 25-64 tended to come in bunches, i.e., alternation of time intervals with large and small amplitudes. The character of the signal persisted on the flow rate increased, while the frequency rose somewhat. The intensity of the temperature fluctuations varied from about  $0.01^\circ\text{C}$  with a flow rate of  $10\text{ m}^3/\text{h}$  to about  $0.025^\circ\text{C}$  at  $40\text{ m}^3/\text{h}$ . These values exceed by an order of magnitude the level of the turbulent-fluctuation intensity as defined from [3]:

$$\sigma_t^{\max} = C\Delta t_\alpha,$$

where  $\Delta t_\alpha$  is the temperature difference between the wall and the coolant flow, and  $C$  is a constant dependent in general on the flow conditions and coolant properties (on the  $Pe$  number).

The TET signals from the flowmeter in cell 11-40 were of the stationary type at all flow rates. The signal intensity was almost independent of the flow rate and was about  $0.001^\circ\text{C}$ . The results indicate that in the TCF in cell 11-40 there are turbulent pulsations, while in the flowmeter in cell 25-64 there is a superposition of the turbulent pulsations and the mixing ones brought in by the flow from external temperature-noise sources. The correlation coefficients in both cases were high (about 0.8-0.9).

Figure 3 shows the variation in the TET signals over the height of the TCF in cell 11-40; the signals for all four thermocouples are virtually the same, which indicates that there is only slight change in the temperature fluctuations and that the flow in the measurement zone has adequate hydrodynamic stability. The signal frequency range can be judged from the spectral density (Fig. 4a), while the increase in frequency with flow rate can be judged from the change in the autocorrelation functions (Fig. 4b). The differences between the autocorrelation functions in Fig. 4c confirms that there is a spread in the time-constants of the TET.

The speeds calculated from the correlation and differential-manometer flowmeters were in satisfactory agreement for flow rates between  $10$  and  $30\text{ m}^3/\text{h}$ . There was a deviation from linearity at higher flow rates, and the correlation flowmeter data deviated upwards considerably (Fig. 5a).

The error in speed measurement by the correlation method increases [7] when the transport time  $\tau_t$  decreases to values equal to or less than  $\tau_\alpha$ , the lag in the TET (Fig. 5b), i.e., when  $\tau_t \leq \tau_\alpha$ ; with this relation between the parameters, the position of the peak in the cross-correlation function becomes closer to the ordinate, and then the possible spread in the TET time-constants (Fig. 4c) and in the passband of the measurement

systems (and sometimes in the presence of synphase noise at the amplifier output) may influence the position of the peak appreciably, and thus can lead to a substantial increase in the error in calculating the coolant speed.

Therefore, these studies show that there is a considerable nonuniformity in the temperature-noise distribution at the points of coolant flow-rate measurement in the RBMK channels, which is due to temperature fluctuations of various origins. The minimum value of the temperature-fluctuation intensity is about  $0.001^{\circ}\text{C}$ . Further improvement in the design of the thermometric correlation flowmeter should be made, firstly, by locating the working ends of the TET in a zone of stable hydrodynamics; secondly, it is desirable to choose the baseline distance between the TET on the basis of observing the inequality  $\tau_t > \tau_{\alpha}$  throughout the flow-rate range. That approach will minimize the systematic error arising from the spread in the TET lag and will reduce the severity of the specifications for the analog measuring instruments in the correlation systems.

#### LITERATURE CITED

1. J. Boland, Reactor-Monitoring Instruments [Russian translation], Atomizdat, Moscow (1973).
2. V. M. Selivanov et al., *At. Énerg.*, 42, No. 1, 49 (1977).
3. M. Kh. Ibragimov et al., Turbulent-Flow Structure and the Heat-Transfer Mechanism in Channels [in Russian], Atomizdat, Moscow (1978).
4. V. M. Selivanov et al., "Utilization of thermocouple random signal correlation method for coolant flow-rate measuring in nuclear power plants," Measurement for Progress in Science and Technology, IMEKO-VIII. Preprint Section IV, Moscow (1979), p. 5.
5. J. S. Bendat and A. G. Piersol, *Random Data: Analysis and Measurement Procedures*, Wiley (1971).
6. I. Ya. Emel'yanov et al., *At. Énerg.*, 51, No. 4, 215 (1981).
7. V. M. Selivanov et al., "Development and examination of a thermometric correlation system for measurement of coolant flow rate for the RBMK reactor," Preprint KFKI-1980-70, Budapest (1980).

#### ACOUSTIC EFFECTS FROM WATER LEAKING INTO SODIUM

V. S. Yugai, R. F. Masagutov,  
and F. A. Kozlov

UDC 621.039.534.8

Tight specifications are imposed on the reliability of fast-reactor nuclear power stations, in particular for the sodium-water steam generators. In this connection, considerable attention is being given to the acoustic method of observing leaks of water into the sodium in the generator. Various experimental studies [1-3] show that the method is promising.

On the other hand, the creation of an acoustic leak-detection system involves solving various complicated scientific and technical problems, of which primary importance attaches to high-temperature means of acoustic measurement and the leak-detection algorithm. The latter requires a study of the acoustic effects related to leaks.

Various processes can act as noise sources when water leaks into sodium in the steam generator; flow of the steam jet from the defect into the heat-transfer tube or into the unit where the tube is fitted into the tube support; oscillations of the hydrogen bubbles formed by reaction between the sodium and the water; boiling of the sodium in the leak zone on account of local reaction heat; and acoustic emission in the components as the leak develops.

It is complicated to observe a leak, because there is a considerable noise level arising from various sources even in the absence of a leak on account of the operation of the steam generator and the other power station equipment, which is acoustically coupled through the coolant and the pipelines to the steam generator. The steam generator is a cylindrical vessel, with a ratio of length to diameter of 5:25, and it may be considered as a narrow bounded tube as regards the propagation of low-frequency noise. For example, with a diameter of 0.6 m the steam-generator module may be considered as a narrow tube for oscillations in the sodium of frequency less than 5 kHz.

Translated from *Atomnaya Énergiya*, Vol. 54, No. 3, pp. 170-173, March, 1983. Original article submitted May 10, 1982.

The body of the module has a certain elasticity, and therefore the speed of acoustic waves of any given wavelength is less than the speed in an unbounded medium. The reaction of the wall is elastic if the circumference of the body is less than the wavelength of the sound in the material. The wave speed in the generator module varies at frequencies less than 1 kHz. The relative reduction in the wave speed at frequencies less than 1 kHz is about 0.3 for the generator module, on the basis of the wall elasticity and the sodium compressibility.

The steam generator module is filled with a tube bundle (there is steam in the tubes) and with sodium around the tubes. If the diameter of a tube is 16 mm and the pitch of the tube in the bundle in a triangular array is 28 mm, then diffraction will occur at a tube for wavelengths much less than the tube diameter, i.e., for oscillations with frequency over 15 kHz.

The noise due to the water boiling in the heat-transfer tubes is the main source of interference in the detection of noise arising from the leakage of water into sodium in the generator module. Calculations have been performed on the transfer coefficients for the passage of boiling-water noise through the tube wall into the sodium, which show that this noise has a substantial effect in the range 1-30 kHz. There is a tendency for the boiling noise intensity to decrease as the frequency rises, so the effects of noise in the ultrasonic range will be considerably less.

The speed of sound in sodium is dependent on the state parameters:  $C = C(T, P)$ , or for small increments

$$\Delta C = \left( \frac{\partial C}{\partial T} \right)_P \Delta T + \left( \frac{\partial C}{\partial P} \right)_T \Delta P.$$

Experimental and theoretical values are available for the speed of sound at the melting point of sodium [4]:  $C = 2653$  m/sec;  $(\partial C/\partial T)_P = 0.58$  m/(sec · deg) at 371 °K, and  $(\partial C/\partial P)_T = 0.62 \cdot 10^{-6}$  m/(sec · Pa) at 383 °K.

If we assume that the speed of sound varies linearly with temperature, then we have that a change in sodium temperature of 200 deg alters the speed of sound by about 5%. A change in pressure in the module under isothermal conditions by  $3.03 \cdot 10^5$  Pa alters the speed of sound in the sodium by a value comparable with the error of measurement.

Solid and gaseous impurities in the sodium can be considered as microscopic inhomogeneities in acoustic measurements at 0.200-200 kHz. The density is important for a solid impurity, while the compressibility is important for a gaseous one. The effects of these impurities on the speed of sound in sodium  $C = \sqrt{1/\rho\beta}$  can be expressed as

$$\frac{\Delta C_\beta}{\Delta C_\rho} = \frac{\Delta\beta/\beta}{\Delta\rho/\rho} \cong \rho C_0^2 g,$$

where  $\beta$  is compressibility;  $\rho$ , density; and  $g$ , coefficient equal to  $3/[4\pi^2\rho(R_0f_0)^2]$  (here  $f_0$  and  $R_0$  are the resonant frequency and radius of a hydrogen bubble).

Clearly, the compressibility change has a decisive effect on the speed of sound.

Therefore, consideration of the module design enables one to choose the working frequency range for detecting leaks. On the other hand, it is also necessary to determine the most likely frequency range for leak acoustic effects in making this choice. The effects associated with gaseous hydrogen are most relevant for the observation of small leaks of water into the sodium. The hydrogen bubbles oscillating in the sodium at the natural resonant frequencies provide a noise source when there is a leak. In order to define the measurement frequency range, it is necessary to know the size distribution of the hydrogen bubbles. According to [5], for the bubble mode of flow for a leak of  $< 10$  g/h the initial (detachment) hydrogen bubble diameter can be taken as 2 mm. As the bubble moves, the diameter falls because the hydrogen dissolves in the sodium. When bubbles fuse, it is possible for a bubble of larger size to arise. As the leak grows, the size of the defect increases, and therefore the hydrogen bubble detachment diameter rises. When the leak goes from bubble type to jet type, there are changes in the contributions from the various noise sources, namely there is an increase in the contribution from the noise generated by the escaping steam jet. It is therefore clear that in this complicated and self-accelerating process there is no predominant frequency or frequency range. Leak-detection algorithms should be based on a set of acoustic features characteristic of the various stages. Here it is desirable to examine the effects of sound absorption in the hydrogen bubbles. One can calculate the effective absorption cross section in order to determine the analyzer band width required to observe the absorption effect at various resonant frequencies.

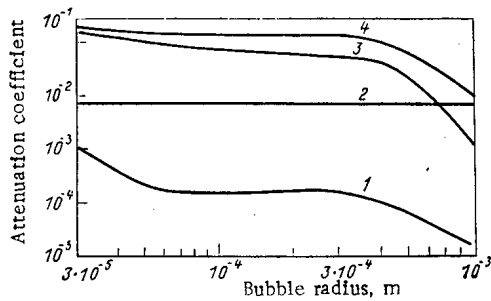


Fig. 1

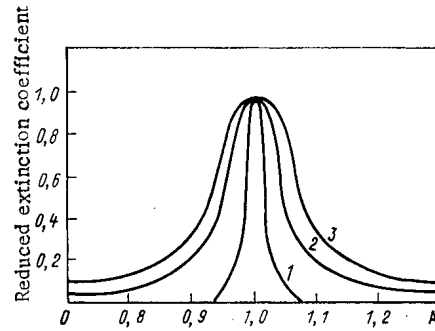


Fig. 2

Fig. 1. Attenuation coefficient for oscillations of a hydrogen bubble in sodium: 1) viscous-loss component; 2) loss component due to sound radiation; 3) thermal-loss component; 4) overall attenuation coefficient.

Fig. 2. Reduced extinction cross section for a hydrogen bubble in sodium (A is the ratio of the frequency of the incident wave to the natural frequency of the bubble): 1)  $R_0 = 10^{-3}$  m,  $\delta = 0.617$ ,  $f_0 = 6$  kHz,  $\sigma_0 = 5.03 \cdot 10^{-2}$  m<sup>2</sup>; 2)  $R_0 = 3 \cdot 10^{-4}$  m,  $\delta = 0.092$ ,  $f_0 = 20$  kHz,  $\sigma_0 = 8.21 \cdot 10^{-4}$  m<sup>2</sup>; 3)  $R_0 = 3 \cdot 10^{-5}$  m,  $\delta = 1.145$ ,  $f_0 = 200$  kHz,  $\sigma_0 = 5.22 \cdot 10^{-6}$  m<sup>2</sup>.

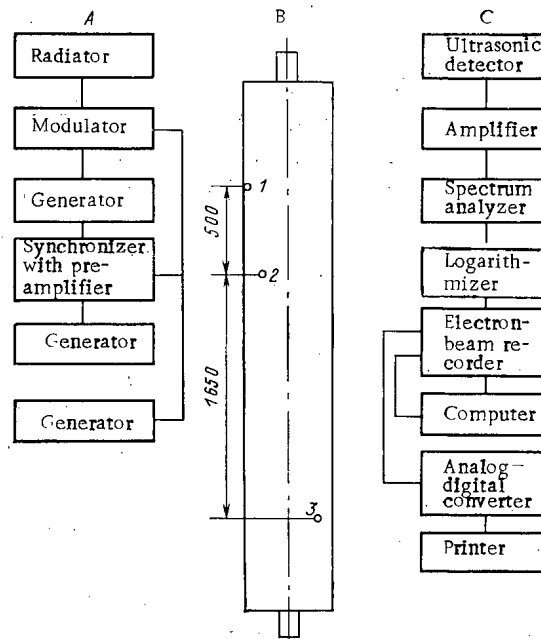


Fig. 3. Acoustic-measurement scheme: A) emission of oscillations in the experimental part; B) experimental part (1-3; positions of radiator, ultrasonic detector, and device for feeding water into sodium); C) system for receiving and processing acoustic noise.

There are three types of energy dissipation when an acoustic wave interacts with a hydrogen bubble in sodium:

- 1) thermal losses due to bubble heating and the loss of heat to the sodium in response to the volume changes produced by the second wave  $\delta_T$ ;
- 2) radiation losses due to scattering of the acoustic energy by the vibrating bubble as a spherical radiator  $\delta_R$ ; and
- 3) viscous losses due to the formation of sodium flows around the hydrogen bubble  $\delta_V$ .

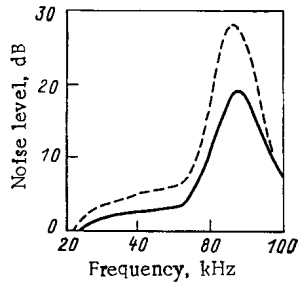


Fig. 4

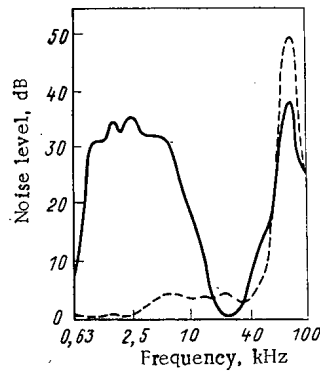


Fig. 5

Fig. 4. Absorption of ultrasound by hydrogen bubbles ( $T_{Na} = 500^\circ\text{C}$ ,  $f_{rad} = 100$  kHz); ----) noise level before feeding water into sodium; —) noise level 5 sec after stopping supply.

Fig. 5. Ultrasound absorption in feeding water into sodium ( $T_{Na} = 350^\circ\text{C}$ ,  $f_{rad} = 100$  kHz): ----) noise level before feeding water into sodium; —) noise upon feeding water with a flow rate of 0.2 g/sec.

Therefore, the overall damping coefficient will be the sum of the three terms,  $\delta = \delta_T + \delta_r + \delta_v$ .

Damping coefficients have been calculated for hydrogen bubbles of size  $10^{-6}$ – $10^{-3}$  m; the dependence of the coefficient on the radius is shown in Fig. 1. To characterize the absorption and scattering at vibrating bubbles it is necessary to determine the effective extinction cross section  $\sigma_e$ , which is equal to the sum of the absorption cross section  $\sigma_a$  and the scattering cross section  $\sigma_s$ . The extinction cross section is given by [6]

$$\sigma_e = \frac{4\pi R_0^2 (\delta/\eta)}{(f_0^2/f^2 - 1)^2 + \delta^2},$$

where  $\eta = 2\pi R_0/\lambda$  is the ratio of the circumference of the bubble to the wavelength. The variation in  $\sigma_e$  was considered for bubbles whose resonant frequencies were 6–200 kHz. Figure 2 shows calculations on the extinction cross sections for hydrogen bubbles in sodium at frequencies close to resonance. The absorption and scattering cross sections are given by [6]

$$\sigma_a = \frac{4\pi R_0^2 (\delta/\eta - 1)}{(f_0^2/f^2 - 1)^2 + \delta^2}, \quad \sigma_s = \frac{4\pi R_0^2}{(f_0^2/f^2 - 1)^2 + \delta^2}.$$

Clearly,  $\sigma_e/\sigma_s = \delta/\eta$ , i.e., hydrogen bubbles in sodium absorb sound much more strongly than they scatter it. On reducing the bubble radius from  $10^{-3}$  to  $3 \cdot 10^{-5}$  m, the ratio increases by a factor of 8.5. If the number of hydrogen bubbles in a unit volume is small, the overall attenuation is equal to the sum of the attenuations at all the bubbles:  $K_e = A n \sigma_e$ . The minimum distance  $l_{min}$  between hydrogen bubbles such that their extinction cross sections do not overlap can be derived from the resonance condition

$$\sigma_{l_0} = \frac{4\pi R_0^2}{\delta_0 \eta_0}.$$

The condition  $\frac{l_{min}}{R_0} = \frac{4}{\sqrt{\delta_0 \eta_0}}$  corresponds to the following volume concentration of hydrogen in the sodium:

$$\alpha = \delta \left( \frac{R_0}{l_{min}} \right)^3.$$

These arguments show that the dependence of  $K_e$  on  $\alpha$  is of saturation type, i.e., the attenuation coefficient is proportional to  $\alpha$  only for  $\alpha \leq \alpha_0$  and attains its maximum value for  $\alpha = \alpha_0$ .

Experimental studies have been made on the attenuation at hydrogen bubbles in a working section represented by a tube of diameter 312 mm and length 3000 mm; wall thickness 6 mm. Within the tube there was a bundle of 61 tubes of diameter  $16 \times 2$  mm. The sealed tubes were mounted with a pitch of 28 mm in a

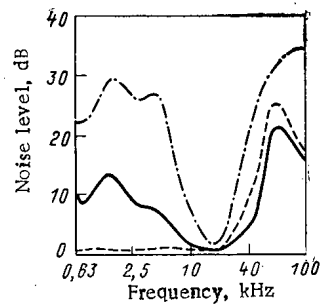


Fig. 6. Absorption and rise in ultrasound upon feeding water into sodium ( $T_{\text{Na}} = 500^{\circ}\text{C}$ ,  $f_{\text{rad}} = 80 \text{ kHz}$ ): - - -) noise level before feeding water into sodium; —) noise level upon feed-water with a flow rate of 0.05 g/sec; - · -) noise level upon feeding water with a flow rate of 0.8 g/sec.

triangular lattice in tube mounts separated by distances of 2500 mm. The sodium rose into the space between the tubes with a speed of 0.02 m/sec. Figure 3 shows the disposition of the device for feeding water into the sodium, of the acoustic detectors, and of the radiator. It also shows schemes for the emission of sinusoidal oscillations at various frequencies and the reception of acoustic noise. The measurements were performed in the following sequence. Initially we measured the noise spectrum at acoustic detectors for emission of a sine wave at a definite frequency in the working part. Then the water was injected into the sodium in the working part while waves were also radiated. The spectra of the noise arising from the leak and the radiation were recorded with the acoustic detectors in the range 0.63-160 kHz. The measurements were performed at various temperatures, water flow rates, and radiative frequencies. Figures 4-6 show the results, which confirm the conclusions from the calculations. The largest noise extinction effect occurs at the resonant frequency (Fig. 4) for hydrogen bubbles shrinking by chemical interaction with the sodium. When water was injected at 0.2 g/sec, the attenuation at 100 kHz was comparable with the effect obtained in the absence of the leak, while the noise generated by the hydrogen bubbles did not produce an appreciable increase in the ultrasonic range. The main increase in the noise level (up to 35 dB) was in the acoustic range up to 10 kHz (Fig. 5). As the leak increases, the above saturation in the attenuation coefficient means that the noise increase predominates over the damping effect (Fig. 6).

These studies therefore indicate that the decisive effect on the acoustic-wave speed in the sodium comes from the change in compressibility arising from the formation of hydrogen bubbles when water enters the sodium. Experiment confirms that the products from the interaction of sodium with water affect the propagation of acoustic noise in the steam-generator model.

The results show that it is necessary to simulate leaks of various sizes in testing acoustic systems for monitoring industrial systems because the effects of noise generation and attenuation are difficult to predict.

#### LITERATURE CITED

1. F. A. Kozlov, G. P. Sergeev, and V. S. Yugai, *At. Energ.*, **39**, No. 6, 432 (1975).
2. P. Magee et al., in: *Proc. of IAEA Specialists Meeting on Leak Detection and Location in LMFBR Steam Generators*, Dimitrovgrad, USSR, 6-9 June, 1978, IAEA, Vienna (1978), p. 108.
3. P. Magee et al., in: *Proc. of IAEA Specialists Meeting on Leak Detection and Location in LMFBR Steam Generators*, Dimitrovgrad, USSR, 6-9 June, 1978, IAEA, Vienna (1978), p. 137.
4. J. Webber and R. Stevens, in: *Sound Propagation in Liquid Metals and Alloys: Physical Acoustics* [Russian translation], Vol. 4, Mir, Moscow (1970).
5. V. I. Subbotin et al., "Observation of the entry of water into sodium," in: *Sodium-Cooled Fast Reactor Engineering*, IAEA, Vienna (1970).
6. *Physical Principles of Ultrasonic Technology* [in Russian], Nauka, Moscow (1970).

FEATURES OF THE BEHAVIOR OF THE BOUNDARY REGIONS  
OF INTERCHANNEL PULSATIIONS

V. N. Komyshnyi, Yu. N. Kornienko,  
B. I. Kulikov, V. M. Selivanov,  
O. A. Sudnitsyn, V. I. Sharypin,  
and A. N. Yarkin

UDC 621.039.553.34

The problem of defining the conditions for the stability of the coolant-flow parameters in a system of parallel steam-generated channels still remains to be solved, despite the considerable amount of experimental and theoretical work that has gone into it [1-8]. The reason for this lies in the spate of new designs and conditions of operation in modern power-reactor systems. This makes existing recommendations inadequate. The theoretical models and computer programs [1-8] developed up to the present, used to estimate the regions of stable operation of specific installations, have only been tested over a narrow range of operating conditions, and this naturally limits their reliable use on a more general basis. To be specific, systematic experiments have not been conducted into the region of small mass rates of flow ( $\rho W < 1000 \text{ kg/m}^2 \cdot \text{sec}$ ). These are important for checking the reliability of the heat exchange at partial power levels in water-cooled water-modulated [9] and boiling-water reactors and are typical for operating conditions involving natural circulation of the coolant over wide variations in heat flow and pressure.

An experimental installation designed for such investigations included two parallel experimental sections united by input and output manifolds. Each section consisted of inlet, vertical-heating, and riser sections. The inlet section is made out of a 1-m length of 14-mm-diameter tube with a 2-mm wall, which was used to replace a Venturi and turbine flowmeter. The heated part (a 20-mm tube with 2-mm walls) is furnished with an unheated replaceable expulsion section, 12 mm in diameter. The outer tube is heated by ac at mains frequency. The conductors are capable of being moved. In the present series of tests, the length of the heated section is 1 m. The riser is made of 14-mm tube with a 2-mm wall, 1.5 m long. The inlets and outlets of each of these sections have chambers and unions for selecting pressure. The coolant used is distilled water.

The method of conducting the experiments in setting up the limits of the regions of interchannel pulsations in the  $\rho W - t_{in}$  plane consists in continuously varying the outlet temperature  $t_{in}$ , while keeping the mass rate of flow  $\rho W$ , heat flow  $q$ , and pressure  $P$  constant. The upper and lower limits of interchannel pulsation are determined in accordance with the start of the rise and damping of the amplitude of the ordered antiphase oscillations in the flow rates in both channels. Under these circumstances, the total flow rate at the inlet to the lower manifold remains constant. The temperature at the inlet to the lower manifold is varied by preheating in the range up to 25°C above saturation temperature at that pressure. The rate of change of  $t_{in}$  is 0.5-3°C/min. This proved to be minimal close to the conjectural boundary of the interchannel pulsation. Duddell oscillographs were used for continuous monitoring of the parameters, together with a scanning monitor system registering on a digital printer. The experiments were carried out in the following ranges of variations of the parameters: pressure 6.0, 12.0, 16.0 MP; heat flow 0.375, 0.5, 0.75 MW/m<sup>2</sup>; mass rates of flow from 110 to 600 kg/(m<sup>2</sup>·sec).

The boundaries of the interchannel pulsation regions are shown in Figs. 1-4. The reproducibility of the experimental points with continual passage through the boundary (according to the nature of the continuous variation in  $t_{in}$ ) was within 1°C. In order to pick out any possible influence of thermal inertia on the displacement of the interchannel pulsation boundary, the tests were carried out with both a continuous rise and also a continuous fall in  $t_{in}$ . The displacement of the interchannel pulsation curve produced in this way did not exceed 5°C at the lower limit of the value of a rate of flow being investigated, and tended to fall as the rate was increased.

---

Translated from *Atomnaya Energiya*, Vol. 54, No. 3, pp. 173-175, March, 1983. Original article submitted June 28, 1982.

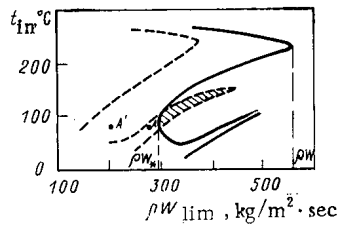


Fig. 1

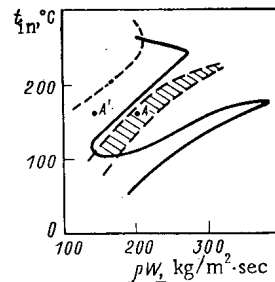


Fig. 2

Fig. 1. Boundaries of interchannel pulsation region at  $P = 6.0$  MPa; —)  $q = 0.75$  MW/m<sup>2</sup>; ----)  $q = 0.5$  MW/m<sup>2</sup>.

Fig. 2. Boundaries of interchannel pulsation region at  $q = 0.375$  MW/m<sup>2</sup>; —)  $P = 6.0$  MPa; ----)  $P = 12.0$  MPa.

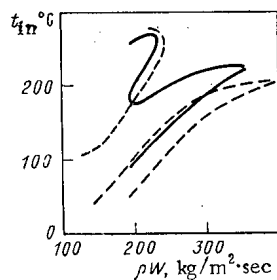


Fig. 3

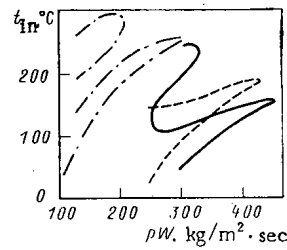


Fig. 4

Fig. 3. Boundaries of interchannel pulsation region at  $q = 0.5$  MW/m<sup>2</sup>; —)  $P = 16.0$  MPa; ----)  $P = 12.0$  MPa.

Fig. 4. Boundaries of interchannel pulsation region: —)  $P = 12.0$  MPa,  $q = 0.75$  MW/m<sup>2</sup>; ----)  $P = 16.0$  MPa,  $q = 0.75$  MW/m<sup>2</sup>; - · - · -)  $P = 16.0$  MPa,  $q = 0.375$  MW/m<sup>2</sup>; · · · ·)  $P = 12.0$  MPa,  $q = 0.375$  MW/m<sup>2</sup>.

Figures 1-4 show the existence of a range of values of mass rate of flow ( $\rho W_* < \rho W < \rho W_{lim}$ ) in which the region of instability consists of two isolated zones. Taking into account the distribution of these zones, we can consider these as being zones of pulsation in the low and high values of the outlet mass steam content  $X_{out}$ . The authors of [5] divide these zones, referring to them as "first-order" and "second order" pulsations. Reference [7] speaks out "primary" and "secondary" pulsations in the band  $\rho W_* < \rho W < \rho W_{lim}$  is qualitatively different. The first case is characterized by the output from the heated section falling periodically to the saturation temperature, while the temperature of the walls changes hardly at all. This variation is of a harmonic nature. In the second case, the wall temperature pulsations have a sawtooth waveform and are of a crisis nature.

An increase in the mass rate of flow leads to the start of a narrowing of both regions of pulsation, followed by their complete extinction at  $\rho W_{lim}$ . An increase in the heat flow at constant pressure leads to a growth in  $\rho W_{lim}$ , while an increase in pressure at constant heat flow leads to a reduction in  $\rho W_{lim}$  (see Figs. 1, 3). A series of combinations of operating parameters in the low-value region of mass rate of flow enables the limits of the union ( $\rho W_*$ ) of both pulsation zones to be clearly established. Under other conditions, such as when point A' (see Figs. 1, 2) moves to the left, e.g., the growth (attenuation) of the oscillations in flow rate were fairly insignificant, so that relating them to the boundaries of interchannel pulsation is not possible.

Figure 5 shows the boundaries of the region of first-order interchannel pulsation for pressures of 6.0 and 16.0 MPa in  $\rho W - X_{out}$  coordinates. At 6.0 MPa, the lower limit of the interchannel pulsation region lies in the zone of negative  $X_{out}$ , which confirms the destabilizing role of boiling with underheating noted in [7].

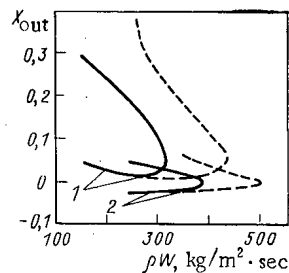


Fig. 5. Boundary of first-order interchannel pulsation region: 1)  $P = 16.0$  MPa; 2)  $P = 6.0$  MPa; —)  $q = 375$  MW/m<sup>2</sup>; - - -)  $q = 0.75$  MW/m<sup>2</sup>.

At pressure of 16.0 MPa, the lower limit of interchannel pulsation lies in zone  $X_{out} > 0$ . Here it is possible that the contribution of boiling with underheat to interchannel pulsation is insignificant.

Since the results reported in the articles on the subject do not offer a generally accepted definition of the degree of stability of the condition, as our factor defining the degree of stability for subsequent analysis we can take the distance from the operating point A to the boundary of interchannel pulsation in the chosen coordinates. The effect of the operational parameter, subject to a given variation while the remaining parameters remain fixed, will be taken as being stabilizing if this distance increases, and as being destabilizing if this distance becomes smaller. Analysis of our experimental data indicates that the influence of the operational parameters  $P$ ,  $q$ ,  $\rho W$ , and  $t_{in}$  on the operational stability will be insignificant for continuous variation. For example, the operating condition corresponding to point A (see Fig. 1,  $P = 6.0$  MPa,  $\rho W = 280$  kg/(m<sup>2</sup>·sec),  $q = 0.5$  MW/m<sup>2</sup>) is unstable, while point A' [ $\rho W = 220$  kg/(m<sup>2</sup>·sec)] is stable. In this case, the reduction in  $\rho W$  is the stabilizing factor corresponding to point A. For the case of point A', the destabilizing factor is both a reduction and an increase in the mass rate of flow, i.e., the influence of the mass rate of flow is insignificant. The same figure also shows cross hatched the part of the region of interchannel pulsation that changes to a stable condition with an increase in heat flow from 0.5 to 0.75 MW/m<sup>2</sup>; in this case, the influence of heat flow stabilizes the system. Figure 2 shows cross hatched the region of interchannel pulsation that changes into a stable region with a reduction of pressure to 6 MPa, i.e., a reduction in pressure is the stabilizing factor. We can see from Figs. 1-4 that conditions exist for which a reduction in heat flow and an increase of flow and pressure are stabilizing factors. These results do not contradict the experimental data regarding interchannel pulsation boundaries [7, 8].

Reference [7] estimates the influence of the operational parameters on the stability of the system from the variation in the total area of the interchannel pulsation regions in  $\rho W - t_{in}$  coordinates or, more roughly, the region of stability is defined as the semiplane in which  $\rho W \geq \rho W_{lim}$ . In this case, the stability of a specific condition (or even a region of operating conditions) remains an open question, together with the degree of proximity of the conditions to the boundary of the interchannel pulsation region.

Consequently, the influences (stabilizing or destabilizing) of each of the operational parameters (pressure, mass rate of flow, heat flow, and inlet temperature) are also single-valuedly defined by the position of the operating point relative to the region of interchannel pulsation. We can see from this that the position set out in the standard method of hydraulic design for a boiler plant [10] is not universally applicable.

#### LITERATURE CITED

1. F. M. Mitenkov and B. I. Motorov, Mechanisms of Unstable Processes in Thermal and Nuclear Power Engineering [in Russian], Atomizdat, Moscow (1981).
2. I. I. Gerliga and V. A. Morozov, Instability of Boilers [in Russian], Atomizdat, Moscow (1969).
3. E. P. Serov and B. P. Korol'kov, Dynamics of Steam Generators [in Russian], Énergiya, Moscow (1972).
4. V. B. Khabenskii et al., in: Achievements in the Investigation of Heat Exchange and Hydraulics of Two-phase Flows in the Components of Power Plant [in Russian], Nauka, Moscow (1973).
5. V. V. Dolgov and O. A. Sudnitsyn, Teploenergetika, No. 3, 36 (1965).
6. Heat Transmission in Two-phase Flow [in Russian], Énergiya, Moscow (1980).
7. E. B. Burlakov, G. E. Maslov, and V. I. Smolin, Voprosy Atomnaya Nauki i Tekhniki, Ser. Tekh. Yad. Reaktorov, No. 1/21, 17 (1978).

8. A. P. Proshutinskii and A. G. Lobachev, *Teploenergetika*, No. 3, 51 (1979).
9. A. Alpatov and A. Gusalov, *Kernenergie*, 20, No. 7, 217 (1977).
10. *Hydraulic Design of Boilers (Standard Method)* [in Russian], Énergiya, Moscow (1978).

## ASYMPTOTIC EXPANSION OF THE SOLUTION OF KINETIC EQUATIONS FOR SLOWLY VARYING REACTIVITY

A. A. Shepelenko

UDC 621.039.51

The dynamics of systems including a nuclear reactor as the object of control are often investigated by means of a computational experiment. The known algorithms [1, 2] provide rapid solution of the Cauchy problem on modern computers for the kinetic equations of the reactor, which form part of the mathematical model of the system. However, the efficiency of the experiment is determined mainly by the possibilities of organizing a series of variant calculations and ordering the results obtained in a form allowing purposeful optimization of the given system to be performed. The efficiency of computational experiments may be increased by the rational use, for their organization, of analytical solutions that sufficiently completely reflect the kinetic properties of the reactor. However, accurate solutions are known for a limited range of functional dependences of the reactivity on the time and take a form that make it difficult to find numerical results [1, 2]. Approximate solutions [3, 4] obtained by the WKB method only take account of one group of delayed neutrons, which is inadequate for description of the kinetics in the region between the critical values for delayed and instantaneous neutrons. The solution of [5] constructed by heuristic means does not have rigorous estimates of the character of the approximation and its accuracy.

In the present work, the method of asymptotic resolution of the system of differential equations [6] is used to construct an approximate solution of the kinetic equations of a point reactor (without constraints on the number of groups of delayed neutrons) for slowly varying reactivity in the form of asymptotic series. The formally slow rate of change in the reactivity corresponds to the "slow time"  $\tau = \alpha t$  ( $\alpha$  is a small parameter and  $t$  is ordinary time) as the argument of the reactivity  $r = r(\tau)$ . The parameter  $\alpha$  is only necessary in the process of constructing the asymptotic expansion when  $\alpha \rightarrow 0$ ;  $\alpha = 1$  must be assumed in the final result.

For the well-known kinetic equations

$$\begin{aligned} dx/dt &= Ax + Q; \quad \varepsilon = \Lambda\beta^{-1}; \quad \sum_i b_i = 1; \\ x &= \begin{bmatrix} n \\ h_1 \\ h_2 \\ \dots \end{bmatrix}; \quad A = \begin{bmatrix} \varepsilon^{-1}(r-1)\varepsilon^{-1}b_1\varepsilon^{-1}b_2\dots \\ \lambda_1 & -\lambda_1 & 0 & \dots \\ \lambda_2 & 0 & -\lambda_2 & \dots \\ \dots & \dots & \dots & \dots \end{bmatrix}; \\ Q &= \begin{bmatrix} \varepsilon^{-1}q \\ 0 \\ 0 \\ \dots \end{bmatrix} \end{aligned} \quad (1)$$

(here  $\Lambda$  and  $\beta$  are the generation time of the instantaneous neutrons and the total proportion of delayed neutrons;  $n$ , neutron density;  $\lambda_i$ ,  $\varepsilon^{-1}\lambda_i^{-1}b_i h_i$ , and  $b_i$ , decay constant, density of precursors, and relative proportion of delayed neutrons of the  $i$ -th group; and  $\varepsilon^{-1}q$ , external neutron source), the matrix  $G = \|g_{ij}\|$  is also found, as well as the diagonal matrix  $D$  and the vector  $S$ , so that the solution of Eq. (1) may be written in the form

$$x = VGz; \quad \frac{dz}{dt} = Dz + S, \quad (2)$$

Translated from *Atomnaya Énergiya*, Vol. 54, No. 3, pp. 175-177, March, 1983. Original article submitted August 5, 1982.

where  $V = \| v_{ij} \|$  is a nonspecific matrix reducing matrix  $A$  to the diagonal form  $P = V^{-1}AV$ . The elements of the principal diagonal of matrix  $P$  are the roots  $p_k$  of the characteristic equation of matrix  $A$

$$r = p_k \left[ \varepsilon + \sum_i b_i (p_k + \lambda_i)^{-1} \right]. \quad (3)$$

Substituting Eq. (2) into Eq. (1) and equating the coefficients with the vectors  $z^0$  and  $z^1$ , we obtain the matrix identity

$$PG = GD + \alpha \left( CG + \frac{dG}{d\tau} \right); \quad C = V^{-1} \frac{dV}{d\tau}; \quad (4)$$

$$GS = \Phi; \quad \Phi = V^{-1}Q, \quad (5)$$

which should satisfy the desired matrices  $C$  and  $D$  and the vector  $S$ . If the expansion

$$G = \sum_{m=0}^{\infty} \alpha^m G_m; \quad D = \sum_{m=0}^{\infty} \alpha^m D_m; \quad S = \sum_{m=0}^{\infty} \alpha^m S_m \quad (6)$$

is substituted into Eqs. (4) and (5), and then terms with the same power of  $\alpha$  are isolated, an infinite system of equations is obtained for determining the unknown elements of the expansions in Eq. (6). The initial elements of the expansions making the main contribution to the asymptote satisfy the equations

$$PG_0 - G_0D_0 = 0 \quad \text{and} \quad G_0S_0 = \Phi. \quad (7)$$

It follows from Eq. (7) that  $G_0$  is an arbitrary diagonal matrix which may expediently be taken as unity;  $D_0 = P$ ;  $S_0 = \Phi$ ; the other elements of the expansions are found from the equations

$$PG_m - G_mP = D_m + \sum_{j=1}^{m-1} G_j D_{m-j} + CG_{m-1} + \frac{dG_{m-1}}{d\tau}; \quad (8)$$

$$S_m + \sum_{j=1}^m G_j S_{m-j} = 0, \quad m \geq 1. \quad (9)$$

Explicit expressions for the matrix  $V$  and its inverse  $W = V^{-1}$ , necessary for the explicit representation of the solution, taking account of the identities following from Eq. (3) and in particular for the derivatives

$$p'_k = dp_k/dr = \left[ \varepsilon + \sum_i b_i \lambda_i (p_k + \lambda_i)^{-2} \right]^{-1};$$

$$\sum_k p'_k = \varepsilon^{-1}; \quad \sum_k (p_k + \lambda_i)^{-1} p'_k = 0;$$

$$\sum_k \lambda_i b_j (p_k + \lambda_i)^{-1} (p_k + \lambda_j)^{-1} p'_k = 0 \quad \text{or} \quad 1 \quad (10)$$

$$(0 \text{ when } i \neq j \text{ and } 1 \text{ when } i = j)$$

may be obtained in the form

$$v_{ik} = (\varepsilon p'_k)^{1/2}; \quad v_{ik} = \lambda_{i-1} (p_k + \lambda_{i-1})^{-1} v_{1k} \quad (i \geq 2); \quad (11)$$

$$w_{h1} = (\varepsilon p'_h)^{1/2}; \quad w_{hj} = \varepsilon^{-1} b_{j-1} (p_h + \lambda_{j-1})^{-1} w_{h1} \quad (j \geq 2). \quad (12)$$

Turning to Eqs. (8) and (9), expressions are given for the first-order corrections:  $D_1 = 0$  since the matrix  $C = \| c_{ij} \|$  is skew symmetric, in view of Eqs. (11) and (12);  $q_{iii} = 0$ ;  $q_{ijj} = (p_i - p_j)^{-1} c_{ij}$  ( $i \neq j$ );  $S_1 = -G_1 \Phi$ .

What is mainly of practical importance is the expression for the neutron density determined by the principal term of the asymptote,

$$n = \sum_k [p'_k(t)]^{1/2} \left\{ f_k(t_0) \exp \int_{t_0}^t p_k(\xi) d\xi + \int_{t_0}^t d\xi [p'_k(\xi)]^{1/2} q(\xi) \exp \int_{t_0}^t p_k(\xi) d\xi \right\}; \quad (13)$$

$$f_k = [\varepsilon n + \sum_i b_i (p_k + \lambda_i)^{-1} h_i] (p'_k)^{1/2};$$

$$f_k(t) \rightarrow f_k(t_0) \quad \text{as} \quad t \rightarrow t_0 + 0.$$

As would be expected, Eq. (13) coincides (apart from differences in notation) with the accurate solution in the case of constant reactivity [1, 2]. In the absence of an external source and with the special initial conditions  $h_i = \lambda_i (p + \lambda_i)^{-1} n$ , where  $p = p_1$  is the largest root of Eq. (3) — this case corresponds to exponential decay with a constant period  $p^{-1}$  — Eq. (13) coincides with the solution of [5]. In this case, it follows from Eq. (3) that  $f_k = 0$  with  $k = 2, 3, \dots$ , and in Eq. (13) there only remains the first term, in which  $f_1 = n (p')^{-1/2}$ . Note that if we obtain the correct formula  $rn = -q (t \rightarrow +\infty)$  describing equilibrium with a source at constant  $q \neq 0$  and  $r < 0$ , all the terms in Eq. (13) must be taken into account, and the identity  $\sum_k p^{-k} p_k' = r^{-1}$ , following from Eq. (3) must be used. In the case of variable reactivity, Eq. (13) looks especially simple in time intervals with a constant rate of change in reactivity, when the exponents in Eq. (13) are determined by the integrals

$$\int_0^r p_k(\rho) d\rho = (r-1) p_k - \frac{\varepsilon}{2} p_k^2 + p_k(0) + \frac{\varepsilon}{2} p_k^2(0) + \sum_i b_i \lambda_i \ln \frac{p_k + \lambda_i}{p_k(0) + \lambda_i}.$$

With increasing distance from the initial state, when the term corresponding to the largest root  $p$  comes to predominate in Eq. (13), it is expedient not only to have the integral form of Eq. (13), but also to use the differential expression following from Eq. (13) for the instantaneous inverse period of the reactor

$$n^{-1} \frac{dn}{dt} = p + \frac{1}{2} p'' (p')^{-1} \frac{dr}{dt}$$

and to study the reactor dynamics in the reactivity phase plane.

#### LITERATURE CITED

1. G. Flett, in: Computational Methods in Reactor Physics [in Russian], Atomizdat, Moscow (1972), p. 277.
2. D. Khetrik, Dynamics of Nuclear Reactors [in Russian], Atomizdat, Moscow (1975).
3. E. Koen, in: Proceedings of the Second Geneva Conference. Selected Papers of Foreign Scientists, Vol. III, Physics of Nuclear Reactors [in Russian], Atomizdat, Moscow (1959), p. 549.
4. S. Tan, Nucleonik, 8, No. 7, 480 (1966).
5. H. Hurwitz, Nucleonics, 5, No. 1, 61 (1949).
6. S. F. Feshchenko, N. I. Shkil', and L. D. Nikolenko, Asymptotic Methods in the Theory of Linear Differential Equations [in Russian], Naukova Dumka, Kiev (1966).

REVERSIBLE REDUCTION IN THE SHEAR MODULI OF IRON ALLOYS  
DURING IRRADIATION

É. U. Grinik and V. S. Karasev

UDC 621.039.531 : 539.67

At present we have not finally established the mechanisms responsible for the behavior of materials under irradiation, particularly at high neutron fluences. Often, the initial stages of irradiation play the decisive part in the development of radiation damage, as a defect structure is then produced whose subsequent evolution determines the radiation resistance. In some cases, internal-friction measurement provides valuable information on the behavior of the material during irradiation, which is not available in any other way.

The internal-friction method has been applied with an apparatus in a reactor channel [1] to examine the effects of neutron irradiation on the temperature dependence of the shear modulus for an iron alloy. The specimens were made from wire of diameter 1 mm with a length of 50 mm for the working part. We examined the following specimens: polycrystalline iron made by electron-beam melting of purity 99.99%, specimens of alloys Fe-<sup>11</sup>B and Fe-<sup>10</sup>B with boron contents of 0.001 and 0.003 mass % correspondingly, and single-crystal Fe-Si specimens with silicon contents of 3.0 mass %. The initial materials for producing the Fe-<sup>11</sup>B and Fe-<sup>10</sup>B specimens were electron-beam iron of purity 99.99% and crystalline boron with an impurity content of about 3%. The Fe-B products contained the following impurities: C ≤ 0.006 mass %; Mn ≤ 0.01 mass %; Si ≤ 0.025 mass %.

Before the specimens were loaded into the reactor, each was mounted in a measurement ampul and was annealed in a prototype materials-testing channel at 800°C for 1 h under a vacuum of about 13 MPa, after which the initial temperature dependence of the shear modulus was determined. The resonant frequencies of the specimens were in the range 5-8 Hz. The amplitude of the relative deformation at the surface was kept at  $5 \cdot 10^{-5}$ .

The irradiation temperature at a reactor power level of 10 MW was  $(350 \pm 20)^\circ\text{C}$ , while the fast-neutron flux density at the specimen was about  $10^{14}$  neutrons/(cm<sup>2</sup>·sec) at  $E \geq 0.1$  MeV. Periodically, as the fluence increased, we determined the temperature dependence of the shear modulus: during irradiation at 350-700°C and with the reactor not working at 60-700°C.

In these measurements on the Fe, Fe-<sup>11</sup>B, Fe-<sup>10</sup>B, and Fe-Si specimens it was found that the shear modulus in the temperature range  $(0.25-0.5)T_{\text{mp}}$  during irradiation was much lower than before and after it. Figure 1 shows that the reduction in the modulus is reversible and occurs only during neutron irradiation. The effect was examined up to fluences of about  $10^{21}$  neutrons/cm<sup>2</sup>. The maximum reduction in the modulus by the reactor irradiation was about 10% (Fig. 2). A similar effect has been observed previously [2, 3] for nickel and iron specimens.

The shear modulus  $G_p$  can be put in the form

$$G_p = G - \Delta G_p, \quad (1)$$

where  $G$  is the value for an unirradiated specimen, and  $\Delta G_p$  is the change in the modulus produced by the irradiation.

The shear modulus of an irradiated specimen is usually higher than the initial value [4], whereas Fig. 1 shows that it is below the initial value on neutron irradiation. Therefore,  $\Delta G_p$  can be put in the following form (Fig. 1a) for specimens irradiated to a given fluence:

$$\Delta G_p = \Delta G_p^{\text{res}} - \Delta G_p^{\text{rev}}, \quad (2)$$

Translated from *Atomnaya Énergiya*, Vol. 54, No. 3, pp. 177-179, March, 1983. Original article submitted April 16, 1982.

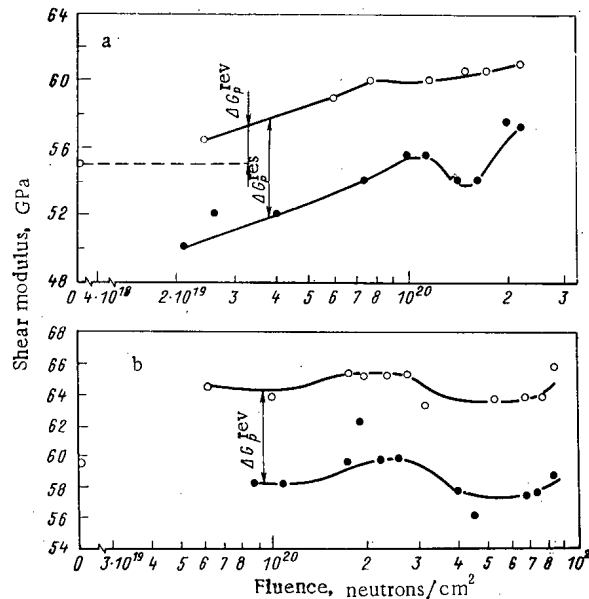


Fig. 1. Effects of fast-neutron fluence ( $E \geq 0.1$  MeV) on the shear moduli of iron at 580°C (a) and Fe-<sup>11</sup>B at 520°C (b): ●) during irradiation; ○) with the reactor shut down.

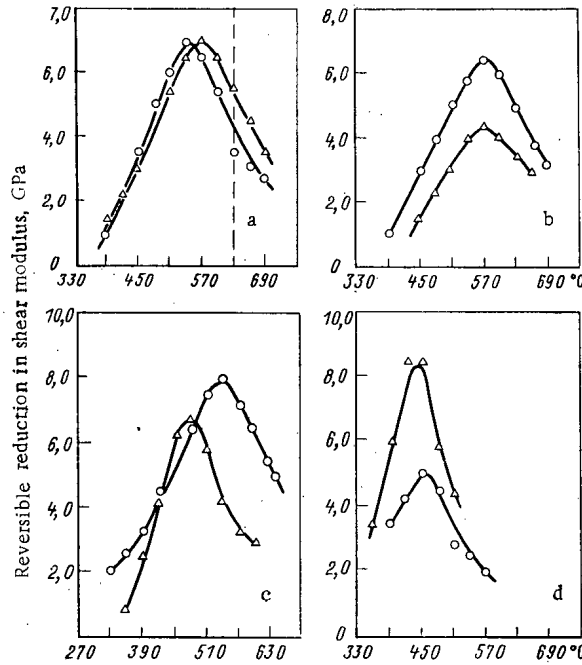


Fig. 2. Temperature dependence of the reversible reduction in shear modulus: a) polycrystalline iron at neutron fluences of  $2.4 \cdot 10^{19}$  (○) and  $6 \cdot 10^{19}$  neutrons/cm<sup>2</sup> (Δ); ---) temperature of grain-boundary maximum in internal friction  $T_N$ ; b) specimens of polycrystalline iron (○) at a fluence of  $1.5 \cdot 10^{20}$  neutrons/cm<sup>2</sup> and for a single crystal of silicon iron (Δ) at a fluence of  $0.4 \cdot 10^{20}$  neutrons/cm<sup>2</sup>; c) Fe-<sup>11</sup>B specimen at neutron fluences of  $1 \cdot 10^{20}$  (Δ) and  $5 \cdot 10^{20}$  neutrons/cm<sup>2</sup> (○); d) Fe-<sup>10</sup>B specimen at neutron fluences of  $0.6 \cdot 10^{20}$  (Δ) and  $1.0 \cdot 10^{20}$  neutrons/cm<sup>2</sup> (○).

TABLE 1. Experimental Values of the Coefficients A and B in (3) for the Temperature Dependence of the Reversible Reduction in Shear Modulus for Various Neutron Fluences

Specimen	Neutron fluence, $10^{20}$ neutrons/cm <sup>2</sup>	A, MPa/°K	B, °K
Fe	0,24	41,5	630
Fe	0,6	39	630
Fe	1,5	33,4	630
Fe- <sup>11</sup> B	1,0	57,5	620
Fe- <sup>11</sup> B	5,0	36,7	580
Fe- <sup>10</sup> B	0,6	68,2	580
Fe- <sup>10</sup> B	1,0	27,8	540
Fe-Si	0,4	25	660

where  $\Delta G_p^{res}$ ,  $\Delta G_p^{rev}$  are the irreversible or residual and reversible parts of the radiation-induced change. Usually, the change in modulus for a previously irradiated material is ascribed to the fixing of dislocations by radiation defects, and then  $\Delta G_p^{res} > 0$  [4-6].

We now consider the reversible reduction during neutron irradiation. At the temperatures of the grain-boundary maxima in the internal friction there is considerable relaxation in the shear modulus [7]. However, the observed effect cannot be explained by accentuated grain-boundary relaxation, since experiment shows that the maximum value of  $\Delta G_p^{rev}$  in these materials is attained at a temperature at which grain-boundary relaxation has not yet set in (Fig. 2a). Also, experiments were made with a single crystal of silicon iron. The temperature dependence of the reversible modulus reduction differed little from the analogous relationship for polycrystalline iron specimens (Fig. 2b), which confirms that the reversible reduction under irradiation is not related to grain-boundary relaxation. Final confirmation of the effect was provided by experiments on the Fe-<sup>11</sup>B, Fe-<sup>10</sup>B specimens. The experiments showed that the boron has a marked effect on grain-boundary relaxation: The temperature of the grain-boundary maximum in the internal friction alters from 630°C for pure iron specimens to 530°C for specimens containing boron. Figures 2c, d show that the boron has virtually no effect on the reversible part of the radiation reduction.

The appreciable reversible reduction in the modulus cannot be explained by increase in the point-defect concentration during neutron irradiation, because an increase in the vacancy concentration by 1% reduces the modulus by 1%, while an increase in the interstitial-atom concentration raises the modulus [6].

Since  $\Delta G_p^{rev}$  is independent of the neutron-flux density, the change in  $\Delta G_p^{rev}$  for nickel was ascribed [3] to preferential diffusion of interstitial atoms to mobile dislocations. Then an expression of the following form was obtained for the rising branch of the temperature dependence

$$\Delta G_p^{rev} = -A(T - B), \quad (3)$$

where T is specimen temperature and A and B are coefficients that are dependent in a complicated way on the rate of production of displacements, the flux density, and the fluence.

The experimental data (Fig. 2) show that at  $(0.25-0.4)T_{mp}$  the rising branches of the temperature dependence of  $\Delta G_p^{rev}$  are actually described by expressions of the form of (3), while A and B have the values given in Table 1.

Table 1 shows that the values of A and B for iron and its alloys in this fluence range are 27-70 MPa/deg K, correspondingly. At  $T \geq (0.4-0.5)T_{mp}$  there is a reduction in  $\Delta G_p^{rev}$ , which may be explained by an increased influx of vacancies into the dislocation-displacement zone.

#### LITERATURE CITED

1. É. U. Grinik, V. S. Karasev, and M. I. Paliokha, Nuclear Science and Engineering: Series Atomic Materials Science [in Russian], Issue 1 (1) (1978), p. 25.
2. É. U. Grinik et al., At. Energ., 34, No. 5, 397 (1973).
3. V. S. Karasev et al., Nuclear Science and Engineering: Series Fuel and Constructional Materials [in Russian], Issue 2 (1975), p. 21.

4. D. Thompson and V. Pare, in: Physical Acoustics [Russian translation], Vol. 3, Part A, Mir, Moscow (1969), p. 347.
5. A. Sosin and D. Kiefer, in: Microplasticity [Russian translation], Metallurgiya, Moscow (1972), p. 130.
6. A. C. Damask and G. J. Dienes, Point Defects in Metals [Russian translation], Mir, Moscow (1966).
7. V. S. Postnikov, Internal Friction in Metals [in Russian], Metallurgiya, Moscow (1974).

## MECHANISM OF THE TUBULAR DIFFUSION OF HELIUM

A. V. Subbotin

UDC 621.039.633

An interesting feature of pore development in the annealing of pure metals preliminarily irradiated with helium is the markedly increased mean pore size at dislocations [1]. This phenomenon may be explained by tubular diffusion of helium atoms in the pores.

In fact, in conditions of prolonged annealing, the solution of vacancies in the lattice is in equilibrium with the dislocations, and hence the chemical potential of the vacancies is zero. In consequence, in the absence of helium, the pores are in conditions of solution (infinitely large critical dimension), regardless of their positions with respect to the dislocations. In the presence of helium in the lattice, however, its admission into the pores is a stimulatory cause of their development. In this case the pore position with respect to the dislocations is significant — the contribution of the tubular-diffusion mechanism of helium considerably increases its intake into the pores at dislocations.

It is known that the vicinity of the dislocation core is characterized by elevated mobility of point defects, impurity atoms, and gas in the direction along the line of the dislocation [2]. The energy of migration along the dislocation lines, according to the estimate of [3], is approximately half the energy of migration in the unperturbed lattice.

With regard to motion in the direction normal to the dislocations, these regions are characterized by considerably smaller mobility of the diffusing agent and, in addition, may be separated from the unperturbed lattice by a small potential barrier [4]. This difference in the absolute values and symmetry of mobility for a regular lattice and the regions adjacent to dislocations leads to the appearance of the tubular-diffusion mechanism: The diffusing atoms incident in the region adjacent to a dislocation are held there to a certain extent by the potential barrier and migrate with increased velocity along the dislocation. The path of the diffusing atom along the dislocation may amount to many thousands of lattice constants before the atom returns to the unperturbed lattice. If the chemical potential of the diffusing atom is changed here (e.g., the dislocation leaves the surface, or intersects a pore), there arises a direction flux along the dislocation line sustained by the influx of atoms from the lattice to the dislocation.

In experiments on the annealing of samples preliminarily irradiated with helium, the pores exist in a two-component solution of vacancies (of concentration  $C_V$ ) and helium atoms (of concentration  $C_g$ ). The development of a pore consisting of  $n(t)$  vacancies and  $x(t)$  helium atoms at time  $t$  is expediently considered in the plane  $(n, x)$  [5] (Fig. 1) with the equations of motion

$$\frac{dn}{dt} = 3 \left( \frac{4\pi}{3\Omega} \right)^{2/3} n^{1/3} D_V \left[ C_V - C_{V_0} \exp \left( \frac{2}{3} \xi_V n^{-1/3} - \frac{x}{n} \right) \right], \quad (1)$$

$$\left( \frac{dx}{dt} \right)_V = 3 \left( \frac{4\pi}{3\Omega} \right)^{2/3} n^{1/3} D_g [C_g - C_{ge}(x, n)], \quad (2)$$

$$\xi_V = 4\pi \left( \frac{3\Omega}{4\pi} \right)^{2/3} \frac{\sigma}{kT},$$

where  $D_g$  and  $D_V$  are the diffusion coefficients of helium and vacancies, respectively;  $C_{ge}(x, n)$ , equilibrium helium concentration at the boundary of a pore with  $n$  vacancies and  $x$  helium atoms [6];  $C_{V_0}$ , thermal-equilibrium concentration of vacancies;  $\sigma$ , pore surface energy; and  $\Omega$ , elementary volume.

Translated from *Atomnaya Energiya*, Vol. 54, No. 3, pp. 179-183, March, 1983. Original article submitted May 28, 1982.

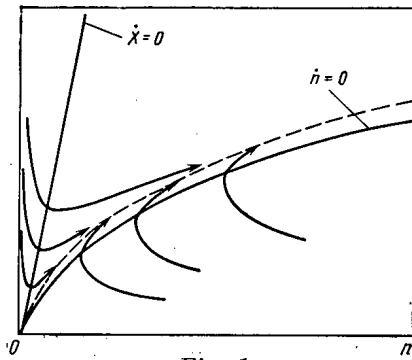


Fig. 1

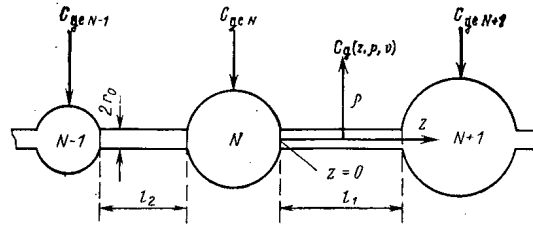


Fig. 2

Fig. 1. Diagram of helium-pore development. The lines with arrows are the trajectories of motion (development) of pores;  $n = 0$  corresponds to the trajectory  $x = (2/3)\xi_V n^{2/3}$ .

Fig. 2. Pores  $N-1$ ,  $N$ , and  $N+1$  connected by dislocational segments of length  $l_1$  and  $l_2$ ;  $C_{geN-1}$ ,  $C_{geN}$ ,  $C_{geN+1}$  are the equilibrium helium concentrations at the pore boundaries.

Since it is always the case that  $D_V C_V \gg D_g C_g$  [5], pore development in experiments on annealing characterized by the condition  $C_V \sim C_{V0}$  is only possible close to trajectories  $n = 0$  of the form [7]

$$x = \frac{2}{3} \xi_V n^{2/3}. \quad (3)$$

In other words, a determining factor in pore development is the rate of helium admission into the pore, i.e.,

$$\frac{dn}{dt} = \frac{n^{1/3}}{\frac{4}{9} \xi_V} \left( \frac{dx}{dt} \right)_V. \quad (4)$$

For pores in unperturbed regions of the lattice, the determining factor is the rate of outflow of helium from the volume. Pores at dislocations absorb helium by two means: from the volume - Eq. (2); and by tubular diffusion. If the helium flux into the pore determined by tubular diffusion is denoted by  $2J_p$ , the expression for the growth rate of a pore at a dislocation may be written in the form

$$\frac{dn}{dt} = \frac{n^{1/3}}{\frac{4}{9} \xi_V} \left[ \left( \frac{dx}{dt} \right)_V + 2J_p \right]. \quad (5)$$

**Tubular Diffusion.** The flux of gas atoms into the pore  $N$  due to the tubular-diffusion mechanism is now determined, considering the segment of dislocations joining pores  $N$  and  $N+1$  as a tube of length  $l_1$  and radius  $r_0 \approx 2b$ , where  $b$  is the Burgers vector (Fig. 2). Two diffusion coefficients are introduced for the region of the dislocation tube: longitudinal  $D_z = D_{z0} \exp(-E_z^m/kT)$  and transverse  $D_\rho = D_{\rho0} \exp(-E_\rho^m/kT)$ , ( $D_z \gg D_g \gg D_\rho$ ). In the discussion, account is taken of the energy barrier  $E_b$  for the gas atoms returning to the volume and also of the energy of the dilatational interaction of the helium atom with the dislocation [8] in regions outside the dislocational tube ( $\rho \geq r_0$ )

$$E(\rho, \vartheta) = kT \frac{L \sin \vartheta}{\rho}; \quad L = \frac{\mu b(1+\nu) \Delta \Omega}{3\pi(1-\nu) kT}, \quad (6)$$

where  $\mu$  is the shear modulus;  $\nu$ , Poisson's ratio;  $\Delta \Omega$ , dilatational volume produced by the helium atom;  $\vartheta$ , angle measured from the slip plane of the dislocation; and  $\rho$ , distance from the center of the dislocational core ( $\rho \geq r_0$ ).

The closed system of equations allowing the flux of helium atoms into the pore  $J_p$  to be determined consists of Eqs. (7) and (8) for the gas concentration in the volume  $C_z(z, \rho, \vartheta)$  and in the tube  $C(z, \rho, \vartheta)$ , the correlational conditions between them in Eqs. (9) and (10), and the boundary conditions in Eqs. (11)-(13)

$$\Delta C_g + \frac{1}{kT} \nabla E \nabla C_g = 0, \quad (7)$$

$$D_\rho \left( \frac{1}{\rho} \frac{\partial}{\partial \rho} \left( \rho \frac{\partial C}{\partial \rho} \right) + \frac{1}{\rho^2} \frac{\partial^2 C}{\partial \rho^2} \right) + D_z \frac{\partial^2 C}{\partial z^2} = 0. \quad (8)$$

In the quasisteady case considered, the flux through the tube boundary must be continuous, and hence

$$\frac{D_g C_g}{kT} (\nabla \mu_g i_\rho) \Big|_{\rho=r_0+0} = D_\rho \frac{\partial C}{\partial \rho} \Big|_{\rho=r_0-0}, \quad (9)$$

where  $\mu_g = kT \ln C_g/C_0 + E$  is the chemical potential of the helium atom in the lattice;  $C_0$ , thermal-equilibrium concentration of helium; and  $i_\rho$ , unit vector in the direction of  $\rho$ .

The amount of gas passing through the side surface of the dislocational tube from the volume should be equal (taking account of emission into the volume) to the amount of gas passing through the end ( $z = 0, l_1$ ) cross sections of the tube into pores  $N$  and  $N + 1$ , i.e.

$$r_0 \int_0^{l_1} \int_0^{2\pi} \frac{D_g C_g}{kT} (\nabla \mu_g i_\rho) \Big|_{\rho=r_0+0} d\vartheta dz = \int_0^{l_1} \int_0^{2\pi} D_z \left[ \frac{\partial C}{\partial z} \Big|_{z=0} - \frac{\partial C}{\partial z} \Big|_{z=l_1} \right] \rho d\rho d\vartheta. \quad (10)$$

The boundary condition determining the concentration  $C_g$  far from the tube ( $\rho = L_d$ ), where  $L_d$  is half the mean distance between dislocations ( $L_d \approx n_d^{-1/2}$ ;  $n_d$  is the dislocation density), under the assumption that the position of the gas pores at dislocations weakly influences  $C_g(z, L_d, \vartheta)$ , takes the form

$$C_g(z, \rho, \vartheta) \Big|_{\rho=L_d} = \bar{C}_g. \quad (11)$$

Since equilibrium values of the gas-atom concentrations  $C_{geN}$  and  $C_{geN+1}$  are maintained at the surface of pores  $N$  and  $N + 1$ , the chemical potential at the pore surface is constant. Equating the expressions for  $\mu_g$  at the external surface of the dislocational tube when  $z = 0, l_1$  to the corresponding expressions for the chemical potential of the pore surface far from the point of intersection with the dislocational tube ( $E = 0$ ), two boundary conditions are obtained:

$$C_g(z, \rho, \vartheta) \Big|_{\substack{z=0 \\ \rho=r_0+0}} = C_{geN} \exp \left[ -\frac{E(r_0, \vartheta)}{kT} \right]; \quad (12)$$

$$C_g(z, \rho, \vartheta) \Big|_{\substack{z=l_1 \\ \rho=r_0+0}} = C_{geN+1} \exp \left[ -\frac{E(r_0, \vartheta)}{kT} \right]. \quad (13)$$

The system in Eqs. (7)-(13) may be solved very simply if it is taken into account that the length of the helium-atom discontinuity in the lattice is comparable with the dimensions of the dislocational-tube cross section. Therefore, the distribution of gas atoms over the tube cross section may be regarded as uniform, and  $C(z)$  may be considered rather than  $C(z, \rho, \vartheta)$ . In turn, this allows the system in Eqs. (7)-(13) to be reformulated, determining the helium flux density in the dislocational tube and from it, and introducing them in the form of sources uniformly distributed over the tube cross section in Eq. (8). In addition, it is necessary to determine the boundary conditions at the ends of the tube ( $z = 0, l_1$ ), using Eqs. (9), (12), and (13).

Consider the process in which a helium atom leaves the tube. The flux density takes the form

$$j(z, r_0, \vartheta) = C(z) \nu r_0 \exp \left[ -\frac{E(r_0, \vartheta) + E_b}{kT} \right], \quad (14)$$

where  $\nu = 4D_\rho/r_0^2$  is the frequency at which helium atoms in the tube approach its surface. Then the flux through the side surface of the tube per unit length

$$J_1 = r_0 \int_0^{2\pi} j(z, r_0, \vartheta) d\vartheta = Z_p D_\rho C(z), \quad (15)$$

where  $Z_p = 8\pi I_0(L/r_0) \exp(-E_b/kT)$ ;  $I_0(L/r_0)$  is a Bessel function with an imaginary argument.

To determine the flux  $J_2$  from the volume into the tube, it is expedient to consider Eq. (7) with the boundary condition in Eq. (11) and the second boundary condition — the concentration at the external surface  $\tilde{C}(z, \vartheta)$  determined by the "transmission capability" of the dislocational tube. If  $C(\rho, z, \vartheta)$  for  $\rho \geq r_0$  is written in the form of a superposition of the two concentrations  $C_1(\rho, z, \vartheta) + C_2(\rho, z, \vartheta)$  satisfying Eq. (7) and the boundary conditions

$$C_1(\rho, z, \vartheta) \Big|_{\rho=L_d} = 0; \quad C_1(\rho, z, \vartheta) \Big|_{\rho=r_0+0} = \tilde{C}(z, \vartheta); \quad (16)$$

$$C_2(\rho, z, \vartheta) \Big|_{\rho=L_d} = \bar{C}; \quad C_2(\rho, z, \vartheta) \Big|_{\rho=r_0+0} = 0, \quad (17)$$

it may readily be established that the solution for  $C_1$  gives Eq. (15) for the flux density from the dislocational tube, while the conditions formulated for  $C_2$  are identical to the formulation of the problem on the flux of point defects to the dislocation in the case of the diffusional controlled absorption mechanism.

Following [9], the expression for the gas-atom flux from the volume to the tube disregarding the inverse flow determined above - see Eq. (15) - may be written in the form

$$J_z = Z_d D_g \bar{C}_g, \quad (18)$$

where

$$Z_d = \frac{2\pi I_0 (L/2r_0)}{K_0 (L/2L_d) I_0 (L/2r_0) - K_0 (L/2r_0) I_0 (L/2L_d)}.$$

Now, on the basis of Eqs. (15) and (18) and also Eq. (8), a reformulated equation is written for the helium concentration in the dislocational tube:

$$\frac{d^2}{dz^2} C(z) - \frac{Z_p D_\rho}{\pi r_0^2 D_z} C(z) + \frac{Z_d D_g}{\pi r_0^2 D_z} \bar{C}_g = 0. \quad (19)$$

It follows from Eq. (15) that the diffusional-displacement length of the helium atom in the tube takes the form

$$l_\tau = \sqrt{\frac{\pi r_0^2 D_z}{Z_p D_\rho}} = \frac{r_0}{2} \sqrt{\frac{D_z}{D_\rho} \frac{\exp(E_0/kT)}{2I_0(L/r_0)}}. \quad (20)$$

Considering the flux of gas atoms leaving the tube through the side surfaces in the vicinity of the ends ( $z = 0, l_1$ ) taking account of the continuity condition in Eq. (9), boundary conditions for Eq. (19) may be obtained. The expression for the flux from the tube takes the form in Eq. (15). The expression for the flux outside the tube may be obtained from Eq. (7) with the boundary condition in Eq. (12) or (13) at the internal boundary of the region ( $\rho = r_0 + 0$ ) and a zero boundary condition for  $\rho = L_d$ . The resulting expression differs from Eq. (18) only in that  $\bar{C}_g$  is replaced by  $C_{geN}$  or  $C_{geN+1}$ . Comparison of the fluxes gives the required boundary conditions

$$C(z)|_{z=0} = \frac{Z_d D_g}{Z_p D_\rho} C_{geN}; \quad (21)$$

$$C(z)|_{z=l_1} = \frac{Z_d D_g}{Z_p D_\rho} C_{geN+1}. \quad (22)$$

Solution of Eq. (19) together with the boundary conditions in Eqs. (21), (22) allows the gas distribution inside the dislocational tube to be obtained:

$$C(z) = \frac{Z_d D_g}{Z_p D_\rho} \left[ (\bar{C}_g - C_{geN}) \operatorname{ch} \left( \frac{l_1}{l_\tau} \right) - (\bar{C}_g - C_{geN+1}) \right] \frac{\operatorname{sh}(z/l_\tau)}{\operatorname{sh}(l_1/l_\tau)} - \frac{Z_d D_g}{Z_p D_\rho} (\bar{C}_g - C_{geN}) \operatorname{ch} \left( \frac{z}{l_\tau} \right) + \frac{Z_d D_g}{Z_p D_\rho} \bar{C}_g. \quad (23)$$

Using Eqs. (23) and (10), the flux of gas atoms from the dislocational tubes into pore N is found:

$$J_p = Z_d l_\tau \frac{D_g}{\Omega} \frac{(\bar{C}_g - C_{geN}) \operatorname{ch}(l_1/l_\tau) - (\bar{C}_g - C_{geN+1})}{\operatorname{sh}(l_1/l_\tau)}. \quad (24)$$

Consider  $l_\tau$ , expressing  $D_z$  and  $D_\rho$  in terms of the corresponding migration energies;  $L/r_0$  is estimated using the parameters known for nickel [10]:  $\mu = 0.94 \cdot 10^{12}$  dyn/cm<sup>2</sup> ( $0.94 \cdot 10^{11}$  Pa) and  $\nu = 0.28$  for  $\Delta\Omega \sim \Omega$ . At temperatures of  $\sim 800$ - $1100^\circ\text{K}$ , it is found that  $L/r_0 \gg 1$ , which allows the asymptotic expansion to be used for  $I_0(L/r_0)$  and  $l_\tau$  to be written in the form

$$l_\tau = \frac{r_0}{2} \left[ \frac{L}{2r_0} \right]^{1/4} \sqrt{\frac{D_{zv}}{D_{\rho 0}}} \times \exp \left( - \frac{E_z^m - E_\rho^m - E_b}{2kT} - \frac{L}{2r_0} \right). \quad (25)$$

The expression for the helium-atom flux into the pore from the dislocational tube in Eq. (14) may usefully be considered in two limiting cases:  $l_1/l_\tau \ll 1$  and  $l_1/l_\tau \gg 1$ .

In the first case

$$J_p = Z_d \left( \frac{l_1}{2} \right) D_g (\bar{C}_g - C_{geN}) + Z_d l_\tau D_g (C_{geN+1} - C_{geN}). \quad (26)$$

The first term on the right-hand side indicates that all the gas atoms absorbed by the dislocational tube from the volume enter a pore. The second term reflects the existence of strong diffusional interaction between

the pores coupled by the dislocational tube, as a result of which the large pore should absorb gas from the small pore. In fact, using [6], and also Eq. (3), it may readily be established that  $C_{ge}(x, n)$  falls with increase in pore size and hence the second term in Eq. (26) is larger than zero in the case when pore  $N + 1$  is smaller than pore  $N$ , the flux into which is also determined by  $J_p$ . Note that different mechanisms of helium migration in the lattice exist; some of these evidently lead to an extremely high value of  $l_T$ .

In the second case ( $l_T/l_1 \ll 1$ )

$$J_p = Z_d l_T D_g (\bar{C}_g - C_{geN}), \quad (27)$$

i.e., the only gas atoms entering the pore are those captured by the dislocational tube at distances from the pore of  $l_T$  or less. In the middle part of the dislocation, dynamic equilibrium is established between the gas atoms which are absorbed and those emitted into the lattice. In this case the interaction between the pores is negligibly small.

Influence of the Tubular-Diffusion Mechanism on Pore Growth. In considering pore growth at dislocations, the relation  $\Omega n = (4/3)\pi R^3$  is used and, substituting Eqs. (26) and (27) into Eq. (5), expressions are obtained for the rate of pore growth in two limiting cases. Note here that the fluxes into pore  $N$  from two dislocational tubes are taken into account (see Fig. 2):

$$\frac{dR}{dt} = \frac{3}{4} \left( \frac{kT}{\sigma\Omega} \right) \left[ 1 + \frac{l_T}{R \ln(2L_d/L)} \right] D_g (\bar{C}_g - C_{geN}), \quad \frac{l_T}{l} \ll 1; \quad (28)$$

$$\frac{dR}{dt} = \frac{3}{4} \left( \frac{kT}{\sigma\Omega} \right) \left\{ \left[ 1 + \frac{l_1 + l_2}{4R \ln(2L_d/L)} \right] D_g (\bar{C}_g - C_{geN}) + \frac{l_T}{2R \ln(2L_d/L)} D_g (C_{geN+1} + C_{geN-1} - 2C_{geN}) \right\}, \quad \frac{l_T}{l} \gg 1. \quad (29)$$

It follows from Eqs. (28) and (29) that the tubular-diffusion mechanism becomes determining in pore development under the condition  $l_T/R \cdot \ln(2L_d/L) > 1$  for the case  $l_T/l \ll 1$  and the condition  $(l_1 + l_2)/4R \ln(2L_d/L) > 1$  for the case  $l_T/l \gg 1$ . The corresponding expressions for the pore growth take the form

$$\frac{dR}{dt} = \frac{3}{4} \left( \frac{kT}{\sigma\Omega} \right) \frac{l_T}{\ln(2L_d/L)} \frac{D_g}{R} (\bar{C}_g - C_{geN}), \quad \frac{l_T}{l} \ll 1; \quad (30)$$

$$\frac{dR}{dt} = \frac{3}{4} \left( \frac{kT}{\sigma\Omega} \right) \frac{l_1 + l_2}{4 \ln(2L_d/L)} \frac{D_g}{R} (\bar{C}_g - C_{geN}) + \frac{3}{4} \left( \frac{kT}{\sigma\Omega} \right) \frac{l_T}{2 \ln(2L_d/L)} \frac{D_g}{R} (C_{geN+1} + C_{geN-1} - 2C_{geN}), \quad \frac{l_T}{l} \gg 1. \quad (31)$$

In considering pore kinetics in the later stages ( $\bar{C}_g \sim C_{ge}$ ), in view of the condition  $l_T/l \gg 1$ , only the last term remains in Eq. (31):

$$\frac{dR}{dt} \approx \frac{3}{4} \left( \frac{kT}{\sigma\Omega} \right) \frac{l_T}{2 \ln(2L_d/L)} \frac{D_g}{R} (C_{geN+1} + C_{geN-1} - 2C_{geN}), \quad (32)$$

and hence the interaction between neighboring pores will be the main mechanism of pore development.

In contrast to the well-known cases of kinetics in the later stages, in the volume, or in a plane, when a critical dimension that is the same for the whole ensemble of developing particles exists in the system [7, 11-13], it follows from Eq. (32) that the critical size of each pore is determined by the dimensions of the two neighboring pores. This must obviously lead to a significant difference between the laws of development of pore ensembles at an arbitrarily chosen dislocation and in an unperturbed lattice.

## CONCLUSIONS

The observation of differences in pore development at dislocations and in the volume of the lattice evidently allows definite information to be obtained on the mechanism of helium-ion migration. In fact, it follows from Eqs. (30), (32) that the growth of pores at dislocation depends cardinally on  $l_T$ . According to Eq. (25),  $l_T$ , in turn, is extremely sensitive to the migration energy and the binding energy, which depend directly on the mechanism of helium migration.

As an illustration of this, assume that the migration of helium occurs over interstitial positions both in the lattice and in the dislocational tube. This case corresponds to a migration energy  $E^m \approx 0.08$  eV [14] and  $\Delta\Omega \sim \Omega$ . The binding energy of the helium atom with the edge of the dislocation should be somewhat less than the binding energy with a vacancy [14]; assume that  $E_b \approx 1$  eV. In this case, Eq. (25) gives  $l_T \sim b$ , and hence the contribution of tubular diffusion in the migration of helium over interstitial positions is negligibly small; consequently, the pores must develop in the same way, regardless of whether they are in a volume or at dislocations. At the same time, the considerable differences noted in [1] between the mean pore sizes at dislocations and in the volume evidently permit the conclusion that the mechanism of helium migration over interstitial positions is not the main mechanism.

It remains to thank Yu. N. Sokurskii and G. A. Arutyunova for fruitful discussions.

#### LITERATURE CITED

1. G. Arutyunova (Arutyunova) et al., *J. Nucl. Mater.*, **110**, No. 1, 65 (1982).
2. P. Shewmon, *Diffusion in Solids*, McGraw-Hill, New York (1963).
3. J. Lothe, *J. Appl. Phys.*, **31**, 1077 (1960).
4. A. Mortlock, *Acta Met.*, **8**, 132 (1960).
5. K. Russell, *Acta Met.*, **26**, 1615 (1978).
6. K. Russell, *Acta Met.*, **20**, 899 (1972).
7. V. V. Slezov and Z. K. Saralidze, *Fiz. Tverd. Tela*, **7**, No. 6, 1605 (1965).
8. P. Heald and M. Speight, *Acta Met.*, 1380 (1975).
9. I. G. Margelashvili and Z. K. Saralidze, *Fiz. Tverd. Tela*, **15**, No. 9, 2665 (1973).
10. R. Johnson, *Philos. Mag.*, **16**, 553 (1967).
11. I. M. Lifshits and V. V. Slezov, *Zh. Eksp. Teor. Fiz.*, **35**, 479 (1958).
12. L. P. Semenov, *At. Energ.*, **15**, No. 5, 404 (1963).
13. A. V. Subbotin, *At. Energ.*, **43**, No. 2, 100 (1977).
14. D. Reed, *Rad. Effects*, **31**, 129 (1977).

#### ATOMIZATION OF GOLD TARGETS BY FISSION FRAGMENTS

I. A. Baranov and V. V. Obnorski

UDC 537.226:539.173

Analysis of experimental data on atomization of materials by heavy multiply charged ions (fission fragments) [1, 2] showed that the atomization factors  $S$  assume values from  $\sim 10$  to  $\sim 5 \cdot 10^4$  atoms/fragment and greatly depend on the structure of the surface layers of the target and the average energy of the fission fragments. Of all the characteristics, in this case the most important are the size distribution of the grains of the material in the surface layers, the film thickness, and the porosity of the targets, i.e., all factors that can give rise to a size effect. In addition, the energy dependence of  $S$  for fine-grained nonconducting materials [3] permitted reliably establishing that for large  $S$  atomization occurs due to ionization losses by the heavy multiply charged ions (fission fragments).

Based on the role of fine grains in the formation of surface tracks from fission fragments in thin metallic films [4], as well as on data in [3], we proposed [5] (see also [2]) an analytic expression for determining the coefficients of the atomization of fine-grained targets by heavy multiply charged ions such as fission fragments due to ionization loss  $(dE/dx)_e$ :

$$S_{cal} = \frac{4}{3} \pi^2 N \frac{\sum_i R_i^3 f_i (1 - 1/n_i^2)}{A} \quad (1)$$

Here  $N$  is the number of atoms per unit volume;  $f_i$ , number of grains with radius  $R_i$  on the irradiated surface with area  $A$ ;  $(1 - 1/n_i^2) = P_i$ , probability of atomization of a grain with radius  $R_i$ ; and

$$n_i = (dE/dx)_e / (dE/dx)_{e, min, i}$$

Translated from *Atomnaya Énergiya*, Vol. 54, No. 3, pp. 184-188, March, 1983. Original article submitted May 24, 1982.

TABLE 1. Coefficients of Atomization of Gold Targets by Heavy Multiply Charged Ions - Fission Fragments with Energies 45-65 MeV;  $(dE/dx)_e = 24 \text{ keV/nm}$

Target characteristic	Computed amount of gold deposited, $\mu\text{g}/\text{cm}^2$	Distance between evaporator and substrate, cm	$S_{\text{exp}}$ for unheated targets, atoms/fragment	$S_{\text{exp}}$ for heated targets, atoms/fragment
Foil with thickness $20 \mu\text{m}$ [6]	-	-	No. 1, $51 \pm 12$	No. 2, $15 \pm 5$
Continuous layer with thickness $0.7 \mu\text{m}$	1400	2	No. 3, $70 \pm 18$	No. 4, $8 \pm 3$
Flat islands with dimensions $0.1 \mu\text{m}$ and thickness $90 \text{ nm}$ (see Fig. 1)	60	9	-	No. 5, $10 \pm 4$
	15	10	-	(33)
Spherical islands - grains with diameter $\sim 30\text{-}50 \text{ nm}$ ; single grains with diameter $\sim 10\text{-}20 \text{ nm}$ are present (see Fig. 2)	60	8	No. 7, $1300 \pm 250$ (2100)	No. 6, $42 \pm 3$ (60)
Discontinuous layer with variable thickness $10\text{-}60 \text{ nm}$ (see Fig. 3)	1.5	12.5	No. 8, $4000 \pm 600$ (12000)	-
Spherical islands - grains with diameter $4.5\text{-}7.5 \text{ nm}$ (see Fig. 4)	3	12.5	No. 9, $11000 \pm 2000$ (5500)	-
Spherical islands - grains with diameter $10\text{-}20 \text{ nm}$ (see Fig. 5)				

Remark. Targets Nos. 3-9 were prepared by thermal sputtering in a vacuum. The values of  $S_{\text{exp}}$ , obtained by rescaling for the total target area, are shown in parentheses.

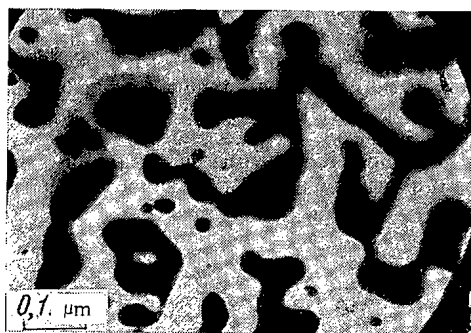


Fig. 1. Heated flat islands of gold with thickness  $\sim 90 \text{ nm}$ , target No. 5.

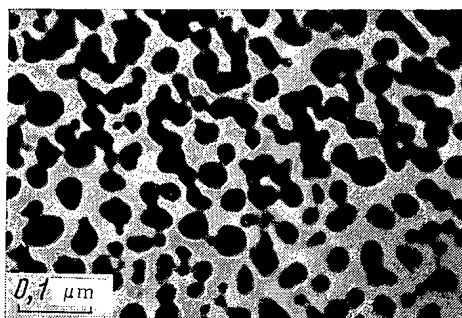


Fig. 2. Heated islands of gold with diameter  $30\text{-}50 \text{ nm}$  (single grains with smaller sizes are visible), target No. 6.

where  $(dE/dx)_{e,\text{min},i}$  is the minimum value of the ionization deceleration capability, with which the heavy multiply-charged ion, passing by at the diameter of the grain, liberates energy sufficient to atomize the grain into separate atoms. In addition, we assumed that grains of appropriate sizes ( $d < 20 \text{ nm}$ ) are atomized due to ionization by a fission fragment either completely or not at all, i.e., partial atomization of grains does not occur. This indicates the existence of an energy threshold for atomization, which depends on the radius of the

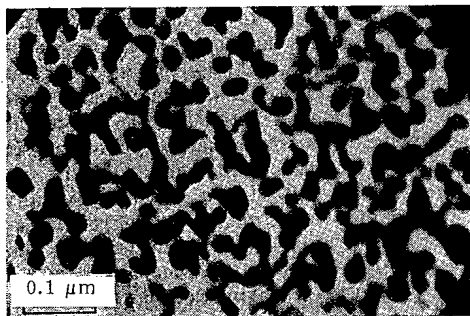


Fig. 3

Fig. 3. Discontinuous gold layer with variable thickness from  $\sim 10$  to  $\sim 60$  nm, target No. 7.

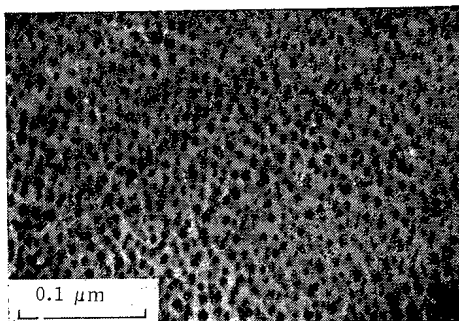


Fig. 4

Fig. 4. Gold grains with diameter 4.5-7.5 nm, target No. 8.

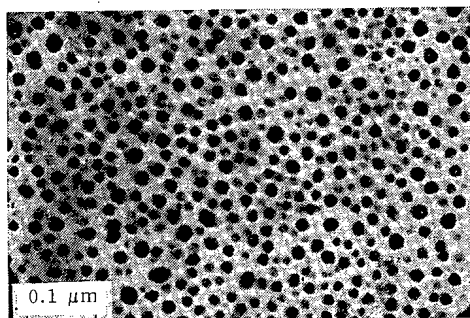


Fig. 5. Gold grains with diameter 10-20 nm, target No. 9.

grain R. Naturally, this does not concern atomization of grains due to elastic collisions, but this type of atomization can be neglected in this case, since, according to estimates in [5], for nondecelerated fission fragments  $S_{elas}$  is only several atoms per fragment. It should be noted that direct experiments in which the atomization factor would be determined for grains of specific size and in which only a single parameter would vary, namely, the structure of the targets, have not yet been performed.

In this work, under identical conditions, the atomization coefficients were measured essentially in a single experiment using the same source of fission fragments with constant geometry in an ultrahigh vacuum for gold targets in the following form: foils, i.e., massive metal; continuous sputtered layer; layer consisting of separate flat islands of different shape; layers consisting of separate spherical islands (grains with different diameter); very thin continuous film with variable thickness. For most targets, electron-microscopic photographs of the surface were obtained beforehand. Gold was chosen as the object of the investigations, because this metal does not have an oxide film and is convenient for performing activation analysis when determining the amount of atomized matter. We proposed to compare the values of  $S$ , obtained for island targets with spherical grains, with values calculated using expression (1).

#### PREPARATION OF GOLD TARGETS

Nine targets were prepared. Two targets (No. 1 and No. 2) represented specimens of massive gold made of foil with a thickness of  $20 \mu\text{m}$ . The surface of the target was chemically treated [6]. Electron-microscopic photography of replicas of the surface showed that, as previously, the dimensions of blocks or grains mainly exceed  $30 \text{ nm}$ . However, single grains were observed with dimensions less than  $20 \text{ nm}$ . To eliminate these fine grains, whose presence could lead to an overestimate of the expected small values of  $S$  [5], according to Sigmund's model [7], for massive metal [6], target No. 2 was annealed at  $550^\circ\text{C}$  for 2 h in a vacuum  $\sim 10^{-3} \text{ Pa}$ . We prepared the remaining seven targets by thermal sputtering of gold in a vacuum on carbon substrates with thickness  $\sim 15 \text{ nm}$ , deposited beforehand on titanium disks. We obtained the different thicknesses and structures of gold layers by varying the gold charge in the evaporator, the distance between the evaporator and the sub-

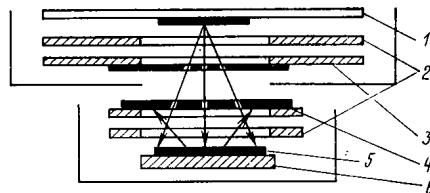


Fig. 6. Scheme of irradiation of targets by fission fragments: 1)  $^{252}\text{Cf}$  source; 2) separating ring; 3) protective nickel films; 4) nickel collector film; 5) target being atomized; 6) titanium disk.

strate, and the rate of evaporation, and by heating part of the layers in order to enlarge the grains and change their shape. We monitored the structure of the layers with the help of electron-microscopic grid markers. Targets Nos. 3, 4 consisted of continuous layers of gold with a thickness of about 700 nm; in addition, target No. 4 was annealed in order to enlarge the grains. The characteristics of the target layers are indicated in Table 1. Figures 1-5 present the electron-microscopic photographs of targets Nos. 5-9, from which it is evident that the relative fraction of the gold-covered surface of the carbon substrates constitutes 0.3, 0.7, 0.6, 0.3, and 0.2, respectively.

### IRRADIATION OF TARGETS

We used fragments of spontaneously fissioning  $^{252}\text{Cf}$  as sources of heavy multiply charged ions. We deposited californium onto a platinum disk by thermal atomization in a vacuum. The diameter of the active spot was 7 mm, the amount of californium was 4  $\mu\text{g}$ , which with a  $4\pi$  geometry provided for a flux of fission fragments equal to  $6 \cdot 10^6$  fragments/sec. We determined the amount of californium on an  $\alpha$  gun to within 5%. We determined the number of fission fragments passing through the surface of the target from published data [8]. To absorb the recoil curium nuclei, arising with the decay of  $^{252}\text{Cf}$ , and to avoid contaminating the chamber with californium, the chamber was covered through a separating ring with a nickel film with a thickness  $\sim 150$   $\mu\text{g}/\text{cm}^2$ . The same kind of nickel film was deposited through a separating ring with thickness 0.8 mm on a gold target and played the role of a collector for the atomized gold. The source of fission fragments was stationary and was situated above the target being atomized. Thus, a fission fragment, prior to falling onto the atomized surface of the corresponding target, passed through two nickel films with a total thickness of  $\sim 300$   $\mu\text{g}/\text{cm}^2$  (Fig. 6). The preparation of nickel films and the determination of their thickness with the help of an alpha spectrometer were described previously [3]. In this experiment, the collimator was not used, while the distance between the source of fission fragments and the atomized surface was 4 mm, i.e., the angular spread of fission fragments relative to the normal to the surface of the target constituted  $0-45^\circ$ . We measured the energy spectrum of the fission fragments with the help of a surface-barrier detector and a spectrometrical channel with an AI-1024 analyzer; it turned out to be somewhat diffuse and shifted into the low energy range, so that the energy of the fission fragments mainly equaled 45-65 MeV. This corresponds to an ionization decelerating capability in gold  $(dE/dx)_{\text{e cp}} \approx 24$  keV/nm [9].

We placed all nine targets covered with nickel collector-films on a disk, which could rotate without destroying the ultrahigh vacuum. Each target was placed in sequence under the source of fission fragments in accordance with the exposure chosen. To average the irradiation conditions, the disk with the targets completed several revolutions. We monitored the position of the targets visually through a heat-resistant glass. To avoid distorting the results due to the reverse atomization of gold from the collector, we chose the integrated fluxes of fission fragments taking into account the expected values of S [1, 2].

### CHAMBER WITH ULTRAHIGH VACUUM

The vacuum chamber was constructed from stainless steel with copper sealing rings. We performed the preliminary evacuation from atmospheric to  $\sim 10^{-1}$  Pa pressure using zeolite pumps. Then, over the course of several hours, we degassed the entire volume at  $400^\circ\text{C}$ . After cooling to  $200^\circ\text{C}$ , we evacuated the chamber, using a "rough" magnetodischarge NORD-250 pump, to a pressure  $10^{-4}-10^{-5}$  Pa. To evacuate the working volume of the chamber and the getter section, we used a "finishing" NORD-250 pump. After achieving a vacuum of  $5 \cdot 10^{-7}$  Pa, we vaporized the titanium in the getter section and a vacuum of  $\leq 4 \cdot 10^{-8}$  Pa was established in the working volume. In this experiment, prior to injecting air and loading the specimens, we filled the chamber

with nitrogen, and to avoid recrystallization of gold and changing the structure of the targets, we heated the chamber to 170°C. In view of the long duration of the experiment, after a vacuum  $\sim 5 \cdot 10^{-7}$  Pa was established, power was supplied to the NORD-250 pump, when necessary, from a specially developed high-voltage block, operating from the 12-V storage battery.

#### DETERMINATION OF THE AMOUNT OF ATOMIZED GOLD ON COLLECTORS

Due to the small quantity of gold on collectors ( $3 \cdot 10^{12}$ – $3 \cdot 10^{13}$  atoms or 0.001–0.01  $\mu\text{g}$ ), for the measurements we used the high-sensitivity technique of neutron activation analysis and high-resolution spectrometry.

We placed nine nickel collector-films with atomized gold, several nickel reference films with a known quantity of gold ( $\sim 0.03$ – $0.001$   $\mu\text{g}$ ), and several pure nickel films into an aluminum container and irradiated them with thermal neutrons from the reactor at the B. P. Konstantinov Institute of Nuclear Physics in Leningrad in a water channel at 60°C for 72 h. The thermal neutron flux density constituted  $\sim 10^{14}$  neutrons/( $\text{cm}^2 \cdot \text{sec}$ ). After the collector-films were irradiated in the reactor, we analyzed the reference films with the gold and the pure nickel films on a  $\gamma$  spectrometer with a liquid nitrogen-cooled Ge detector. By comparing the areas of the peaks, corresponding to an energy 412 keV ( $\gamma$  line of  $^{198}\text{Au}$ ), we determined the number of  $^{197}\text{Au}$  atoms on the collectors for the collector and reference films. Knowing the number of fission fragments passing through the surface of the targets,  $S$  can be determined for each target. The data obtained were checked by determining the absolute efficiency of detection of  $\gamma$  rays with energies of about 400 keV using standard  $\gamma$  ray sources and based on data on the neutron flux in the reactor. The values of  $S$  found in this manner are 8% higher than the values determined from the gold references, which will be presented in what follows.

#### RESULTS AND DISCUSSION

The experimentally obtained values  $S_{\text{exp}}$  for nine gold targets with different structure was presented in Table 1. The final error in the experiment depends on the following: on the error in determining the number of 412-keV  $\gamma$  quanta detected (this error was 20% for targets Nos. 1, 3, and 6, 35% for targets Nos. 2, 4, and 5, and 5% for targets Nos. 7–9); on the error in determining the number of fission fragments reaching the target, equal to 10%; and, on the error in determining the amount of gold on the reference films, which is 10% (we note that this error could be somewhat higher, since the data for the references with charges of 0.03  $\mu\text{g}$  and 0.003  $\mu\text{g}$  did not coincide).

The highest values of  $S_{\text{exp}}$ , equal to 4000 and 11,000 atoms/fragment, were obtained for targets Nos. 8 and 9 from separate grains with average diameter  $\sim 6.5$  and  $\sim 14$  nm, respectively; for target No. 6 (grain diameter 30–50 nm) this value constituted only 42 atoms/fragment. If we include the fact that the surface of targets Nos. 6, 8, and 9 is only partially covered by gold grains, then the values of  $S_{\text{exp}}$  recalculated for the entire surface will equal  $\sim 60$ ,  $\sim 12,000$ , and  $\sim 55,000$  atoms/fragment, respectively. It was assumed here that the grains do not touch one another, and in analyzing the data obtained we used the model of isolated grains.

In comparing  $S_{\text{exp}}$  for targets Nos. 6, 8, and 9 with the values calculated using Eq. (1), we assume that  $(dE/dx)_e = 24$  keV/nm, the binding energy of gold atoms is  $U_0 = 3.75$  eV, and  $N = 5.9 \cdot 10^{22}$  atoms/ $\text{cm}^3$ ; we determined  $(dE/dx)_{e,\text{min},i}$  and  $P_i$  for each  $R_i$ . It turned out that for  $(dE/dx)_e = 24$  keV/nm, according to (1), gold grains with diameter not exceeding 14.5 nm can atomize. In this connection, grain size distributions were constructed only for targets Nos. 8 and 9, since for targets Nos. 2, 4, 5, and 6 the gold grains had diameters  $\geq 30$  nm, and therefore the coefficient of atomization  $S_{\text{cal}}$  must equal zero. According to (1) and the grain size distribution, 50% of all grains, i.e., grains with diameters exceeding 14.5 nm, did not contribute to  $S_{\text{cal}}$  for target No. 1. Most grains in target No. 8 had diameters 4.5–7.5 nm, for which the probability of atomization is close to 1.0, so that  $S_{\text{cal}}$  for targets Nos. 8 and 9 constituted 2300 and 2100 atoms/fragment, respectively. Taking into account the sharp dependence of  $S_{\text{cal}}$  on  $R$ , as well as the approximations which were made in deriving expressions for  $S_{\text{cal}}$  [5], the agreement between  $S_{\text{cal}}$  for targets Nos. 8 and 9 is satisfactory. However, we note that  $S_{\text{cal}}$  for target No. 9 turned out to be a factor  $\sim 5$  smaller than  $S_{\text{exp}}$ . The total agreement between the computed and experimental values of  $S$  for target No. 9 is obtained if it is assumed that for  $(dE/dx)_e = 24$  keV/nm, grains with diameter less than 19.5, and not 14.5 nm as assumed above, can be completely atomized. This is only possible when the material is atomized due to removal not only of separate atoms, but of groups of atoms as well. In addition, much less energy is required to break up a grain. However, it should be noted that the disagreement between the computed and experimental results could be due to the inadequate accuracy with which the grain size distribution was determined (see Fig. 5), since it was determined from a single

electron-microscopic photograph, albeit with preliminary visual observation of other sections of the surface in the electron microscope. For target No. 6 the coefficient of atomization must coincide with the measured value for massive metal, since grains with diameters exceeding 20 nm must not atomize due to the energy of ionization losses, which is not sufficient for complete atomization of grains into separate atoms and, according to the isolated-grain model, partial atomization, as already mentioned, does not occur. Indeed, for target No. 6 the coefficient of atomization is more than 100 times smaller than that obtained for targets Nos. 8 and 9, although the grain diameters in the two cases indicated differ only insignificantly and constitute more than 30 and less than 20 nm, respectively. At the same time, the value obtained  $S = 42$  atoms/fragment (more correctly,  $S = 60$  atoms/fragment) exceeds by a factor  $\sim 10$  the value computed using Sigmund's cascade model [5, 7]. This is apparently related to the presence (see Fig. 2) of separate grains with diameter not greater than 20 nm on the surface of the target, which can be atomized by fission fragments due to ionization losses and which can thereby increase the measured value of  $S$ . This also explains the high, compared to the expected value for massive metals, coefficient of atomization for target No. 1, constituting 51 atoms/fragment. We note that for target No. 3 the coefficient of atomization is much less than expected [10]. Apparently, due to the small (2 cm) distance between the evaporator and the substrate, many small grains on the heated substrate (temperature was not monitored) coalesced into larger grains. The smallest values of  $S$  were obtained for the annealed foil (No. 2), annealed continuous layer (No. 4), and annealed layer consisting of quite thick ( $\sim 90$  nm) flat islands of size  $\sim 100$  nm (No. 5): 15, 8, and 10 (33) atoms/fragment, respectively. If we even assume that grains with diameters less than 20 nm were absent on the surface of these targets after annealing, then values of  $S$  still exceed by a factor of 3-7 the values found from Sigmund's cascade theory. It is possible that here the inadequate accuracy of measurements or Sigmund's equation for calculating  $S_{cal}$  had an effect or there was partial atomization of the massive metals due to ionization losses. For target No. 7,  $S = 1300$  (2100) atoms/fragment. The structure of this target is inhomogeneous; this is mainly a thin discontinuous gold film (on a carbon substrate) with variable thickness 10-60 nm, containing separate grains with diameters less than 20 nm. Apparently,  $S$  in this case is determined both by fine grains and by sections of film with thickness less than 10 nm, when the size effect can be manifested.

In conclusion we should note the following:

1. Large coefficients of atomization ( $10^3$ - $5 \cdot 10^4$  atoms/fragment) are observed only for targets consisting of islands of matter with grain sizes not greater than 20 nm (or the same islands on the surface of massive metal [10] and nonconducting films [11]). In this case atomization occurs in accordance with the isolated grain model [5].

2. The analytic expression correctly represents the value of  $S$  and indicates the strong influence of the grain size and relates  $S_{cal}$  to  $(dE/dx)_e$  for heavy multiply charged ions. Further refinement of the expression for  $S_{cal}$  will require more-careful experimental estimation of the grain size distribution and the mass of the atomized matter.

3. The coefficients of atomization, for heated films with islands of gold with diameter  $\sim 0.1 \mu\text{m}$  and thickness  $0.09 \mu\text{m}$ , for annealed continuous films with thicknesses  $\sim 1 \mu\text{m}$  and for annealed metallurgical foils are approximately the same and equal 10-30 atoms/fragment. To obtain a more-accurate value of  $S$  for bulk metals and to estimate the effect of their thickness, it is necessary to increase the accuracy of the measurements, to guarantee the absence of grains with diameters less than 30-50 nm on the surface of the metal, as well as to include the effect of the dose, exceeding  $5 \cdot 10^{12}$  fragments/cm<sup>2</sup>, especially when beams of heavy multiply charged ions are used.

We are grateful to V. P. Éismont and A. S. Krivokhatskii for discussing the results of the experiments, to B. G. Yarullof and G. V. Solov'ev for help in irradiating the specimens, to B. M. Aleksandrov for preparing the <sup>252</sup>Cf sources, and to G. A. Tutin, A. G. Donichkin, and A. N. Smirnov for help in performing the  $\gamma$ -spectrometric measurements.

#### LITERATURE CITED

1. I. A. Baranov and V. V. Obnorski, Problems in Nuclear Science and Technology, Series on the Physics of Radiation Damage [in Russian] (1981) No. 5(19), p. 37.
2. I. A. Baranov, A. S. Krivokhatskii, and V. V. Obnorski, Zh. Tekh. Fiz., 51, No. 12, 2457 (1981).
3. B. M. Aleksandrov et al., At. Energ., 38, No. 1, 47 (1975).
4. A. Goland and A. Paskin, J. Appl. Phys., 35, No. 7, 2188 (1964).

5. I. A. Baranov and V. V. Obnorskii, "Atomization of targets in beams of heavy multiply charged ions," Preprint RI-120, Leningrad (1980).
6. V. V. Obnorskii et al., *At. Energ.*, **53**, No. 2, 105 (1982).
7. P. Sigmund, *Phys. Rev.*, **184**, 383 (1969).
8. K. A. Petrzhak and M. A. Bak, *Zh. Tekh. Fiz.*, **25**, No. 4, 636 (1955).
9. L. Northcliffe and R. Schilling, *Nucl. Data Tables*, Vol. 7, No. 3, 4 (1970).
10. B. M. Aleksandrov et al., *At. Energ.*, **41**, No. 6, 417 (1976).
11. B. M. Aleksandrov et al., *At. Energ.*, **36**, No. 2, 139 (1974).

RADIATION TESTING AND THERMAL TESTING OF COMPTON-EMISSION  
NEUTRON DETECTORS HAVING A HAFNIUM-CONTAINING EMITTER

I. Ya. Emel'yanov, Yu. I. Volod'ko,  
O. K. Egorov, S. B. Zlokazov,  
V. V. Postnikov, Yu. A. Safin,  
and V. I. Uvarov

UDC 539.1.074.8

Compton-emission neutron detectors with a hafnium-containing emitter are one of the promising detector types for monitoring the neutron-flux distribution in the core zones of reactors. By contrast to the beta-emission neutron detectors with an emitter made from rhodium, silver, or vanadium [1-3] - detectors widely employed in power reactors - Compton-emission neutron detectors with a hafnium-containing emitter are practically free of inertia [4]. These detectors are therefore preferred in automatic systems for monitoring, controlling, and protecting reactors, where the detectors have to meet increased requirements in regard to fast response. Compton-emission neutron detectors are often produced with a technique employed in the manufacture of cables with magnesia insulation. The technique allows serial production of Compton-emission neutron detectors without important limitations for the length of the sensitive detector portion.

For the purpose of separately studying the influence which heat and radiation have upon the metrological properties and the electrical properties of Compton-emission neutron detectors and cables with magnesia insulation, we built an experimental setup which we inserted into a dry channel placed in the core of the experimental IVV-2M water-water reactor. When used with electric heating elements, the setup makes it possible to obtain various temperatures at a certain radiation intensity level, i.e., the temperature of the Compton-emission neutron detector can be varied within known limits without depending upon the irradiation intensity. Earlier a similar setup had been used to study the properties of beta-emission neutron detectors with a silver emitter and a cable with magnesia insulation [5]. In our experiment, the average flux density of the thermal neutrons reached  $1.7 \cdot 10^{14}$  neutrons/(cm<sup>2</sup> · sec) on the sample surface, the average flux density of the fast neutrons ( $E \geq 1.15$  MeV) was  $3.8 \cdot 10^{13}$  neutrons/(cm<sup>2</sup> · sec), and the average dose rate of the  $\gamma$ -radiation was  $2.8 \cdot 10^3$  Gy/sec.

Four samples of the cable-type Compton-emission neutron detector with a hafnium-containing emitter were tested. The design of the Compton-emission neutron detector is similar to that of the previously tested beta-emission neutron detector with a silver emitter [5]; the Compton-emission detector has an outer diameter of 3.0 mm. The insulation of the Compton-emission neutron detector is made of magnesium-oxide powder of the "analytically pure" quality according to All-Union State Standard 4526-75. The test samples of the Compton-emission neutron detector were annealed for 7 h at 750-800°C before the tests.

Both the current (short-circuit current) and the emf of the Compton-emission neutron detectors were determined at various irradiation-intensity levels and temperatures. The current of the Compton-emission neutron detector was measured with an F 116/2 microvolt-microammeter. The emf (in the range 0.03-20 V) was determined either with an electrostatic S-50 voltmeter or by applying an adjustable dc voltage between the emitter of the Compton-emission neutron detector and the input of a current meter; the voltage corresponding

---

Translated from *Atomnaya Energiya*, Vol. 54, No. 3, pp. 189-192, March, 1983. Original article submitted April 21, 1982.

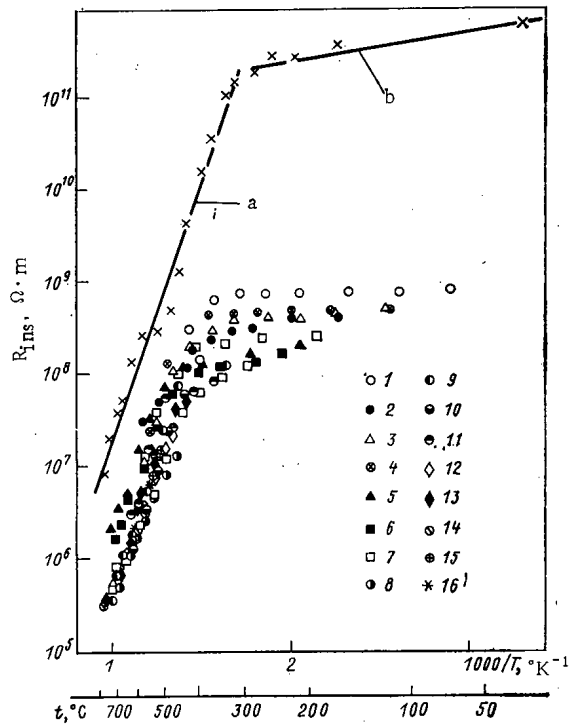


Fig. 1. Temperature dependence (outside the reactor and at various irradiation intensities in the reactor) of the insulation resistance of a Compton-emission neutron detector (a, b) correspond to Eqs. (3) and (5), respectively;  $\times$  refers to measurements outside the reactor). The points correspond to various  $\phi_T$  values (neutrons/cm<sup>2</sup>·sec; first value indicated) and  $R_\gamma$  values (Gy/sec; second value indicated): 1)  $8.5 \cdot 10^{12}$ ,  $1.4 \cdot 10^2$ ; 2)  $1.1 \cdot 10^{13}$ ,  $1.9 \cdot 10^2$ ; 3)  $1.4 \cdot 10^{13}$ ,  $2.2 \cdot 10^2$ ; 4)  $1.7 \cdot 10^{13}$ ,  $2.8 \cdot 10^2$ ; 5)  $1.8 \cdot 10^{13}$ ,  $3.0 \cdot 10^2$ ; 6)  $2.3 \cdot 10^{13}$ ,  $3.8 \cdot 10^2$ ; 7)  $3.4 \cdot 10^{13}$ ,  $5.6 \cdot 10^2$ ; 8)  $4.6 \cdot 10^{13}$ ,  $7.5 \cdot 10^2$ ; 9)  $5.1 \cdot 10^{13}$ ,  $8.4 \cdot 10^2$ ; 10)  $5.7 \cdot 10^{13}$ ,  $9.4 \cdot 10^2$ ; 11)  $6.8 \cdot 10^{13}$ ,  $1.1 \cdot 10^3$ ; 12)  $8.5 \cdot 10^{13}$ ,  $1.4 \cdot 10^3$ ; 13)  $1.0 \cdot 10^{14}$ ,  $1.7 \cdot 10^3$ ; 14)  $1.2 \cdot 10^{14}$ ,  $2.0 \cdot 10^3$ ; 15)  $1.4 \cdot 10^{14}$ ,  $2.2 \cdot 10^3$ ; 16)  $1.7 \cdot 10^{14}$ ,  $2.8 \cdot 10^3$ .

to current zero was numerically equal to the emf determined with a VK 7-9 voltmeter. The insulation resistance was calculated from both the current and the emf of the Compton-emission neutron detector. The temperature of the Compton-emission neutron detector was measured with a Chromel-Alumel thermoelectric thermometer. The junction of the thermoelectric thermometer was soldered directly to the collector of the Compton-emission neutron detector. The temperature gradient between the emitter and the collector did not exceed 1°C, owing to the high thermal conductivity of the densely pressed magnesium oxide (there were no gas-filled gaps in the insulation). The stationary temperature values were measured during 1-2 h. In individual cases the constance of the current of the Compton-emission neutron detector was checked for 15-20 h at a constant temperature and a constant irradiation intensity.

Experimental data on the resistance of the insulation of the Compton-emission neutron detector (Fig. 1)\* were evaluated in accordance with the theoretical temperature dependence and irradiation-intensity dependence of the electric conductivity of mineral insulation [6]. The dependence was based on the assumption that the electric conductivity  $\sigma$  of the insulation is composed of the thermal component  $\sigma_t$  and the radiation-thermal component  $\sigma_r$ , i.e., the insulation resistance at a given temperature and irradiation intensity can be expressed as follows:

$$R_{ins} = (1/R_r + 1/R_t)^{-1}, \quad (1)$$

\* Data averaged over four samples of Compton-emission neutron detectors are shown in Fig. 1 and referred to below.

where  $R_t$  is the insulation resistance at a given temperature outside the reactor.

It follows from Fig. 1 that, as in the case of a beta-emission neutron detector with a silver emitter, the radiation-thermal component of the electric conductivity of the insulation is much greater than the thermal electric conductivity of a Compton-emission neutron detector, and that  $R_r$  depends basically upon the total insulation resistance. The insulation resistance  $R_t$  outside the reactor in a Compton-emission neutron detector with a hafnium-containing emitter is much greater than in a beta-emission neutron detector with a silver emitter. The total insulation resistance  $R_{ins}$  of a Compton-emission neutron detector inside the reactor is also 1-2 orders of magnitude greater than that of a beta-emission neutron detector. This seems to be associated with the reduced (several times reduced) number of electrons leaving the emitter of the Compton-emission neutron detector at the same particular neutron-flux density.

We obtained empirical temperature dependencies of  $R_r$  and  $R_t$  for a Compton-emission neutron detector with a hafnium-containing emitter:

at temperatures in excess of 330°C

$$R_r = 7.9 \cdot 10^6 T^{-3/2} \varphi_T^{-0.043} \exp(9.4 \cdot 10^3/T), \quad (2)$$

$$R_t = 54 \exp(1.3 \cdot 10^4/T); \quad (3)$$

at temperatures up to 330°C

$$R_r = 1.3 \cdot 10^{14} P_\gamma^{-0.63} T^{-3/2}, \quad (4)$$

$$R_t = 4.8 \cdot 10^{10} \exp(8.1 \cdot 10^2/T). \quad (5)$$

The notation is interpreted as follows:  $T$  is the absolute temperature, deg K;  $\varphi_T$ , thermal-neutron flux density, neutrons/(cm<sup>2</sup> · sec); and  $P_\gamma$ , dose rate, Gy/sec, of the  $\gamma$  radiation;  $R_r$  and  $R_t$ , are referred to a detector length of 1 m and expressed in  $\Omega \cdot m$ .

Figure 1 shows that in the temperature range 330-770°C, the layering of points referring to different irradiation-intensity levels is less pronounced than in the range 70-330°C. The data were separately evaluated for the two temperature intervals. The exponent at the irradiation intensities in Eqs. (2) and (4) assumes very dissimilar values. In the interval 330-770°C, the parameter is close to zero, i.e., the dependence of  $R_r$  upon the irradiation intensity is only weakly pronounced, as in the case of beta-emission neutron detectors with a silver emitter. In the range 70-330°C this exponent is 0.63 and close to its value in the cable with magnesia insulation. We can assume that in the case of the cable,  $R_r$  is basically given by the dose rate of the  $\gamma$ -radiation, which in Eq. (4) was assumed as the measure of the irradiation intensity. Thus, as far as this aspect is concerned, a Compton-emission neutron detector with a hafnium-containing emitter occupies an intermediate position between a beta-emission neutron detector with a silver emitter and a cable.

The confidence limits in the calculation of the insulation resistance of the Compton-emission neutron detector with Eq. (1) and Eqs. (2)-(5) at the confidence level 0.98 correspond to  $R_{ins}$  changes by a factor of 6 toward greater or smaller values. Equation (2) is applicable at thermal-neutron flux densities ranging from  $8 \cdot 10^{12}$  to  $1.7 \cdot 10^{14}$  neutrons/(cm<sup>2</sup> · sec), fast-neutron ( $E \geq 1.15$  MeV) flux densities ranging from  $2 \cdot 10^{12}$  to  $3.8 \cdot 10^{13}$  neutrons/(cm<sup>2</sup> · sec), and  $\gamma$  dose rates ranging from  $1.2 \cdot 10^2$  to  $2.8 \cdot 10^3$  Gy/sec; Eq. (4) is applicable at thermal-neutron flux densities ranging from  $8 \cdot 10^{12}$  to  $5 \cdot 10^{13}$  neutrons/(cm<sup>2</sup> · sec), fast-neutron flux densities ranging from  $2 \cdot 10^{12}$  to  $1.5 \cdot 10^{13}$  neutrons/(cm<sup>2</sup> · sec), and  $\gamma$  dose rates ranging from  $1.2 \cdot 10^2$  to  $9 \cdot 10^2$  Gy/sec.

The sensitivity of the Compton-emission neutron detector is defined as the ratio of the detector current to the unit neutron flux density per unit detector length and depends upon both the temperature and the neutron-flux density to a lesser extent than does the sensitivity of beta-emission neutron detector with a silver emitter. The dependences of the sensitivity of the Compton-emission neutron detector upon the neutron-flux density is less pronounced than the sensitivity dependence on the temperature. The current of the Compton-emission neutron detector can increase with increasing temperature at a certain flux, because the rate of the nuclear reaction of neutron absorption in hafnium is increased by Doppler broadening of a neutron resonances [7]. But in the interval 70-770°C, this broadening in hafnium enhances the neutron absorption only by a few percent. This is certainly inadequate for explaining the observed change in the current of the Compton-emission neutron detector.

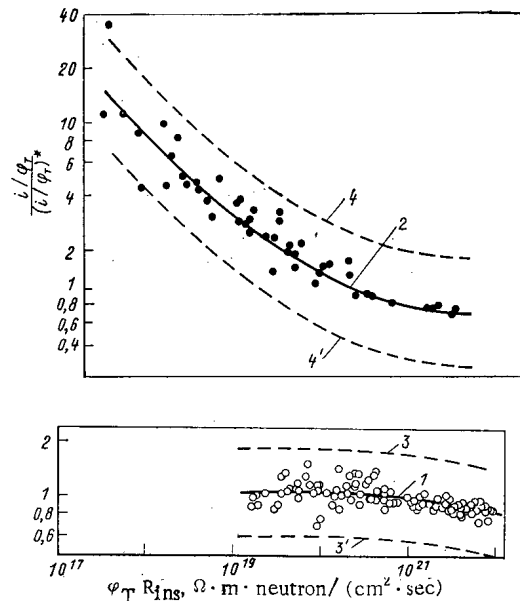


Fig. 2. Dependence of the sensitivity of the Compton-emission neutron detector upon  $\varphi_{TRins}$  for detectors with (○) a hafnium-containing emitter and (●) a silver emitter: 1) corresponds to Eq. (6); 2) corresponds to the analogous formula for the beta-emission neutron detector with a silver emitter [5]; 3, 3' and 4, 4' indicate the limits for the 0.98 confidence level.

An analysis of the experimental data has shown that, as in the case of a beta-emission neutron detector with a silver emitter [5], the resulting dependence of the sensitivity of the Compton-emission neutron detector upon the temperature and the neutron flux should be interpreted with the product  $\varphi_{TRins}$  — the flux density of thermal neutrons times the insulation resistance of the Compton-emission neutron detector; the product is proportional to the electric potential of the barrier in the insulation of the Compton-emission neutron detector [5]. It was established that with a constant product  $\varphi_{TRins}$ , the sensitivity of the Compton-emission neutron detector depends only slightly upon the temperature and the neutron-flux density.

In general terms, the dependence of the sensitivity of the Compton-emission neutron detector upon the height of the potential barrier can be explained as in the case of the beta-emission neutron detector with a silver emitter [5]. The sensitivity of the Compton-emission neutron detector can be modified by changes in the electric potential distribution in the dielectric in dependence upon the irradiation intensity and the temperature, and by the influence which the changing distribution exerts upon the passage of electrons.

Figure 2 shows the experimentally obtained dependence of the sensitivity of the Compton-emission-neutron detector upon the factor  $\varphi_{TRins}$ . We realize that for  $\varphi_{TRins} \geq 5 \cdot 10^{20} \Omega \cdot m \cdot \text{neutron}/(\text{cm}^2 \cdot \text{sec})$ , the spread of the experimental points is much smaller than at lower  $\varphi_{TRins}$  values. At significant  $\varphi_{TRins}$  values we can therefore obviously expect more-clearly pronounced changes in the sensitivity of the Compton-emission neutron detector in dependence upon the temperature and, accordingly, detector operation of greater stability. As far as the design of the Compton-emission neutron detector with a hafnium-containing emitter is concerned, in the case of a high-power reactor with a core height of 7 m and an average thermal-neutron flux density of about  $7 \cdot 10^{13}$  neutrons/ $(\text{cm}^2 \cdot \text{sec})$  in the core, a value  $\varphi_{TRins} = 5 \cdot 10^{20} \Omega \cdot m \cdot \text{neutrons}/(\text{cm}^2 \cdot \text{sec})$  corresponds to an insulation resistance of the Compton-emission neutron detector of the order of  $1 \cdot 10^6 \Omega$  at the nominal power rate of the reactor, i.e., stable operation of the detector can be expected at greater  $R_{ins}$  values. But at  $\varphi_T = 7 \cdot 10^{13}$  neutrons/ $(\text{cm}^2 \cdot \text{sec})$  we obtain  $R_{ins} = 1 \cdot 10^6 \Omega$  at 550–600°C for the Compton-emission neutron detector (see Fig. 1), which means that the highest operational temperature of the Compton-emission neutron detector is not below this value.

By evaluating the results of the measurements shown in Fig. 2 with the least-squares method, the following empirical dependence of the sensitivity of the Compton-emission neutron detector upon the factor  $\varphi_{TR_{ins}}$  was obtained:

$$\frac{i/\varphi_T}{(i/\varphi_T)^*} = 9.6 \cdot 10^{-10} \exp \{2.1 \lg(\varphi_T R_{ins}) - 0.053 [\lg(\varphi_T R_{ins})]^2\}, \quad (6)$$

where  $i$  is the detector current, A/m, referred to a 1-m detector length;  $\varphi_T$ , average flux density of the thermal neutrons, neutrons/(cm<sup>2</sup>·sec), over the length of the sensitive portion of the detector;  $R_{ins}$ , resistance,  $\Omega \cdot m$ , of the detector insulation referred to 1 m of detector length; and  $(i/\varphi_T)^*$ , detector sensitivity at  $\varphi_{TR_{ins}} = 5 \cdot 10^{20} \Omega \cdot m \cdot \text{neutrons}/(\text{cm}^2 \cdot \text{sec})$ . The limits (in regard to irradiation intensity) within which Eq. (6) can be employed coincide with the corresponding limits for Eq. (2). Equation (6) can be used at temperatures of 70-770°C. The confidence limits for calculating the sensitivity of a Compton-emission neutron detector with Eq. (6) and formulas (1)-(5) at the confidence level 0.98 correspond to sensitivity changes by a factor of 1.8 toward larger or smaller values (see Fig. 2). The errors of determining the sensitivity of the Compton-emission neutron detector are much smaller than the spread of the experimental points shown in Fig. 2.

Figure 2 shows for comparison the above-described dependence of the detector sensitivity upon the factor  $\varphi_{TR_{ins}}$  for a Compton-emission neutron detector with a hafnium-containing emitter; also shown is the corresponding dependence for a beta-emission neutron detector with a silver emitter. Obviously, in the first case the dependence is much less pronounced than in the second case. The rapid increase in the current of the beta-emission neutron detector with a silver emitter at increasing temperature limits the highest operational temperature of the beta-emission neutron detector to 400-450°C, i.e., the temperature is lower by about 150°C than that of the Compton-emission neutron detector with a hafnium emitter. In practice, both the Compton-emission neutron detector with the hafnium-containing emitter and the beta-emission neutron detector with the silver emitter are usually employed under conditions corresponding to the right side of curves 1 and 3 of Fig. 2, i.e., at values  $\varphi_{TR_{ins}} \geq 5 \cdot 10^{20} \Omega \cdot m \cdot \text{neutron}/(\text{cm}^2 \cdot \text{sec})$ . In this range the dependence of both Compton-emission and beta-emission neutron detectors upon  $\varphi_{TR_{ins}}$  is relatively stable and not very pronounced. For  $\varphi_{TR_{ins}} \geq 5 \cdot 10^{20} \Omega \cdot m \cdot \text{neutron}/(\text{cm}^2 \cdot \text{sec})$ , i.e., in the range of Compton-emission neutron detector operation in regard to temperature and radiation intensity, a temperature increase from 70 to 550-600°C at unchanged irradiation intensity leads to an increase in the sensitivity of the Compton-emission neutron detector by at most 13-18%. A similar increase in the sensitivity of the beta-emission neutron detector with the silver emitter corresponds to a temperature change of only 50-100°C.

The results obtained in our work confirm that the electric fields in the insulation of the emission detectors are important for the current conversion process in the detector.

#### LITERATURE CITED

1. M. G. Mitel'man et al., Detectors for Measurements of Energy Liberation Inside Reactors [in Russian], Atomizdat, Moscow (1977).
2. I. Ya. Emel'yanov et al., At. Energ., 48, No. 6, 368 (1980).
3. J. Boland, Instruments (in the Core) for Monitoring Nuclear Reactors [Russian translation], Atomizdat, Moscow (1973), p. 160.
4. H. Böck et al., Nucl. Instrum. Methods, 123, No. 1, 117 (1975).
5. I. Ya. Emel'yanov et al., At. Energ., 37, No. 1, 72 (1974).
6. I. Ya. Emel'yanov et al., At. Energ., 50, No. 1, 21 (1981).
7. A. M. Weinberg and E. P. Wigner, Physics Theory of Neutron Chain Reactors, Univ. Chicago Press (1958).

LOCAL RADIATION ACTION OF ATMOSPHERIC EMISSIONS  
ASSOCIATED WITH THE OPERATION  
OF A RADIOCHEMICAL PLANT

I. N. Ruzhentsova and E. N. Teverovskii

UDC 004.86

It has been proposed in many countries to make the transition to a closed nuclear fuel cycle with the regeneration of spent fuel at radiochemical plants (RCP). In this connection the possible radiation action on the population both on the local and on the global scales resulting from the operation of RCP is of interest. The global effects of radioactive contamination of the biosphere by atmospheric emissions from RCP has been discussed in detail in [1]. Estimates are made in this paper of the local irradiation dosages of the population.

The radiation environment associated with the operation of RCP is determined by the internal irradiation upon the oral entry of radionuclides with the consumable food products and the inhalational entry of radionuclides into the human organism, as well as by external irradiation due to the emission stream and radioactive aerosols precipitated on the surface of the earth. The emission capacity and the composition of the radionuclides eliminated through the ventilation duct of an RCP depend on the kind of fuel, the duration of irradiation (the operating period of the reactor), and the holding time of the fuel prior to regeneration, as well as on the reprocessing technology and the efficiency of the gas-purifying equipment used.

Let us consider a hypothetical RCP with a capacity of 1500 tons/yr. This value is characteristic both for the published designs of plants for fuel reprocessing and for hypothetical RCP presented in the scientific-technical literature [1].

The calculated values of the capacity for emission into the atmosphere of the principal radionuclides during the operation of a hypothetical RCP in Bq/MW (elec.) · yr are given below:

Tritium	2.2 · 10 <sup>9</sup> –7.4 · 10 <sup>11</sup>
<sup>14</sup> C	3.7 · 10 <sup>8</sup>
<sup>85</sup> Kr	1.2 · 10 <sup>13</sup>
<sup>129</sup> I	4.1 · 10 <sup>5</sup> –1.2 · 10 <sup>7</sup>
<sup>90</sup> Sr	2.2 · 10 <sup>6</sup>
<sup>106</sup> Ru	1.6 · 10 <sup>6</sup>
<sup>134</sup> Cs	2.4 · 10 <sup>6</sup>
<sup>137</sup> Cs	3.1 · 10 <sup>6</sup>
<sup>144</sup> Ce	1.7 · 10 <sup>6</sup>
<sup>238</sup> Pu	5.6 · 10 <sup>5</sup>
<sup>239</sup> Pu	6.7 · 10 <sup>4</sup>

The following assumptions were made in the calculation:

1. The enrichment of the fuel of a typical light-water reactor is 3%, and the depletion depth is 30 MW · days/kg [1].
2. The holding time of the fuel prior to regeneration is 3 yrs [2, 3].
3. Two values of the relative yield are considered for tritium;  $q = A_Q/A_M$ , where  $A_Q$  is the activity of the radionuclide emitted into the atmosphere and  $A_M$  is the activity of the same nuclide in the fuel mass which has proceeded to reprocessing.
  - a)  $q(^3\text{H}) = 3 \cdot 10^{-3}$  [4, 5]. Most of the tritium goes into the environment with the liquid waste.
  - b)  $q(^3\text{H}) = 1$ , i.e., all the tritium contained in the depleted fuel enters the atmosphere during regeneration [1, 4].
4. The entire amount of <sup>14</sup>C and <sup>85</sup>Kr contained in the depleted fuel is emitted into the atmosphere during regeneration [1, 4].

Translated from *Atomnaya Énergiya*, Vol. 54, No. 3, pp. 192-194, March, 1983. Original article submitted June 14, 1982.

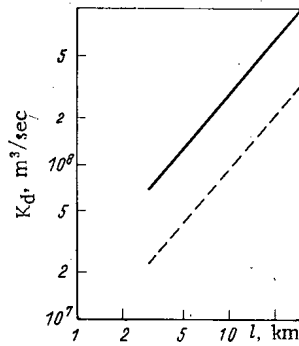


Fig. 1. Dependence of the mean annual dilution coefficient  $K$  of a weightless and highly dispersed impurity on the direction  $l$  to the ventilation duct for RCP regions having different peculiarities of the wind regimes with  $P/P_0 = 1$  (—) and 3 (----).

TABLE 1. Variation of the Internal Irradiation Dosage at the Point of Maximum Near-Surface Concentration for Different Locations of the RCP

Radionuclide	$D_{max}$ , sievert*/MW (elec.)·yr	Critical organ	$D_{max}$ , sievert/MW (elec.)·yr (inhalational entry)	Critical organ
Tritium	a) $1,2 \cdot 10^{-12} - 3,6 \cdot 10^{-12}$ b) $3,8 \cdot 10^{-10} - 1,4 \cdot 10^{-9}$	Whole body Fatty tissue	$4,2 \cdot 10^{-13} - 1,3 \cdot 10^{-12}$ $1,4 \cdot 10^{-10} - 4,2 \cdot 10^{-10}$	Whole body Fatty tissue
$^{14}C$ $^{129}I$	$2,4 \cdot 10^{-11} - 7,2 \cdot 10^{-11}$	Thyroid gland	$5,7 \cdot 10^{-13} - 1,7 \cdot 10^{-12}$	Thyroid gland
$^{90}Sr$	a) $1,0 \cdot 10^{-10} - 3,0 \cdot 10^{-10}$ b) $2,8 \cdot 10^{-9} - 8,4 \cdot 10^{-9}$	Bone	$1,4 \cdot 10^{-12} - 4,2 \cdot 10^{-12}$ $3,9 \cdot 10^{-11} - 1,2 \cdot 10^{-10}$	Bone
$^{106}Ru$	$1,1 \cdot 10^{-9} - 3,3 \cdot 10^{-9}$ $6,0 \cdot 10^{-12} - 1,8 \cdot 10^{-11}$	Gastrointestinal tract (lower large intestine)	$1,0 \cdot 10^{-11} - 3,0 \cdot 10^{-11}$ $5,8 \cdot 10^{-14} - 1,7 \cdot 10^{-13}$	Gastrointestinal tract (lower large intestine)
$^{134}Cs$	$5,8 \cdot 10^{-11} - 1,7 \cdot 10^{-10}$	Whole body	$5,7 \cdot 10^{-14} - 1,7 \cdot 10^{-13}$	Whole body
$^{137}Cs$	$8,0 \cdot 10^{-11} - 2,4 \cdot 10^{-10}$	Whole body	$4,3 \cdot 10^{-14} - 1,3 \cdot 10^{-13}$	Whole body
$^{144}Ce$	$3,6 \cdot 10^{-12} - 1,1 \cdot 10^{-11}$	Gastrointestinal tract (lower large intestine)	$7,0 \cdot 10^{-13} - 2,1 \cdot 10^{-12}$	Lungs
$^{238}Pu$	$2,0 \cdot 10^{-11} - 6,0 \cdot 10^{-11}$	Bone	$3,1 \cdot 10^{-9} - 9,3 \cdot 10^{-9}$	Bone
$^{232}Pu$	$2,2 \cdot 10^{-12} - 6,6 \cdot 10^{-12}$	Bone	$4,3 \cdot 10^{-10} - 1,3 \cdot 10^{-9}$	Bone

\* 1 sievert = 100 rem; 1 csievert = 1 rem.

5. Two limiting cases are discussed for  $^{129}I$ :

a) the system for collecting  $^{129}I$  at the RCP has an efficiency of 99% [1, 5]; in this case  $q(^{129}I) = 0.01$ .

b) there is no system for collecting the iodine, and 25% of the  $^{129}I$  is emitted into the atmosphere, i.e.,  $q(^{129}I) = 0.25$  [5], and the rest of the iodine enters the environment with the liquid waste.

It has been taken into consideration that practically all the  $^{129}I$  is emitted into the atmosphere in vapor form; the subsequent adsorption of the vapors on atmospheric condensation nuclei results in the fact that the iodine is scattered as a highly dispersed impurity in the near-surface layer of the atmosphere.

6. The emission capacity of  $^{90}Sr$ ,  $^{137}Cs$ ,  $^{106}Ru$ ,  $^{144}Ce$ , and  $^{134}Cs$  has been determined for  $q = 2.5 \cdot 10^{-8}$  [3].

7. The emission capacity of  $^{238}Pu$  and  $^{239}Pu$  has been calculated for  $q = 1.6 \cdot 10^{-7}$  [5]. We note that the emissions of aerosols depend mainly on the technological peculiarities of the fuel regeneration process at the RCP.

The irradiation dosage caused by the emission of the  $i$ -th radionuclide is proportional to the ratio  $Q_i K_{D_i} / K_d$  ( $Q_i$  is the capacity for emission of the radionuclide;  $K_d$ , mean annual dilution coefficient of the impurity in the near-surface layer of the atmosphere; and  $K_{D_i}$ , transition coefficient from the near-surface concentration of the radionuclide to the irradiation dosage).

TABLE 2. Variation of the External Irradiation Dosage at the Point of Maximum Near-Surface Concentration for Different Locations of the RCP

Radionuclide	$D_{max}$ , sievert/MW (elec.)·yr (irradiation due to the surface of the earth)	Critical organ	$D_{max}$ , sievert/MW (elec.)·yr (irradiation due to the emission stream)	Critical organ
$^{85}Kr$	—	—	$1,5 \cdot 10^{-9} - 4,5 \cdot 10^{-9}$	Skin
$^{106}Ru$	$6,0 \cdot 10^{-14} - 1,8 \cdot 10^{-13}$	Whole body	$1,4 \cdot 10^{-16} - 4,2 \cdot 10^{-16}$	Whole body
$^{134}Cs$	$8,5 \cdot 10^{-13} - 2,6 \cdot 10^{-12}$	Same	$1,7 \cdot 10^{-15} - 5,1 \cdot 10^{-15}$	Same
$^{137}Cs$	$8,7 \cdot 10^{-13} - 2,6 \cdot 10^{-12}$	» »	$7,6 \cdot 10^{-16} - 2,3 \cdot 10^{-15}$	» »
$^{144}Cs$	$7,1 \cdot 10^{-15} - 2,1 \cdot 10^{-14}$	» »	$1,5 \cdot 10^{-17} - 4,5 \cdot 10^{-17}$	» »

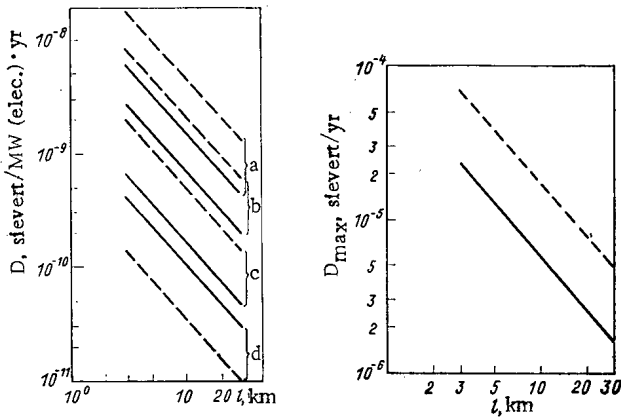


Fig. 2. Irradiation dosages of organs and tissues at various distances from an emission source: ---)  $P/P_0 = 3$ ; —)  $P/P_0 = 1$ ; a) group III of critical organs; b) group II for  $q(^{129}I) = 0.25$ ; c) group I for  $q(^3H) = 1$ ; d) group I for  $q(^3H) = 3 \cdot 10^{-3}$  (—) with  $P/P_0 = 3$ , and group II for  $q(^{129}I) = 0.01$  (---) with  $P/P_0 = 1$ .

Fig. 3. Variation of the maximum total effective dosage  $D_{max}$  in various locations of an RCP as a function of distance with  $P/P_0 = 3$  (---) and  $P/P_0 = 1$  (—).

The mean annual dilution coefficient depends on the elongation index of the mean annual rose of the winds at the RCP location  $P/P_0$ , where  $P$  is the actual repeatability of the predominant wind direction and  $P_0 = 0.125$  is the repeatability of each direction of the eight-bearing circular rose of the winds. The transition to actual repeatability of the predominant wind direction from a circular rose of winds is accomplished with the help of the relationship

$$K_d = K_{d0} (P/P_0)^{-1}, \tag{1}$$

where  $K_{d0}$  and  $K_d$  are the mean annual dilution coefficients for the circular and actual roses of the winds;  $P/P_0 = 2$  for a 2:1 wind rose, and  $P/P_0 = 3$  for a 3:1 wind rose.

The range of variation of the experimental values of the mean annual dilution coefficient of a weightless and highly dispersed impurity for RCP locations having different peculiarities of the wind regime [4] are shown in Fig. 1 for an effective height of the source of 200 m, which is adopted in [1].

The limits of variation of the irradiation dosage of the population at the point of maximum near-surface concentration are given in Tables 1, 2 for different locations of the RCP. An average food ration was assumed when estimating the dosage values; the contributions of the principal nutrition products produced at the plant

locations to the annual consumption are as follows: 80% (milk, vegetables, meat) and 100% (potatoes) [6]. The sources of the drinking water supply are artesian wells. The coefficients  $KD_i$  are taken from [6-8].

The values of the irradiation dosage of separate groups of critical organs [7] at various distances from the ventilation duct of an RCP are presented in Fig. 2. The variation of the maximum total effective dosage as a function of distance from an RCP is shown in Fig. 3 for different locations of it. We note that the main factor of the radiation action of the emissions of an RCP is the oral entry of radionuclides into the human organism. The external irradiation produced by the emission of  $^{85}\text{Kr}$  exerts a smaller effect. The dosage of external irradiation due to radionuclides precipitated on the surface of the earth and the irradiation dosage associated with inhalational entry are smaller by two orders of magnitude than the internal irradiation dosage due to oral entry. The effect of an emission stream of radioactive aerosols on the formation of the irradiation dosage level is insignificant. As far as contributions to the total effective irradiation dosage of the population in the regions in which plants are located is concerned, the radionuclides are distributed in the following order: for  $q(^3\text{H}) = 3 \cdot 10^{-3}$  and  $q(^{129}\text{I}) = 0.01$   $^{137}\text{Cs}$  -  $^{134}\text{Cs}$ ,  $^{85}\text{Kr}$ ,  $^{14}\text{C}$ ,  $^{90}\text{Sr}$ ,  $^{238}\text{Pu}$ ,  $^{129}\text{I}$ ,  $^{239}\text{Pu}$ ,  $^{106}\text{Ru}$ ,  $^{144}\text{Ce}$ , and  $^3\text{H}$ ; for  $q(^3\text{H}) = 1$  and  $q(^{129}\text{I}) = 0.25$   $^3\text{H}$  -  $^{129}\text{I}$ ,  $^{137}\text{Cs}$ ,  $^{134}\text{Cs}$ ,  $^{85}\text{Kr}$ ,  $^{14}\text{C}$ ,  $^{90}\text{Sr}$ ,  $^{238}\text{Pu}$ ,  $^{239}\text{Pu}$ ,  $^{106}\text{Ru}$ , and  $^{144}\text{Ce}$ .

As is evident from Fig. 3, the upper limit to the total effective dosage at the point of maximum near-surface concentration does not exceed  $7.0 \cdot 10^{-5}$  sievert/yr. At the same time, the dosage produced by the natural radiation background amounts to  $\sim 1 \cdot 10^{-3}$  sievert/yr [1]. Thus, the maximum total effective dosage at the locations of RCP amounts to about 10% of the dosage produced by the natural radiation background.

According to the data of [1], the individual effective dosage at the point of maximum near-surface concentration is  $3.5 \cdot 10^{-7}$  sievert/yr and  $4.2 \cdot 10^{-6}$  sievert/yr for nuclear power plants with water-cooled-water-modulated power reactors and with high-powered water-cooled channel reactors, respectively. Consequently, the radiation action of an RCP on the population living in the vicinity of its location is 16-200 times higher than the radiation action of nuclear power plants with different types of reactors. The total effective irradiation dosage of the population in the vicinity of an RCP is 70 times less than the dosage limit for personnel of category B established by NRB-76 [7].

If one assumes, as has been done in [1], that the average population density at plant sites is equal to 25 persons/ $\text{km}^2$ , then the upper limit of the collective irradiation dosage of the population in a radius out to 100 km, which can serve as one of the characteristics of radiation action, will not exceed 2 man-sievert/yr.

#### LITERATURE CITED

1. N. S. Babaev et al., Nuclear Power, Man, and the Environment [in Russian], Énergoizdat, Moscow (1981).
2. V. V. Fomin et al., At. Energ., 43, No. 6, 481 (1977).
3. "Sources and the action of ionizing radiation," Lectures of the United Nations Scientific Committee on the Action of Nuclear Radiation, New York (1978).
4. N. E. Artemova et al., At. Energ., 51, No. 2, 112 (1981).
5. "Radioactive contamination associated with the production of nuclear energy," Lectures of the United Nations Scientific Committee on the Action of Nuclear Radiation, New York (1980), UN, A/AC. 82/374.
6. N. E. Artemova et al., Permissible Emissions of Radioactive and Harmful Chemical Materials into the Near-Surface Layer of the Atmosphere [in Russian], Atomizdat, Moscow (1980).
7. Norms of Radiation Safety NRB-76 and the Basic Sanitation Rules OSP-72/80, Énergoizdat, Moscow (1981).
8. Meteorology and Atomic Energy [in Russian], Gidrometeoizdat, Leningrad (1971).

ALLOWANCE FOR ECONOMIC DISCOUNTING IN ESTIMATION OF THE HARM  
 DONE BY RADIOACTIVE CONTAMINATION OF THE BIOSPHERE  
 BY NUCLEAR ENERGY FACILITIES

V. F. Demin, E. I. Ermakova,  
 and Ya. V. Shevelev

UDC 621.039.003

Both individual and collective radiation doses\* are estimated in order to determine the impact of radiation. An important place is occupied by the so-called expected collective doses

$$S^c = \int_0^{\infty} \dot{S}(t) dt, \quad (1)$$

where  $\dot{S}(t)$  is the collective dose rate at the time  $t$ , caused by some industrial process in the nuclear fuel cycle (NFC) at the time  $t = 0$ ;

At the present time the quantity  $S^t$  is used as a measure of the total irradiation of the population due to the source under consideration and serves as a basis for estimating the pertinent harm, expressed by one indicator or another. For convenience in making relative estimates, the literature usually gives the values of the collective doses, normalized to a unit of energy generated — usually 1 MW (elec.) · yr. Such values of  $S^t$  and  $\bar{S}$  are indicated below by  $\bar{S}^t$  and  $\bar{S}$ , respectively.

\* Henceforth, dose will be taken to mean the effective equivalent dose [4].

TABLE 1. Normalized Expected Values of the Irradiation Dose of the Personnel and Population at Various Stages of the NFC in a Light-Water Reactor,  $10^{-2}$  man-sievert/MW(elec.)·yr

NFC stage	$\bar{S}^t$	$\bar{S}$	$\bar{S}_a^t$ *
Ore extraction and processing: fuel fabrication			
personnel	0,2—0,3	0,2—0,3	0,2—0,3
population	~ 1000	0,3	≤ 0,01
Atomic power plant			
personnel	1	1	1
population			
local and regional dose	0,04—0,4	0,04—0,4	0,04—0,4
overall dose	3—7	0,6—1,7	~ 0,1
Spent-fuel processing			
personnel	1,0	1,0	1,0
population:			
local and regional dose	0,1—0,6	0,1—0,6	0,1—0,6
overall dose	70—85	2,1—3,9	~ 0,5
Radioactive waste handling, including burial			
personnel	0,01—0,2	0,01—0,2	0,01—0,2
population	25—110	~ 0	~ 0
Research and development			
personnel	0,5	0,5	0,5
<b>Total</b>			
personnel	~ 3	~ 3	~ 3
population	~ 1000	3,1—6,9	0,8—1,6

\*Data of present paper.

Translated from Atomnaya Énergiya, Vol. 54, No. 3, pp. 195—199, March, 1983. Original article submitted January 11, 1982.

Table 1 gives the values of  $\bar{S}^t$  for different stages in the nuclear fuel processing cycle, according to the data of [1-3]. The uncertainty in the estimates is due to the scatter of the data from different sources in the literature and the inaccuracy of the model calculations, as well as to the difference in the initial characteristics of the NFC (with and without spent-fuel reprocessing), etc. As follows from Table 1, the largest contribution to the total  $\bar{S}^t$  comes from: the initial stage of the NFC,\* mainly because of the uranium and its decay products entering into the environment with emissions (discharges) from facilities in this stage; reprocessing of spent fuel (as a result of the emission or discharge of globally significant radionuclides, mainly  $^{129}\text{I}$  and  $^{14}\text{C}$ ); burial of radioactive wastes. The principal characteristic of these contributions to  $\bar{S}^t$  is that they are formed because of radionuclides with a very long half-life and during many thousands of years at a very low collective dose rate  $\dot{S}$ . On the other hand, part of the contributions to  $\bar{S}^t$  comes from short-lived radionuclides. This is the dose received by the personnel and population on local and regional scales as the result of emissions (discharges) from atomic power plants and a radiochemical plant during the time that coincides with the time of the industrial process or is close to it.

In view of this, there is doubt as to the equivalence of the various components of  $\bar{S}^t$ , particularly those which are realized in very remote times (for more details see [1, 2]). As a palliative resolution of the doubts in [1] it was proposed to use the so-called incompletely expected dose  $\bar{S}_i^t$  for estimating the radiation impact of the NFC. It is also defined by Eq. (1), except that the upper limit of integration  $t = \infty$  is replaced by  $t_{\max} = 500 \text{ yr}$  (or  $10^4 \text{ yr}$ ).

It should be obvious that both the very procedure of truncating the range of integration and the limit  $t = 500 \text{ yr}$  are not justified.†

The authors of this paper investigated the possibility of another concept of the expected dose. The investigations were directed at looking for and substantiating such time-weighting factors which would make it possible to vary the value of the dose received by the population at different times relative to the time at which energy was generated. As a result of these investigations we can make the following conclusions:

1. Considering various aspects of the estimation of the harm done by radioactive contamination of the biosphere (economic, social, biomedical, etc.), we can introduce some of them, but it is difficult to substantiate them with sufficient rigor because of uncertainties in the long-range predictions.‡ An exception is the time factor explicable by the economic approach to estimation of the harm; this is the familiar discounting function from economics.

2. The discounted expected dose  $S_d^t$  defined below should become the basis for an estimate of the harm from radioactive contamination of the biosphere with NFC facilities, regardless of the indicators (economic or other) in terms of which this harm is expressed. It is important only that a corresponding economic factor could be associated with any of these noneconomic indicators.

#### DISCOUNTED EXPECTED COLLECTIVE DOSE

An economic approach to estimation of the harm inflicted upon the environment by one form of industry or another is necessary for a number of reasons. The principal reason is that the economic effect is the sole indicator which can be used to compare or sum up different forms of harm to the biosphere and the expenditures on a protection system. The use of the benefit-harm criterion in optimization of the system of environmental protection is based on this approach.

In economic assessment of the harm it is not at all a matter of indifference as to when, relative to the time of production, the damage occurs or the expenditures must be made. In the economic calculations, time is taken into account by introducing the aforementioned discounting function

$$\Phi(t) = e^{-Et}, \quad (2)$$

where the parameter  $E$  is the norm for reducing the expenditures to a unit time ( $\text{yr}^{-1}$ ). Its value is taken to be 0.08 [5]; time  $t$  is in yrs.

\* All of the facilities up to atomic power plants.

† The quantity  $\bar{S}_i^t$  was introduced for another purpose, viz., for estimating the maximum annual dose  $\dot{S}$  for the population at some future moment of time, caused by prolonged operation (for 500 yr) of an atomic power plant at a constant level [1].

‡ For example, a prediction associated with the development of methods for the treatment of certain cancers or genetic diseases or others.

Suppose that a unit of production is accompanied by an economic damage, whose "realization" is stretched considerably in time, and this "stretching" is described by the function  $\bar{Z}(t)$ , the annual damage at the time  $t$  measured from the moment of production. The bar above  $Z$  indicates that we are considering the loss per unit production. Then the contribution from the resulting damage to the reduced production cost is

$$\bar{Z} = \int_0^{\infty} \bar{Z}(t) e^{-Et} dt. \quad (3)$$

Equation (3) and the considerations above concerning the use of the discounting factor in estimating the damage to the biosphere, inflicted by one form of production or another, constitute the starting point for determining the discounted expected dose  $\bar{S}_d^t$ .

The harm  $Z$  to the health of the population and the collective dose  $S$  are related by

$$Z = AS \quad (4)$$

or, for their annual values,

$$\dot{Z} = A\dot{S}, \quad (5)$$

where  $A$  is the economic damage from a dose of 1 man-sievert.

When in Eq. (3) we substitute Eq. (5), written for the reduced quantities  $\bar{Z}(t)$  and  $\bar{S}(t)$ , for  $\bar{S}_d^t \equiv Z/A$  we get

$$\bar{S}_d^t = \int_0^{\infty} \bar{S}(t) e^{-Et} dt. \quad (6)$$

The transition from Eq. (3) to Eq. (6) was made with the assumption that  $A$  does not depend on time.

The value of  $\bar{S}_d^t$  found from Eq. (6) with allowance for the discounting function can be appropriately called the discounted expected dose or the economically significant measure of the expected dose, in contradistinction to the total expected dose [see Eq. (1)].

Table 1 gives the values of  $\bar{S}_d^t$  calculated from Eq. (6). The values of  $\bar{S}(t)$  were obtained with the dose-estimation models described in [1]. We point out that for the components of the expected dose which the discounting function does not affect,  $\bar{S}^t = \bar{S}_i^t = \bar{S}^t$ . These components include the personnel irradiation dose as well as the irradiation dose received by the population from relatively short-lived radionuclides.

## DISCUSSION AND CONCLUSIONS

With the economic approach to the estimation of the harm done to the biosphere by radioactive contaminations, it is necessary to take discounting into account when summing the collective dose from different times. In this case the estimation of the harm is based not on the total  $\bar{S}^t$ , but on the discounted expected dose  $\bar{S}_d^t$ .

The latter is an intermediate quantity in the calculation of the economic harm from radioactive contamination of the biosphere (relative to  $\bar{Z}$ ). The introduction of a new quantity in addition to  $Z$  is appropriate because Eq. (6) does not contain the quantity  $A$ , whose value has not been established reliably as yet. Several papers have been published to date about estimating  $A$  (e.g., [6-8]) as a quantity characterizing the economic harm due to the loss of health or premature death. Thus far, however, there are substantial divergences both in the approaches to the determination of  $A$  and in the estimation of its individual components.

In obtaining Eq. (6) we assumed that  $A$  does not depend on time. Generally speaking, this is not so. The parameter  $E$  may also vary with time. In this case the time factor  $e^{-Et}$  in (6) should be replaced by

$$\exp\left(-\int_0^t E(\tau) d\tau\right) f_A(t). \quad (7)$$

Here the first term is a time-dependent discounting factor for  $E$ , and  $f_A(t)$  is a function that allows for the time variation of  $A$ . Without going into details in discussing this problem, we note the following:

1. The rate and direction of the time variation of  $A$  (if no allowance is made for inflation) have also not been adequately established, just like the quantity  $A$  itself, but in this case  $f_A(t)$  is a function that varies much more slowly than does the discounting function and, therefore, is less significant.

2. If it is assumed that under the conditions of some country the quantity  $A$  is subject to the effects of inflation ( $A = A_0 e^{\gamma t}$ , where  $\gamma$  is the inflation rate,  $\text{yr}^{-1}$ ), then  $\Delta E = \gamma$  must be added to  $E$ . As a result, in Eq. (6) the two auxiliary exponents (of  $E$  and  $\gamma$ ) cancel each other out and the formula for  $\bar{S}_d^t$  remains the same.\*

3. Determining  $E(t)$  is a problem of long-range forecasting, which is not considered here. It is unquestionable, however, that the character of  $E(t)$  in the distant future cannot significantly affect the values of  $\bar{S}_d^t$ , referred to the present time or the nearest future.

An explanation must be given as to the choice of  $E$ . Generally speaking,  $E$  can be different for different countries and different social systems and may change as the social system develops. Moreover, even within the framework of a single country there may be differences as to the standardized value of  $E$ . This hinders the choice of  $E$  for concrete economic calculations. In calculation of  $\bar{S}_d^t$  for the NFC, however, the uncertainties indicated above are not of fundamental importance. From Table I we see that when the integral is truncated to the times in (1) by  $t_{\text{max}}^{500} = 500 \text{ yr}$ , the most significant components of the total expected dose  $\bar{S}^t$  [resulting from the effect of radionuclides with a very long half-life  $T_{1/2}$  ( $\text{U}$ ,  $^{129}\text{I}$ , etc.) or with a very long time for emergence from a deep geological burial vault  $T_{\text{emer}}$  ( $T_{1/2} \gg t_{\text{max}}^{500}$ )] become zero. In this case the value of the truncated  $\bar{S}^t$  decreases by two or three orders of magnitude and terms that do not depend on the truncation limit begin to play an important role.

The time of economic truncation  $\tau_{\text{ec}} = 1/E$  in any case is smaller than  $t_{\text{max}}^{500}$  (in actual fact, much smaller). Therefore,  $\bar{S}_d^t$  also does not contain large terms. In this case the inaccuracies in the remaining,  $E$ -dependent contributions in  $\bar{S}_d^t$ , owing to the likely inaccuracy of  $E$ , are not very significant against the background of the total value of  $\bar{S}_d^t$  for the personnel and the population. Under these conditions it is reasonable, in our opinion, to choose the smallest  $E$  ( $E_{\text{min}}$ ) of the values recommended in the literature: first, when  $E_{\text{min}}$  is used the upper limiting value (other conditions remaining the same) is obtained for  $\bar{S}_d^t$ ; second,  $\bar{S}_d^t$  does not change very much with a possible transition to a more correct value of  $E$ . The values of  $E$  recommended in the domestic literature are in the range  $0.08$ - $0.15 \text{ yr}^{-1}$  (see, e.g., [5], as well as [9]). On the basis of the considerations presented above in this paper we have chosen†  $E = 0.08 \text{ yr}^{-1}$ .

Other (noneconomic) factors which could be used in the integrand in Eq. (6) are completely indeterminate at the present time. It should be understood, however, that their possible inclusion in (6), equivalent to some variation of  $E$ , cannot have a major effect on  $\bar{S}_d^t$  for the NFC (see the considerations above about the choice of  $E$  and about the dependence of  $\bar{S}_d^t$  on  $E$ ). In view of this, we can speak of the distinct, fundamental value of the economic discounting factor among all probable time factors mentioned earlier.

Economic truncation of the range of integration in (6) results in our ignoring the irradiation dose received by the population in comparatively long times  $t > \tau_{\text{ec}}$ . It may turn out that this characteristic of  $\bar{S}_d^t$  for the NFC causes unacceptable contradictions between generations: The advantage from economies in expenditures on building protective structures will be enjoyed by our generation, while the greater part of the harm from the radioactive contamination of the biosphere will befall the next generation. In actual fact, there is no contradiction. A positive discounting norm  $E$  corresponds to a development of society such that part of the material goods is transferred to the accumulated fund, i.e., for a continuous improvement of future living conditions. As a result, the present generation will hand over to the next generation a larger volume of material goods than it received as it started life.

Under such conditions the appearance of additional means at some time, e.g., because of a reasonable saving of means in building protective installations in NFC facilities, will benefit both the present generation and generations to come (because these means are transferred partially into the consumption fund and partially into the accumulated fund). Conversely, both the present generation and coming generations will suffer material loss if because of an incorrect economic assessment excessive funds are expended on protective installations. In particular, such an error occurs if the total and not the discounted expected dose is used as the basis for the assessment of the harm. It must be pointed out that the decrease which an economic error caused in the accumulated fund passed on to the next generation grows exponentially with time.

Thus, as a compensation for a relatively slight increase in the radiation background, future generations will receive growing material means, part of which could be spent on public health protection. This can be

\* The possible dependence of  $\gamma$  on  $t$  must be taken into account in exactly the same way as is the dependence  $E(t)$  [see (7)].

† When the problem of the choice of  $E$  is raised in international scientific organizations, it may become necessary to reduce this value somewhat.

done by: reducing the technogenic addition to the background irradiation of man (by improving the medical diagnostic apparatus, constructing buildings from building materials with a lower content of natural radionuclides, etc.); employing prophylactic social and medical measures to protect and improve public health; and improving medical services.

At the present time the technogenic addition to the natural background is fairly substantial. According to the data of [10], for the population of the USSR this correction  $\Delta\bar{H}^{(T)}$  to the average individual yearly dose is  $\sim 3$  msievert, on average. In the main it comes from medical diagnostic procedures ( $\sim 1.5$  msievert) and the natural radionuclides in building materials ( $\sim 1.3$  msievert). In principle, one can pose the problem of greatly decreasing  $\Delta\bar{H}^{(T)}$ , but solving it at this time or in the near future would involve colossal expenditures which society today would not afford. In the distant future these same expenditures, converted to the present time, decrease manyfold and the further into the future they are removed, the more they are reduced. It is important to point out that the correction  $\Delta\bar{H}_{NP}^{(T)}$ , due to long-lived radionuclides of the NFC, to the present-day total  $\Delta\bar{H}^{(T)}$  is relatively small at any planned or predicted level of nuclear power development (with the present-day technology for handling wastes with a high specific activity, including their vitrification and burial at great depths).

## CONCLUSIONS AND PROPOSALS

1. With the economic approach to estimation of the harm from radioactive contamination of the biosphere, the economic comparison of the degree of the effect of various technologies, stages of the NFC, etc., on the biosphere, and the application of the benefit-harm criterion for the purposes of optimization of the safety system of facilities, it is necessary to employ discounting of the magnitude of the harm, in particular, the discounted expected dose  $\bar{S}_d^t$  instead of the total expected dose.\* In the opinion of the present authors, in the final table of the report of the United Nations Scientific Committee on the Effect of Atomic Radiation (see [1], Vol. 1, pp. 33, 372), characterizing the radiation effect of the NFC on the population, it would be more correct to indicate the discounted and not the total values of the doses.

2. For a present-day nuclear fuel cycle,  $\bar{S}_d^t$  is two to three orders of magnitude smaller than the total expected dose  $S^t$  (see Table 1). Clearly, this relation between  $\bar{S}_d^t$  and  $S^t$  is maintained for future NFC as well.

3. It is proposed that a new concept, that of discounted collective expected dose (see Eq. (6)) be added to the definitions of the expected dose.†

The authors express their heartfelt thanks to V. A. Legasov, N. N. Ponomarev-Stepen', and I. I. Kuz'min for support and valuable critical comments.

We also thank N. G. Gusev for informing us about [12-14].

## LITERATURE CITED

1. Sources and Effect of Ionizing Radiation. 1977 Report of the United Nations Scientific Committee on the Effect of Atomic Radiation of the United Nations General Assembly, United Nations Organization, New York (1978); also 1982 report.
2. International Assessment of Nuclear Fuel Cycle, IAEA, Vienna (1980), p. 7.
3. L. A. Buldakov et al., Radiation Safety in the Atomic Power Industry [in Russian], Atomizdat, Moscow (1981).
4. Recommendation of International Commission on Radiation Safety. Publication No. 26 [in Russian], Atomizdat, Moscow (1978).
5. L. I. Lopatnikov, Shorter Economic-Mathematical Dictionary [in Russian], Nauka, Moscow (1979).

\* The collective dose criterion should be employed with the simultaneous imposition of a limitation on the maximum value of the individual yearly dose (in accordance with the recommendations of the International Commission on Radiological Protection (see Sec. 76 [4]).

† The principal statements of this paper in the form of a report were sent to the United Nations Scientific Committee on the Effect of Atomic Radiation in July, 1981 [11]. The authors received several responses and comments on the report. Publications [12-14] that have appeared have in one form or another taken up the topics considered in the present paper. We suggest that our paper, which is more complete than [11], contains answers to questions that arose and comments made, particularly concerning the choice of the value of  $E$ , the sense of  $E$  and  $\bar{S}_d^t$ , and the fact that Eq. (6) contains no correction for inflation.

6. J. Ahmed and H. Daw, Cost-Benefit Analysis and Radiation Protection. IAEA Bulletin, (1980), Vol. 22, No. 5/6, p. 13.
7. Recommendations of International Commission on Radiation Protection. Publication No. 22 [in Russian], Atomizdat, Moscow (1975).
8. Nuclear News, 24, No. 11, 144 (1981).
9. W. Hafele et al., Fusion and Fast Breeder Reactors. IIASA, RR-77-8, Austria (1977).
10. N. S. Babaev et al., in: Nuclear Power, Man, and the Environment [in Russian], A. P. Aleksandrov, (ed.), Energoizdat, Moscow (1981).
11. V. Demin, Preprint IAE-3524/3, Institute of Atomic Energy, Moscow (1981).
12. B. Cohen, Bull. At. Scientists, 32, 61 (1976).
13. H. Gjorup, in: Proc. Int. Conf. Nuclear Power and Fuel Cycle, Salzburg, May 2-3, 1977, IAEA, Vienna (1977), Vol. 4, p. 303.
14. H. Bonka and H. Horn, in: Fifth Int. Congr. IRPA, Israel, March 9-14, 1980, Israel (1980), Vol. 1, p. 29.

## LETTERS TO THE EDITOR

## EXPERIMENTAL DATA ON THE NEUTRON FIELDS OF THE VVÉR-440

S. S. Lomakin, A. G. Morozov,  
G. G. Panfilov, Kh. Ya. Bondars,  
and A. A. Lapenas

UDC 621.039.512.45

The parameters of the neutron fields in the circumvessel space of the VVÉR are investigated by the authors on actual nuclear power stations (NPS), in order to assess the quality of the radiation shielding, to refine the radiation lifetime of the plant, and to verify the calculated data and computational programs [1-3]. The volume of experimental investigations carried out on almost all nuclear power station units with VVÉR-440 allows the data obtained about the composition and level of the neutron radiation to be compared and generalized.

The measurements were carried out in front of and behind the reactor vessel, and also in the channels of the ionization chambers (IC) located in the radiation shield in the vicinity of the reactor vessel. For the measurements in front of and behind the reactor vessel, special channels were used, ensuring the necessary location of the neutron detectors.

The measurements were carried out by the activation method. The fast-neutron flux density was determined with threshold detectors, containing  $^{103}\text{Rh}$ ,  $^{115}\text{In}$ ,  $^{58}\text{Ni}$ ,  $^{54}\text{Fe}$ ,  $^{124}\text{Mg}$ ,  $^{27}\text{Al}$ , and  $^{127}\text{I}$ , and for the determination of the spectral parameters and the thermal-neutron flux density, detectors with  $^{115}\text{In}$ ,  $^{197}\text{Au}$ ,  $^{140}\text{La}$ ,  $^{151}\text{Sm}$ ,  $^{63}\text{Cu}$ ,  $^{55}\text{Mn}$ , and  $^{176}\text{Lu}$  were used.

The thermal-neutron field behind the reactor is formed by fast-fission neutrons which have passed through the radiation shield and the reactor vessel. At the sites of location of the IC, these neutrons were moderated and thermalized in the medium surrounding the IC channels.

At the Novovoronezh and Kol'sk nuclear power stations, the IC channels are located behind the reactor vessel in water tanks, and at Armyan they are in the concrete of the dry shield. Table I gives the measured values of the neutron flux density  $nV_0$ , the Maxwell distribution temperatures  $T$ , and the epithermal parameter  $r\sqrt{T/T_0}$  ( $V_0 = 2200$  m/sec.  $T_0 = 293^\circ\text{K}$ ). All data are averaged over the units of these nuclear power stations with IC channels in the water tanks or in the dry shield. The position of the control organs in the measurements corresponded to the normal working range.

It can be seen that the thermal neutron spectrum in the IC channels located in the concrete shield is somewhat "harder," mainly because of the presence of the iron reinforcement in the concrete shield. Repeated measurements showed that the thermal-neutron field behind the reactor vessel in the IC channels is characterized by stability, and is independent of the fuel burnup and the concentration of boric acid in the core.

TABLE 1. Thermal-Neutron Field Parameters in the IC Channels

Location of IC channel	$nV_0$ , neutrons/[ $\text{cm}^2 \cdot$ sec $\cdot$ MW (t.)]	$T$ , °K	$r\sqrt{T/T_0}$
Water tank	$(14,6 \pm 0,7) \cdot 10^6$	$409 \pm 13$	$0,08 \pm 0,01$
Concrete shield	$(3,8 \pm 0,2) \cdot 10^6$	$550 \pm 14$	$0,13 \pm 0,01$

Translated from Atomnaya Énergiya, Vol. 54, No. 3, pp. 200-201, March, 1983. Original article submitted March 18, 1982.

TABLE 2. Fast-Neutron Flux at the Inside Surface of the Reactor Vessel and Behind the Reactor Vessel, neutrons/[cm<sup>2</sup> · sec · MW(t.)]

NPS	Unit	At the inside surface of the reactor vessel	Behind the reactor vessel
Novovoronezh	Second	0,83 · 10 <sup>8</sup> (R = 176,4 cm)	1,21 · 10 <sup>7</sup> (R = 190,5 cm)
Armyan	First	—	0,73 · 10 <sup>7</sup> (R = 237 cm)
Kol'sk	The same	0,80 · 10 <sup>8</sup> * (R = 178 cm)	

\*Calculation by the RADUGA program [4], normalized on measurements in the IC channel and in the core.

TABLE 3. Values of  $\varphi$  in the IC channels

NPS	Unit	$\varphi$ (E > 1 MeV) neutron/[cm <sup>2</sup> · sec · MW (t.)]	R, cm
Voronezh	Third	2,04 · 10 <sup>6</sup>	214
	Fourth	2,33 · 10 <sup>6</sup>	214
Armyan	First	0,94 · 10 <sup>6</sup>	255
Kol'sk	First	1,96 · 10 <sup>6</sup>	214

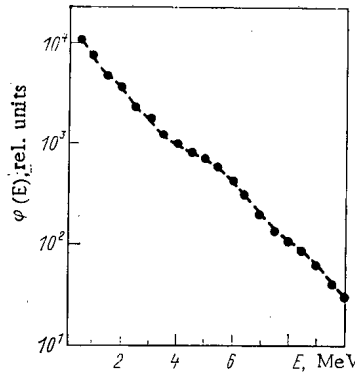


Fig. 1. Energy distribution of the fast-neutron flux density ( $\varphi$ ) in the VVER-440 vessel.

The fast-neutron flux density was determined in the circumvessel space of these nuclear power stations. The values of the fast-neutron flux density  $\varphi$  with energy in excess of 1.0 MeV at the level of the center of the core, and the distance R from the center of the core to the measurements sites, are given in Tables 2 and 3.

The greatest number of measurements was carried out in the IC channels, access to which is relatively simple. The data obtained are given in Table 3. The errors in the measured values of  $\varphi$  are within the limits of  $\pm 25\%$  for a 95% level of the confidence coefficient.

An analysis of the data obtained shows their agreement with the structural features of the nuclear power station units and their similarity when there is no difference in the units. The tables give the values of  $\varphi$  (E > 1.0 MeV) by which the nuclear power station units are compared. For an estimate of the radiation lifetime of the reactor plant, the present-day approach requires a knowledge of the energy dependence of the neutron flux density  $\varphi(E)$  and consideration of the action of the neutrons on the material, starting with an energy of 0.1–0.6 MeV. For the inside surface of the VVER vessel (second unit of the Novovoronezh nuclear power station), Fig. 1 shows the differential density, restored by the SAND II method from the obtained experimental data. The method

of restoration used, and also the errors of the cross sections and the measured rate of activation, lead to a spread of the values obtained for  $\varphi(E)$  for an energy in excess of 0.6 MeV, equal to  $\pm 32\%$ .

## LITERATURE CITED

1. S. S. Lomakin et al., *At. Energ.*, **31**, No. 1, 54 (1971).
2. L. I. Golubev, et al., *At. Energ.*, **44**, No. 5, 458 (1978).
3. Kh. Ya. Bondaras et al., in: *Radiation Safety and Shielding of Nuclear Power Stations* [in Russian], No. 5, Atomizdat, Moscow (1981), p. 143.
4. L. P. Bass et al., in: *Radiation Safety and Shielding of Nuclear Power Stations* [in Russian], No. 3, Atomizdat, Moscow (1977).

EFFECTS OF PRELIMINARY FEW-CYCLE LOADING  
ON THE RADIATION EMBRITTLEMENT OF 15Kh2MFA STEEL

L. A. Vainer and B. T. Timofeev

UDC 620.171

The shell of a reactor undergoes cyclic thermomechanical loading during operation, and this produces maximal stresses exceeding the yield point in stress-concentrator zones. This few-cycle loading may alter the critical brittleness temperature and the tendency to radiation embrittlement. The general considerations here are as follows:

The studies were made on 15Kh2MFA steel. The heat treatment consisted in quenching with subsequent high tempering, which produced a homogeneous structure. The steel had the following mass % composition: C - 0.18, Si - 0.30, Mn - 0.50, S - 0.012, P - 0.017, Cr - 2.60, Mo - 0.76, V - 0.29, Ni - 0.20, Cu - 0.12; the mechanical properties at 293°K were as follows:  $\sigma_{0.2} = 470$  MPa,  $S_K = 1510$  MPa,  $\psi_K = 76\%$ ,  $KCV_{max} = 1900$  kJ/m<sup>2</sup>.

The few-cycle loading was applied to specimens with working cross sections of  $10 \times 30$  mm using a UMÉ-10TM test machine at room temperature. The working-life curve for the material was used in selecting a deformation amplitude  $\bar{\epsilon} = 1.2$ , which corresponds to 30,000 cycles to failure. Then one batch of the specimens was loaded with 300 cycles of this amplitude, which corresponded to  $0.01 N_K = 0.1$  [N], where  $N_K$  is the number of cycles to failure and [N] is the permissible number of cycles laid down in "Strength-Calculation Norms." The second batch of specimens received 3000 cycles ( $0.1 N_K = [N]$ ).

The working parts of the specimens tested in few-cycle fatigue were used in making smaller ( $5 \times 4 \times 27.5$  mm) specimens with V notches for impact-viscosity testing. All the specimens used in determining the impact viscosity (including those after few-cycle fatigue) after preparation were kept at 500°C for 500 h.

Some of the specimens from the three batches were irradiated in the VVR-M reactor of the Academy of Sciences of the USSR to an integral fluence of  $10^{24}$  neutrons/m<sup>2</sup> ( $E > 0.5$  MeV) at  $275 \pm 25^\circ\text{C}$  and up to  $3 \cdot 10^{24}$  neutrons/m<sup>2</sup> at  $375 \pm 25^\circ\text{C}$ . The initial and irradiated specimens were examined with an MK-1.5 pendulum striker. For this purpose, at temperatures between  $-100$  and  $+20^\circ\text{C}$  the specimens were placed in alcohol cooled with liquid nitrogen, while for lower temperatures the specimens were cooled by liquid nitrogen or nitrogen vapor. Metallography of the fractures in metal with few-cycle damage showed that there were no microcracks.

Figure 1 shows the impact-viscosity tests on the initial and irradiated 15Kh2MFA steel specimens with and without few-cycle damage. The above conditions of few-cycle loading do not alter the critical brittleness temperature of 15Kh2MFA steel within limits of  $\pm 10^\circ\text{C}$ . Also, the impact-viscosity curves in the absence of few-cycle loading or after such loading with numbers of cycles corresponding to  $0.01 N_K = 0.1$  [N] and  $0.1 N_K = [N]$  are practically the same, not only in the initial state, but also after neutron irradiation at  $275 \pm 25^\circ\text{C}$  to a fluence of  $10^{24}$  neutrons/m<sup>2</sup> and at  $375 \pm 25^\circ\text{C}$  to a fluence of  $3 \cdot 10^{24}$  neutrons/m<sup>2</sup>. In that case, the increases in the critical brittleness temperature determined from tests on small specimens for impact viscosity were

Translated from *Atomnaya Énergiya*, Vol. 54, No. 3, pp.201-202, March, 1983. Original article submitted April 1, 1982.

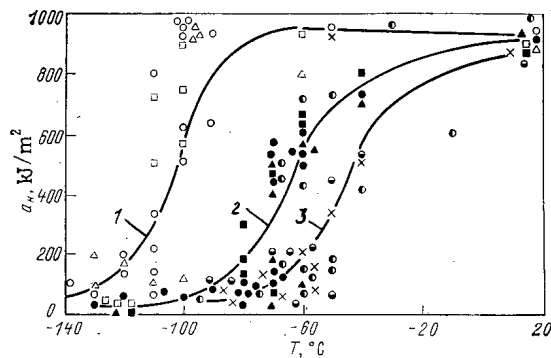


Fig. 1. Change in the temperature dependence of the impact viscosity for 15Kh2MFA steel in response to few-cycle loading and neutron irradiation: 1 (○, □, △) without irradiation; 2 (●, ■, ▲) after irradiation with a fluence of  $10^{24}$  neutrons/m<sup>2</sup> at  $275 \pm 25^\circ\text{C}$ ; 3 (●, ×, ●) after irradiation with a fluence of  $3 \cdot 10^{24}$  neutrons/m<sup>2</sup> at  $375 \pm 25^\circ\text{C}$ ; ○, ●, ● without preliminary loading; □, ■, × 300 loading cycles; △, ▲, ● 3000 loading cycles.

40 and  $60^\circ\text{C}$ , correspondingly, for fluences of  $10^{24}$  and  $3 \cdot 10^{24}$  neutrons/m<sup>2</sup>, which are approximately equal to the increment in the critical brittleness temperature determined on specimens of type IV in accordance with All-Union State Standard 9454-60 for the same steel after analogous irradiation treatments (L. A. Vainer, I. A. Razov, and A. S. Teshchenko, *Fiz. Met. Metalloved.*, 42, No. 5, 971 (1976)).

The data indicate that preliminary few-cycle loading close to that experienced by reactor pressure vessels does not affect the critical brittleness temperature in 15Kh2MFA steel or the radiation embrittlement.

GENERATING PURE BEAMS OF NUCLEI IN THE  
SYNCHROPHASOTRON OF THE JOINT INSTITUTE  
OF NUCLEAR RESEARCH

UDC 539.1

Yu. D. Beznogikh, V. P. Vadeev,  
M. A. Voevodin, V. I. Volkov,  
E. D. Donets, V. G. Dudnikov,  
L. P. Zinov'ev, V. A. Monchinskii,  
A. I. Pikin, I. N. Semenyushkin,  
V. M. Slepnev, S. A. Khorozov,  
and A. P. Tsarenkov

In 1982 the outstanding Soviet physicist, the founder and first director of the High-Energy Laboratory of the Joint Institute of Nuclear Research, academician V. I. Veksler had his 70th birthday.

One of the most important stages in the development of Russian and Western accelerators was the synchrophasotron built in Dubna under the supervision of V. I. Veksler. Bold and far-reaching scientific and technological solutions introduced in this accelerator made it possible to use the synchrophasotron at the beginning of the seventies for new unique applications, mainly for accelerating nuclei to record energies [1]. The new energy range of accelerated beams of nuclei stimulated rapid development of research in a new direction: relativistic nuclear physics [2].

Beams of nuclei of elements which are heavier than helium, particularly beams of carbon ( $C^{6+}$ ), were regularly accelerated and used in physics experiments made since 1977 on the synchrophasotron of the Joint Institute of Nuclear Research [3, 4]. The cryogenic electron-beam ionizing unit "Krion," built in the High-Energy Laboratory, has been employed as a source of nuclei [5, 3]. This source provides beams of nuclei even of heavier elements, such as  $O^{8+}$  and  $Ne^{10+}$ . Beams of even still heavier nuclei, particularly of  $Ar^{18+}$  and of the heliumlike xenon  $Xe^{52+}$  ions, have been obtained from the Krion-2 source built for research work [6]. As far as the mass is concerned, beams which can be accelerated to relativistic energies are at the present time basically limited by losses in the course of the synchrotron acceleration; the losses originate from the capture of electrons by nuclei of the beam in collisions with atoms of the residual gas in the synchrophasotron chamber. For example, when the carbon nuclei are accelerated, only  $(2-4) \cdot 10^6$  nuclei reach the final energy of  $\sim 4.0$  GeV/nucleon from the  $(1-2) \cdot 10^8$  nuclei injected into the ring, i.e., the attenuation coefficient, which includes all sources of losses, is 50-100.

In the transition to the acceleration of neon, the coefficient rises sharply due to losses in the residual gas, and the neon nuclei are apparently the heaviest particles which still can be accelerated in the synchrophasotron at injection energies of 5 MeV/nucleon and pressures of  $2.76 \cdot 10^{-4}$  Pa in the accelerator chamber. Attempts to accelerate neon nuclei have been made earlier [3, 4]. Tracer amounts of relativistic  $^{20}Ne$  nuclei

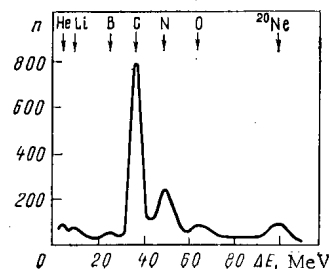


Fig. 1. Spectral composition of the relativistic beam of nuclei in the slow extraction channel during the acceleration of  $^{20}Ne$ .

Translated from *Atomnaya Énergiya*, Vol. 54, No. 3, pp. 202-203, March, 1983. Original article submitted April 16, 1982.

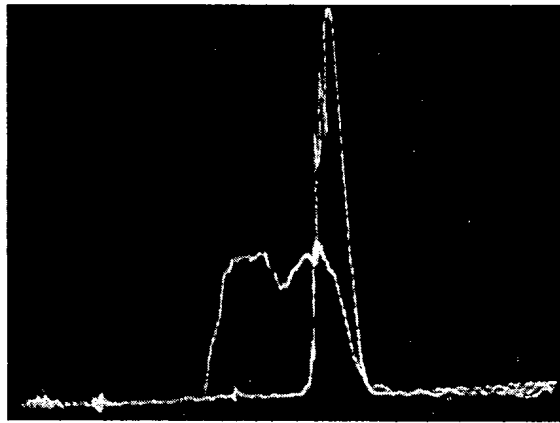


Fig. 2. Circulating  $^{22}\text{Ne}$  beam and beam injected onto the target in betatron operation. Length of the beam pulse obtained from the target  $150\ \mu\text{sec}$  on the base line;  $N_{\text{LU-20}} = 5 \cdot 10^6$  particles/pulse;  $N_{\beta} = 3.5 \cdot 10^6$  particles/pulse.

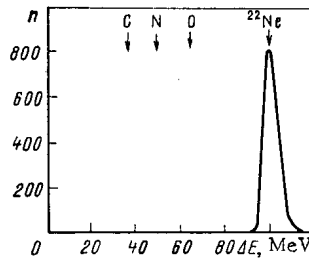


Fig. 3. Spectral composition of the relativistic beam of nuclei in the slow extraction channel during  $^{22}\text{Ne}$  acceleration.

( $\sim 10^2$  particles/pulse) of final energy have been recorded and the pattern of the interaction with nuclei in a streamer chamber has been derived. Such extremely small quantities of accelerated particles could suffice for efficient physics research only when track detectors in the form of nuclear emulsions and bubble chambers are employed. Admixtures to the  $^{20}\text{Ne}$  beam (He, C, N, and O) pose difficulties (Fig. 1).

These admixtures are usually present in the beam of nuclei obtained from the ionizing unit. The admixtures are produced in very small quantities from the elements of the residual gas, but owing to the high attenuation coefficient of the  $^{20}\text{Ne}$  nuclei beam during its acceleration, the beam appears to be enriched by nuclei of lighter elements. It seems that this effect can be precluded by using an isotope with an A/Z ratio differing from 2.  $^{22}\text{Ne}$  seems to be most appropriate in the case of neon. The acceleration of the  $^{22}\text{Ne}$  nuclei to 73 GeV in the synchrophasotron was achieved at the end of the December working period of carbon acceleration. A vacuum of  $2.40 \cdot 10^{-4}$  Pa was obtained by that time in the accelerator chamber. The ionizing unit Krion was operated at low power: The electron-beam current was  $\sim 50$  mA, which corresponds to a current density of  $\sim 60$  A/cm<sup>2</sup> in the beam; the beam energy was  $\sim 8$  keV at 50% recuperation; the ion delay time was  $\sim 300$  msec.

When compared with the nominal operation in the case of neon, the above conditions of operation provided only a 10% fraction of nuclei in the beam. In this case the admixture gases in the electron beam were minimal. This was extremely important in the first experiment on the acceleration of  $^{22}\text{Ne}$  nuclei. Since in the case of this isotope we have A/Z = 2.2 rather than 2 as in the nuclei usually accelerated in the synchrophasotron, the transition to the acceleration of  $^{22}\text{Ne}$  necessitated changes in the parameters of the accelerating LU-20 equipment and the high-frequency system of the synchrophasotron. The voltage applied to the accelerating tube of the preinjector of the equipment was raised along with the accelerating voltage of the high-frequency field in the resonator; the  $^{22}\text{Ne}$  nuclei were injected into the chamber of the synchrophasotron in a magnetic field of 258 G in distinction to the 236 G used in the acceleration of particles with A/Z = 2. Figure 2 is an oscillogram of the beam circulating and ejected onto a betatron target in betatron operation.

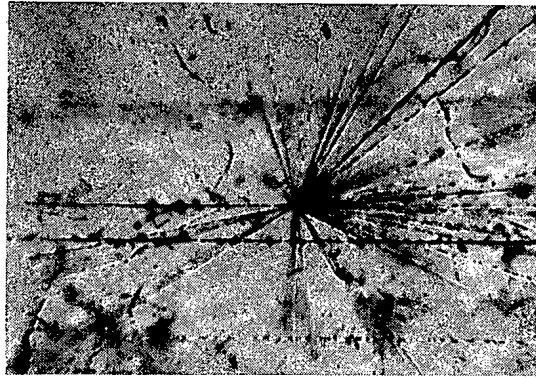


Fig. 4. Tracks of 73 GeV  $^{22}\text{Ne}$  nuclei in a photoemulsion (an inelastic process between one of the nuclei and a nucleus of the photoemulsion has occurred).

The  $^{22}\text{Ne}$  acceleration required significant readjustment of the relation governing the frequency of the accelerating voltage and the magnetic field in the synchrophasotron. The adjustment, which provided for only nominal beam losses during the acceleration process, was as follows:

1) the real dependence of the coupling law was recorded at 80 points of the magnetic field [7] during the acceleration of carbon nuclei;

2) corrections for the frequency of the accelerating voltage were calculated at these points of the magnetic field;

3) the coupling law was adjusted, taking into account the corrections calculated for the acceleration of  $^{22}\text{Ne}$  nuclei; and

4) the coupling law was corrected with the aid of a multichannel ionization sensor mounted in the vacuum chamber of the synchrophasotron and operated on-line with an ES-1010 computer [8].

A pure beam of  $^{22}\text{Ne}$  nuclei was obtained as the result of our work in the slow extraction channel of the synchrophasotron. Figure 3 shows the spectral composition of the extracted beam at energy 73 GeV. The accelerated beam reached an intensity of  $(1-2) \cdot 10^3$  particles/pulse. The first physics experiments were made with the relativistic  $^{22}\text{Ne}$  beam; in particular, the effective cross sections of inelastic interactions between  $^{22}\text{Ne}$  nuclei and C, Al, Cu, and Pb nuclei were measured and more than ten stacks of nuclear emulsions were irradiated. Figure 4 shows an interaction of a  $^{22}\text{Ne}$  nucleus with a nucleus of the photoemulsion.

This technique of generating pure beams of relativistic nuclei is of great interest for research on the dependence of the cross section upon the atomic number (particularly of the so-called enhanced or abnormal A dependencies) and for the search for extreme states of nuclear matter by investigating secondary interactions of nuclear fragments. It will be possible to significantly increase the beam intensity of the nuclei in the synchrophasotron and to broaden the beam composition after the following measures have been taken: putting into operation cryogenic pumping of the accelerator [9]; developing more powerful sources of heavy nuclei, especially development work on the electron-beam ionizing unit, and modernizing the injector and carefully adjusting the magnetic fields and accelerating fields of the machine.

The authors thank A. M. Baldin for initiating the present work which is directed toward a broadening of the composition of nuclei accelerated in the synchrophasotron; the authors also thank the synchrophasotron personnel for the successful acceleration work.

#### LITERATURE CITED

1. A. M. Baldin et al., JINR R9-5442, Dubna (1970).
2. Synopsis of the History of Nuclear Physics Development in the USSR [in Russian], Naukova Dumka, Kiev (1982), p. 152.
3. A. M. Baldin et al., in: Trans. of the Tenth Int. Conf. on Accelerators of Charged High-Energy Particles [in Russian], Press of the Inst. of High-Energy Physics, Serpukhov (1977), p. 367.
4. V. P. Vadeev et al., JINR R7-10823, Dubna (1977).

5. E. D. Donets and A. I. Pikin, Zh. Tekh. Fiz., **45**, 2373 (1975).
6. E. D. Donets and V. P. Ovsyannikov, JINR R7-80-515, Dubna (1980).
7. A. I. Mikhailov, G. P. Puchkov, and A. P. Tsarenkov, JINR 9-10712, Dubna (1977).
8. V. I. Volkov et al., JINR 10-12273, Dubna (1979).
9. N. I. Balandikov et al., JINR R8-80-172, Dubna (1980).

LOCAL ANALYSIS OF  $^3\text{He}$  BY TRACK AUTORADIOGRAPHY  
OF THE  $^3\text{He}(n,p)^3\text{H}$  REACTION

E. E. Goncharov, G. G. Ryabova,  
and D. A. Sorochan

UDC 621.039.8: 621.039.531

At the present time there are not available any direct methods of local  $^4\text{He}$  analysis with a sensitivity and surface resolution as required for problems associated with a possible redistribution of implanted helium atoms over a surface. Indirect data on the position of implanted helium on grain boundaries and other surface defects can be obtained from investigations of blister formation on the TsM-6 molybdenum alloy [1, 2], but it is not possible to obtain information on the helium redistribution over the surface when the helium irradiation doses are below the dose causing the development of blisters.

To date no track autoradiographs of  $^3\text{He}$ -containing samples have been obtained, though it is possible to use the nuclear reaction  $^3\text{He}(n,p)^3\text{H}$  for investigating the local distribution of helium in materials with the aid of solid-state track detectors [3]. The reason seems to be that it is relatively difficult to prepare samples with a certain  $^3\text{He}$  concentration and to record both protons and  $^3\text{He}$  nuclei with solid-state track detectors.

Test samples with a known concentration and distribution of  $^3\text{He}$  in a region with a diameter of 3 mm were prepared by ion implantation. Polished KÉF-7.5 silicon plates with a size of  $8 \times 12$  mm were employed. A  $0.54\text{-}\mu\text{m}$ -thick  $\text{SiO}_2$  mask was applied to the sample surface by photolithography. The mask pattern comprised periodic rectangular and triangular figures with a size of a few to several hundred microns (Fig. 1a).

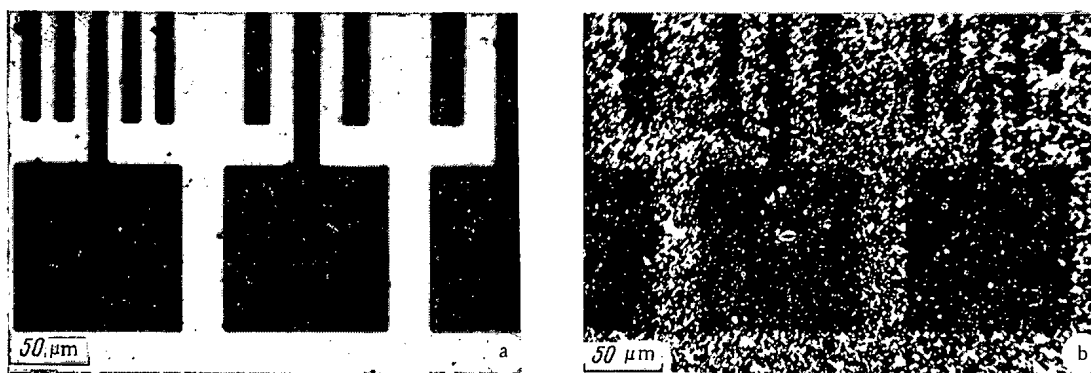


Fig. 1. Microphotographs of: a) an Si sample with an  $\text{SiO}_2$  mask on the surface; b) a track autoradiograph of the distribution of  $^3\text{He}$  implanted in the sample (distribution obtained after removal of the mask).

Translated from Atomnaya Énergiya, Vol. 54, No. 3, pp.204-205, March, 1983. Original article submitted May 10, 1982.

In the implantation of 18-keV  $^3\text{He}$  ions, the dose values were  $2.9 \cdot 10^{16}$ ,  $9.3 \cdot 10^{16}$ ,  $2.9 \cdot 10^{17}$ , and  $8.6 \cdot 10^{17}$  atoms/ $\text{m}^2$ , which correspond to current densities of  $0.5 \cdot 10^{-4}$ ,  $1.2 \cdot 10^{-4}$ ,  $2.4 \cdot 10^{-4}$ , and  $1.17 \cdot 10^{-3}$  A/ $\text{m}^2$ , respectively. The range of the 18-keV  $^3\text{He}$  ions in the  $\text{SiO}_2$  was  $\sim 0.16 \mu\text{m}$  [4], and therefore the helium was incident on the silicon only in areas not covered by the mask. After irradiation, the  $\text{SiO}_2$  mask was removed by etching in concentrated HF. Since the doses employed were much lower than the doses causing blister formation, and since the ion distribution over the beam cross section was uniform, it could be assumed that a uniform alloying of the samples had been achieved. In this case the surface concentration of  $^3\text{He}$  must correspond to the dose of the implanted ions.

Test samples and track detectors directly applied to them were irradiated in the IRT-2000 reactor with thermal neutrons to a flux density of  $2.5 \cdot 10^{12}$  neutrons/ $\text{cm}^2$ . Two types of solid-state track detectors were used: one of  $\text{C}_{12}\text{H}_{18}\text{O}_6$  acetobutyrate cellulose, and one of Kodak CN-85  $\text{C}_6\text{H}_8\text{O}_9\text{N}_3$  nitrate cellulose. The range of 18-keV  $^3\text{He}$  ions in silicon is  $\sim 0.2 \mu\text{m}$  in normal incidence [4]. The protons and  $^3\text{H}$  nuclei incident on a solid-state track detector pass through this layer and their energies are reduced by 567 and 166 keV, respectively [5]. It is a well-known fact that the solid-state track detectors employed do not allow the recording of  $^1\text{H}$  and  $^3\text{H}$  nuclei with energies below 550 keV [6] in the case of normal development. This was confirmed by control experiments with test samples. In order to increase the recording efficiency, solid-state track detectors irradiated with neutrons were exposed for 6 h at a distance of 8 cm from a DRSh-250-3 mercury-vapor quartz lamp. The exposure was made through a light filter with a transmission maximum of the ultraviolet radiation at wavelengths below 365 nm. An additional light filter, which absorbed red and infrared radiation, prevented the solid-state track detector from being heated. The exposed detectors were etched for 6 h in 35% KOH at 308 °K. In this fashion track autoradiographs of the  $^3\text{He}$  distribution were obtained. Mainly qualitative results were obtained with the nitrate cellulose detectors (see Fig. 1b). After catalytic etching of the acetobutyrate cellulose detectors in a solution of 35% KOH, 0.5% K $\text{OCl}$ , and 1 mg/ml of  $\text{CuSO}_4$  at 308 °K for 4 h, track autoradiographs resembling those shown in Fig. 1b were obtained.

The autoradiographs were observed and photographed with an MBI-15 optical microscope having a resolution of  $1 \mu\text{m}$ . The density  $\rho$  of protons and  $^3\text{H}$  nuclei incident on the solid-state track detectors was calculated with the formula  $\rho = \sigma FN (k_p + k_{^3\text{H}})$ , where  $\sigma$  is the cross section of the  $^3\text{He}(n,p)^3\text{H}$  reaction in the case of thermal neutrons;  $F$ , flux of thermal neutrons;  $N$ , surface concentration of  $^3\text{He}$  atoms; and  $k_p$ ,  $k_{^3\text{H}}$ , geometrical factors which determine the relation between 18-keV  $^3\text{He}$  ions in Si and the ranges of the products resulting from the  $^3\text{He}(n,p)^3\text{H}$  reaction. Thus, for  $R_{^3\text{He}} = 0.16 \mu\text{m}$ ,  $R_p(578 \text{ keV}) = 7.2 \mu\text{m}$ , and  $R_{^3\text{H}}(186 \text{ keV}) = 2.1 \mu\text{m}$  [4], we have  $k_p = k_{^3\text{H}} = 0.5$ , i.e., half of the particles generated during the exposure time are incident on the detector while the autoradiographic image is formed.

In the development process described above, the recording efficiency of the solid-state track detectors was  $\sim 50\%$  because the detectors record only protons (the range of the  $^3\text{H}$  nuclei is comparable with the thickness of the solid-state track detector layer removed by etching).

The detection limit of  $^3\text{He}$  is  $10^{16}$  and  $10^{14}$  atoms/ $\text{m}^2$  for acetobutyrate and nitrate celluloses, respectively. The reason is that a higher background of tracks is formed in the cellulose nitrate detector by the nuclear reaction  $^{14}\text{N}(n,p)^{14}\text{C}$ . The resolution can reach  $0.1 \mu\text{m}$  when weakly etched tracks are observed in an electron microscope. The results show that track autoradiography involving the  $^3\text{He}(n,p)^3\text{H}$  reaction can be used for nondestructive checking of the helium redistribution on the surface of a material.

The authors thank V. A. Kurnaev and A. V. Romanovskii for their help in the helium implantation and E. M. Rozenberg for help in preparing the samples.

#### LITERATURE CITED

1. D. M. Skorov et al., *At. Energ.*, **49**, No. 2, 130 (1980).
2. B. A. Kalin et al., *At. Energ.*, **51**, No. 6, 385 (1981).
3. Zhu and Run-sheng, *Phys. Energ. Fort. Phys. Nucl.*, **4**, No. 3, 356 (1980).
4. A. F. Burenkov et al., in: *Tables of the Parameters of the Spatial Distribution of Ion-Implanted Impurities* [in Russian], Belorussian State Univ., Minsk (1980).
5. C. Williamson et al., *Rap. CEA*, R 3042, Juillet (1966).
6. R. L. Fleischer et al., in: *Tracks of Charged Particles in Solids, Part 1, Methods of Track Investigations* [Russian translation], Énergoizdat, Moscow (1981), p. 25.

APPROXIMATE SOLUTION OF THE  $\gamma$ -QUANTA TRANSFER  
EQUATION IN STRAIGHT-AHEAD SCATTERING

V. P. Zhemchugov

UDC 539.125.52 + 621.039.51.12

The  $\gamma$ -quanta transfer equation in straight-ahead scattering takes the form [1]

$$\begin{aligned} \partial\Phi/\partial z + S(\alpha)\Phi(z, \alpha) &= \int_{\alpha_0}^{\alpha} A(\alpha' \rightarrow \alpha)\Phi(z, \alpha')d\alpha'; \\ \Phi(0, \alpha) &= g(\alpha), \end{aligned} \quad (1)$$

where  $\Phi(z, \alpha)$  is the differential (with respect to the energy density) flux of  $\gamma$  quanta at point  $z$  of space (in units of the path length of the greatest-energy  $\gamma$  quanta);  $\alpha = m_0c^2/E\gamma$ , relative wavelength of the  $\gamma$  quanta;  $\alpha_0$ , minimum wavelength of the radiation;  $S(\alpha) = \Sigma(\alpha)/\Sigma(\alpha_0)$ , total reaction cross section of the  $\gamma$  quanta, rel. units; and  $A(\alpha' \rightarrow \alpha) = \Sigma_S(\alpha' \rightarrow \alpha)/\Sigma(\alpha_0)$ , differential scattering cross section, rel. units. It is assumed that there are no internal sources in the medium, and that radiation with the spectrum  $g(\alpha)$  is incident at the boundary  $z = 0$ .

The accurate solutions of Eq. (1) given in [1, 2] may be used in practical problems only extremely rarely, and are of purely theoretical interest. In real calculations, Eq. (1) must be solved by one of the approximate numerical methods (the moment method, the successive-collision method, etc. [1]). Each of these methods has its deficiencies in terms of rapidity or accuracy, and the choice is determined by the conditions of the problem. The method proposed below is likewise not free of deficiencies, but it provides better speed and accuracy in a certain sufficiently broad range of the variables  $z$  and  $\alpha$ .

In addition to Eq. (1), the equation for the function  $\Psi(z, \alpha) = \exp[S(\alpha)z]\Phi(z, \alpha)$  will be considered

$$\begin{aligned} \partial\Psi/\partial z &= \int_{\alpha_0}^{\alpha} A(\alpha' \rightarrow \alpha)\exp[z\Delta(\alpha, \alpha')]\Psi(z, \alpha')d\alpha'; \\ \Psi(0, \alpha) &= g(\alpha), \end{aligned} \quad (2)$$

where  $\Delta(\alpha, \alpha') = S(\alpha) - S(\alpha')$ . The derivative with respect to the spatial variable  $z$  on the left-hand side of Eqs. (1) and (2) allows, together with the boundary conditions, recurrence relations to be obtained for finding the coefficients of the Taylor-series expansion of  $\Phi(z, \alpha)$  and  $\Psi(z, \alpha)$  in the vicinity of the point  $z = 0$ .

It is assumed that the function  $\Phi(z, \alpha)$  and, correspondingly, also the function  $\Psi(z, \alpha)$  are continuously differentiable with respect to  $z$  as many times as is necessary, and the solution of Eqs. (1), (2) will be sought in the form of the series

$$\Phi(z, \alpha) = \sum_{n=0}^{\infty} \varphi_n(\alpha) z^n/n!; \quad (3)$$

$$\Psi(z, \alpha) = \sum_{n=0}^{\infty} \psi_n(\alpha) z^n/n!; \quad (4)$$

where  $\varphi_n(\alpha) = \Phi_z^{(n)}(0, \alpha)$ ;  $\psi_n(\alpha) = \Psi_z^{(n)}(0, \alpha)$ . Differentiating Eqs. (1), (2)  $m$  times with respect to  $z$ , it is found that

$$\Phi_z^{(m+1)}(z, \alpha) = \int_{\alpha_0}^{\alpha} A(\alpha' \rightarrow \alpha)\Phi_z^{(m)}(z, \alpha')d\alpha' - S(\alpha)\Phi_z^{(m)}(z, \alpha);$$

$$\begin{aligned} \Psi_z^{(m+1)}(z, \alpha) &= \int_{\alpha_0}^{\alpha} A(\alpha' \rightarrow \alpha)\exp[z\Delta(\alpha, \alpha')] \times \\ &\times \left[ \sum_{h=0}^m C_m^h \Delta^{m-h} \Psi_z^{(h)}(z, \alpha') \right] d\alpha', \end{aligned}$$

Translated from *Atomnaya Énergiya*, Vol. 54, No. 3, pp. 205-206, March, 1983. Original article submitted May 24, 1982.

where  $C_m^k$  are Newtonian binomial coefficients. Substituting  $z = 0$  into the expressions obtained, recurrence relations are found for the coefficients of the expansions in Eqs. (3) and (4)

$$\varphi_{m+1}(\alpha) = \int_{\alpha_0}^{\alpha} A(\alpha' \rightarrow \alpha) \varphi_m(\alpha') d\alpha' + S(\alpha) \varphi_m(\alpha); \quad (5)$$

$$\psi_{m+1}(\alpha) = \int_{\alpha_0}^{\alpha} A(\alpha' \rightarrow \alpha) \left[ \sum_{k=0}^m C_m^k \Delta^{m-k} \psi_k(\alpha') \right] d\alpha', \quad (6)$$

where  $\varphi_0(\alpha) = \psi_0(\alpha) = g(\alpha)$ , in view of the boundary conditions. Analogous recurrence relations may be obtained if the solution of Eq. (1) is sought in the form

$$\Phi(z, \alpha) = \exp(-z) \sum_{n=0}^{\infty} f_n(\alpha) z^n. \quad (7)$$

In fact, substituting the expansion from Eq. (7) into Eq. (1), and comparing the coefficients of equal powers of  $z$ , it is found that

$$(m+1) f_{m+1}(\alpha) = \int_{\alpha_0}^{\alpha} A(\alpha' \rightarrow \alpha) f_m(\alpha') d\alpha' + [1 - S(\alpha)] f_m(\alpha), \quad (8)$$

where  $f_0(\alpha) = g(\alpha)$ .

Any of the recurrence relations allows the asymptotic behavior of the solution of Eq. (1) at small  $z$  to be found for problems of practical importance. As is known [1], the function  $A(\alpha' \rightarrow \alpha) = (\alpha_0/2)(\alpha'/\alpha)^2(\alpha'/\alpha + \alpha/\alpha')$  provides a sufficiently accurate description of the Compton scattering of  $\gamma$  quanta at high energies ( $\alpha'$ ,  $\alpha \ll 1$ ). Assuming that  $g(\alpha) = \delta(\alpha - \alpha_0)$  and using Eq. (8), it is found that

$$f_0(\alpha) = \delta(\alpha - \alpha_0); \quad f_1(\alpha) = A(\alpha_0 \rightarrow \alpha); \\ 2f_2(\alpha) = [1 - S(\alpha)] A(\alpha_0 \rightarrow \alpha) + (\alpha_0^2/3)(1 - \alpha_0^3/\alpha^3).$$

Then at small  $z$  the asymptote

$$\Phi(z, \alpha) = \exp(-z) \{ \delta(\alpha - \alpha_0) + zA(\alpha_0 \rightarrow \alpha) + \\ + (z^2/2) [A(\alpha_0 \rightarrow \alpha)(1 - S(\alpha)) + (\alpha_0^2/3)(1 - \alpha_0^3/\alpha^3)] \} \quad (9)$$

holds.

The recurrence relations in Eqs. (5), (8) look less laborious. It is clear, however, that the series in Eq. (3) will converge much more slowly, since the expansion in Eq. (3) takes no account of the asymptotic behavior of the function  $\Phi(z, \alpha)$  as  $z \rightarrow \infty$ .

Numerical investigation of the expansions in Eqs. (3), (4), and (7) have been performed for scatterers with contrasting properties: aluminum [ $h_S(\alpha) = \Sigma_S(\alpha)/\Sigma(\alpha) \approx 1$ ], a medium with weak absorption; uranium [ $h_S(\alpha) \ll 1$ ], a strongly absorbing material; iron [ $h_S(\alpha) < 1$ ], an intermediate material. The solutions are compared with solutions obtained by the moment method and the successive-collision method (which is regarded as more accurate but requires considerable machine time). The discrepancy between the solutions is regarded as negligible if the difference is no more than 2-3%. The integrals in all the recurrence relations are calculated by a Newton-Cotes quadrature formula of closed type with  $n = 2, 3, 4$  in a sufficiently small interval  $\Delta\alpha$ . The results of the numerical investigations permit the following conclusions to be drawn:

1. The series in Eq. (3) with expansion coefficients determined by Eq. (5) and a number of terms in the expansion  $N \leq 20$  gives the solution only for small  $z$  (for aluminum and iron,  $z \leq 5$ ; for uranium,  $z \leq 3$ ). The series in Eqs. (4) and (7), with the coefficients determined by Eqs. (6) and (8), respectively, provide sufficiently accurate solutions at  $z \leq 20$  over a broad energy range  $E_\gamma = 2.5-50$  MeV for all the given materials. With this number of terms, the series is relatively small, and oscillates from 5 to 20 as a function of the energy range and in particular the behavior of the functions  $S(\alpha)$  and  $h_S(\alpha)$  in this range.

2. Other conditions being equal, a smaller number of terms is required in the series of Eq. (4) than in Eq. (7) if the function  $S(\alpha)$  decreases; if it rises, however, then the series in Eq. (7) converges more rapidly. This is as would be expected, since the exponential preceding the sum in Eq. (7) takes account of the more-penetrating component of the radiation. In the case when the function  $S(\alpha)$  has a clearly expressed minimum, the number of terms in the expansions of Eqs. (4) and (7) is approximately equal with the same calculation accuracy.

3. The asymptote of Eq. (9) allows sufficiently accurate values of  $\Phi(z, \alpha)$  to be obtained over a broad energy range with  $z < 2$ . The integral characteristics are described by the asymptote in Eq. (9) with an error of less than 5% when  $z \leq 4$  for iron,  $z \leq 2$  for aluminum, and  $z \leq 1$  for uranium.

Thus, the method of solution of Eq. (1) based on Taylor-series expansion of the solution provides good accuracy over a broad range of  $\gamma$ -quantum energies and at sufficiently large distances from the source. It thus competes successfully with traditional methods such as the moment method and the successive-collision method, and is less laborious, i.e., requires much less computer time.

## LITERATURE CITED

1. U. Fano, L. Spenser, and M. Berger, Transfer of Gamma Radiation [Russian translation], Gosatomizdat, Moscow (1963).
2. V. P. Zhemchugov, At. Energ., 50, No. 2, 143 (1981).

TEMPERATURE DEPENDENCE OF THE SCATTERING CROSS SECTION  
OF COLD NEUTRONS IN DITOLYLMETHANE

Yu. M. Berzilov, V. E. Zhitarev,  
A. M. Motorin, S. B. Stepanov,  
and Yu. V. Sharanin

UDC 539.171.416.22: 621.039.532.6

Hydrocarbons of the diphenylmethane series for a long time have been considered potential high-temperature coolants [1] for, e.g., nuclear power generation. At the present time, the possible use of ditolylmethane ( $C_{15}H_{16}$ ) as a moderator-coolant in reactors for heating in remote areas is being investigated. To date no complete data on the properties of the materials are available. In calculations of the thermalization of neutrons one can find partial information (or no information at all) on the cross section of interaction of ditolylmethane with slow neutrons and on the influence of the state parameters of the scatterer upon the interaction with such neutrons. The present work had the goal of partially filling these gaps.

The investigation concerned the temperature dependence (in the interval 25-300°C) of the total interaction cross section of ditolylmethane with cold neutrons at wavelengths of 0.6-1.9 nm (energies of 2.3-0.23 meV). The cross section was determined with crystal spectrometers of the neutron duct + crystal type [2] in the horizontal channels of the IRT-2000 reactor of the MIFI. The spectra of cold neutrons were produced in double-bent polished brass tubes, the neutron ducts. A tube with a size of 10 × 23 × 4650 mm was used for measurements in the range 0.6-1.3 nm (2.3-0.48 meV) (the limit wavelength of the spectrum was  $\lambda_{\min} \approx 0.5$  nm, i.e.,  $E = 3.3$  meV); in the range 1.3-1.9 nm (0.48-0.23 meV), the tube had a size of 25 × 58 × 6000 mm ( $\lambda_{\min} \approx 0.9$  nm, i.e.,  $E = 1$  meV). Packages of sheets of fluorphlogopyte mica ( $d_{001} = 0.997$  nm) served as monochromators. The wavelength resolution was better than 4% and the concentration of neutrons of higher orders of reflection was less than 1% in the entire range of neutron energies considered. The solid angle under which the detector (SNM-51 counter) was visible from the sample was less than 0.003 sr. Ditolylmethane of the "pure" quality was used for the samples. The plane samples of the liquid had a thickness of 1.3 and 1.5 mm at room temperature; the thickness was determined with an error of 2% through the passage of water in the same container. The samples could be heated to 400°C (error 2-4°C) in a hermetically sealed container with "windows" of an aluminum alloy. The sample transmissivity was 0.2-0.5.

Table 1 lists the total cross section values for the interaction of ditolylmethane molecules with cold neutrons. The density values of the material were taken from [1]; the error of the density values did not exceed 1.5%. The cross section errors listed in the table comprise the thickness error and the sample-density error.

Previous experimental investigations of several hydrogen-containing liquids (e.g., [3, 4]) have shown that the scattering cross section of cold neutrons of sufficiently long wavelength ( $\lambda > 0.5-1.0$  nm,  $E < 3.3-0.8$  meV)

---

Translated from Atomnaya Énergiya, Vol. 54, No. 3, pp. 206-207, March, 1983. Original article submitted June 6, 1982.

TABLE 1. Total Cross Section ( $10^{-27}$  m<sup>2</sup>) of the Interaction of DitolyImethane Molecules with Cold Neutrons

T, °C	$\lambda$ , nm (E, meV)													
	0,6 (2,3)	0,7 (1,7)	0,8 (1,3)	0,9 (1,0)	1,0 (0,80)	1,1 (0,67)	1,2 (0,57)	1,3 (0,48)	1,4 (0,42)	1,5 (0,36)	1,6 (0,32)	1,7 (0,28)	1,8 (0,25)	1,9 (0,23)
25	184±10	183±6	199±6	206±6	217±5	225±6	232±6	241±6	247±7	250±7	263±7	283±7	277±8	296±8
80	185±10	200±6	213±6	227±6	229±6	247±6	264±7	268±7	276±8	304±10	294±8	319±8	323±8	338±8
130	201±10	211±6	223±6	241±6	255±7	266±7	283±7	295±7	304±9	316±8	337±9	345±9	365±9	373±9
180	205±10	225±7	240±7	257±7	274±7	286±7	296±7	317±8	318±8	324±8	352±8	372±9	381±10	415±9
240	213±11	232±7	250±7	272±7	291±7	305±8	319±8	340±9	367±10	372±9	407±10	415±9	436±11	469±11
300	221±11	245±7	267±7	288±8	322±8	328±8	352±9	368±9	380±11	399±11	430±12	436±11	465±12	483±11

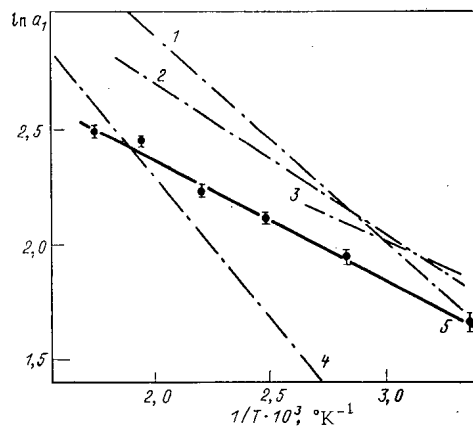


Fig. 1. Temperature dependence of  $\ln a_1$  in the case of: 1)  $H_2O$ ; 2)  $C_6H_6$ ; 3)  $C_7H_8$ ; 4)  $C_{10}H_{12}$  [4, 5]; 5) ditolyImethane (present work).

usually can be described with good precision by a linear function of the form  $\sigma_S(\lambda) = a_0 + a_1\lambda$ . The slope  $a_1$  of the straight line accounts for the contribution of the inelastic component  $\sigma_{ie}$  to the scattering cross section. The observed function  $\sigma_S(\lambda)$  corresponds to the general concept that the cross section  $\sigma_{ie}$  is proportional to the wavelength of the slow neutrons, the energy of which is much smaller than the characteristic energy transfer in scattering in the particular material. Our results have shown that ditolyImethane is a scattering system satisfying the above condition with the state parameters employed. It is therefore possible to use the results of investigations of the temperature dependence of the scattering cross section [3-5]; conclusions and estimates pertaining to the conditions of thermal motion in ditolyImethane can be made.

When the temperature dependence of the slope  $a_1(T)$  is considered in conjunction with the results of [4, 5] for several other materials, we can employ the exponential concept in accordance with [4, 5]:  $a_1(T) = a_{10} \exp(-\epsilon/kT)$  (see Fig. 1). These results indicate that on the average, hydrogen atoms in ditolyImethane perform relatively large free motions which considerably exceed those of, e.g., diphenyl (which is of similar molecular structure and viscosity). This conclusion is confirmed by the slope value, which is slightly smaller than that of water, benzene, and toluene at room temperature; the conclusion is further confirmed by the temperature dependence, which is closer to that of toluene:  $\epsilon_{C_{10}H_{12}} = 0.104$  eV;  $\epsilon_{H_2O} = 0.077$  eV;  $\epsilon_{C_6H_6} = 0.057$  eV;  $\epsilon_{DTM} = 0.046$  eV; and  $\epsilon_{C_7H_8} = 0.04$  eV.

Interestingly enough, toluene is characterized by the greatest mobility of the molecule as a whole and of the hydrogen atoms as well (according to the viscosity, self-diffusion, internal rotation data, etc.). The ditolyImethane molecule is substantially more complicated and heavier than the other molecules, but its viscosity is significantly higher [1]. Therefore, the mobility of the molecule as a whole (translations, rotations) is reduced. One must therefore assume that the ditolyImethane molecule can perform movements which are characterized by a high degree of freedom and the participation of a large number of hydrogen atoms. The outstanding indicators for the influence of quasifree movements upon the scattering cross section of the cold neutrons are the increased slope  $a_1$  at low temperatures and the reduced temperature dependence of the slope. An indicator of this influence is the ratio  $\epsilon/E$ , wherein  $E$  is the activation energy of viscous flow: For water

and diphenyl with strongly reduced molecular motions, we have  $\varepsilon/E = 0.5$ ; for benzene with a high barrier against rotation around the axis of sixth order, we have  $\varepsilon/E = 0.4$ ; for toluene with an almost free rotation of the methyl group and low viscosity, we have  $\varepsilon/E = 0.3$ ; and for ditolylmethane we have  $\varepsilon/E = 0.2$ . There is every reason to assume that only a high degree of rotational freedom of the methyl groups in the ditolylmethane molecule can account for all the listed properties of the scattering cross section. We find  $V_{CH_3} \leq k\bar{T} = 3.6$  kJ/mole for the average barrier against rotation of the methyl group (with  $\bar{T} = 436^\circ\text{K}$  denoting the average temperature of our experiments). When we use the recommendations of [4, 5], we obtain in a first approximation of the lower boundary of the remaining potential barriers against thermal motion of the ditolylmethane molecule:  $V_{\min}^{DTM} \approx \varepsilon_{DTM} = 4.4$  J/mole.

## LITERATURE CITED

1. Thermophysical Properties of Gases and Liquids [in Russian], Nauka, Moscow (1972).
2. S. B. Stepanov et al., in: Neutron Physics [in Russian], Vol. 4, FÉI, Obninsk (1974), p. 257.
3. J. Rush et al., J. Chem. Phys., 37, No. 2, 234 (1962).
4. V. E. Zhitarev et al., At. Energ., 46, No. 3, 190 (1979).
5. V. E. Zhitarev et al., At. Energ., 51, No. 3, 181 (1981).

DISCREPANCY OF THE RESULTS OF  $\bar{\nu}_p$  MEASUREMENTS  
IN THE FISSION OF  $^{237}\text{Np}$  NUCLEI BY NEUTRONS

V. V. Malinovskii, V. G. Vorob'eva,  
B. D. Kuz'minov, V. M. Piksaikin,  
N. N. Semenova, S. M. Solov'ev,  
and P. S. Soloshenkov

UDC 539.173

To date there have been published three papers [1-3] in which results of measurements of the average number  $\bar{\nu}_p$  of prompt neutrons in the fission of  $^{237}\text{Np}$  nuclei by monoenergetic neutrons have been presented. The discrepancy in the results of [1, 2] and [3] exceeds the measurement errors indicated by the authors. The cited work was done with various measurement techniques, and the discrepancy between the results attests to systematic errors.

The goal of the present work was to elucidate the possible reasons for discrepancies between our experimental data [2] and the data of [3]. The  $\bar{\nu}_p$  values obtained for  $^{238}\text{U}$  in [4] and [5, 6] by the same groups of researchers, under conditions resembling those of [2] and [3], respectively, coincide within the limits of the estimated measurement errors, but as far as the method is concerned, our work of [2] and [4] differs practically only by the correction to  $\bar{\nu}_p$  (4.7% in [2], and 0.2% in [4]). The correction depends upon the level of amplitude discrimination of the pulses generated in the ionization chamber by fission fragments.

Two versions of a fission chamber were used in [2]. The first chamber version consisted of six sections with ten double-face layers of a substance undergoing fission and contained a total amount of 130 mg of neptunium in each section. Even when the current pulses were used, a fission-event recording efficiency of about 55% could be obtained. In the second version, the chamber sections contained only one neptunium layer (7 mg). The maximum efficiency of recording fission fragments reached 80%. An extrapolation of the measured  $\bar{\nu}_p$  to the  $\bar{\nu}_p$  value at 100% recording efficiency of fission fragments was made with three  $\bar{\nu}_p$  values, one of which had been obtained with the first version of the fission chamber (efficiency 55%), whereas the other two had been obtained with the second chamber version (recording efficiency 60 and 80%).

In the present work the dependence of the measured  $\bar{\nu}_p$  value upon the efficiency of recording fission fragments was investigated in greater detail. Uranous-uranic oxide layers with a thickness of about 1 mg/cm<sup>2</sup> and a low uniformly distributed admixture of  $^{252}\text{Cf}$  were used for the measurements. The chamber geometry corresponded to the second version [2]. Measurements at different amplitude discrimination levels for the pulses generated by the fission fragments were made with respect to an "infinitely thin"  $^{252}\text{Cf}$  layer.

---

Translated from Atomnaya Énergiya, Vol. 54, No. 3, pp. 208-209, March, 1983. Original article submitted July 12, 1982.

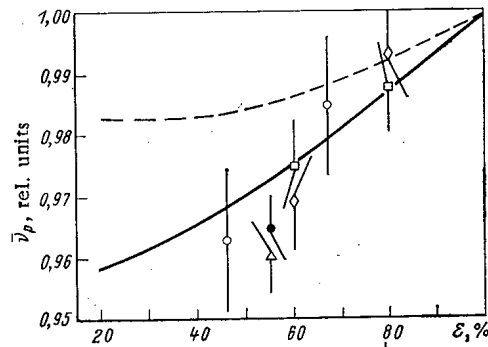


Fig. 1. Dependence of  $\bar{\nu}_p$  upon the efficiency  $\epsilon$  of recording fission fragments: ———, ———) results of measurements made with  $^{252}\text{Cf}$ -containing layers on  $^{237}\text{Np}$  at neutron energies 2.64 and 3.07 MeV, respectively;  $\diamond$  and  $\square$ ) fission-chamber sections with a single layer undergoing fission;  $\Delta$ ,  $\bullet$ ) sections consisting of ten layers;  $\circ$ ) results obtained with a spiral-shaped fission chamber at the neutron energy 2.0 MeV.

TABLE 1. Results of  $\bar{\nu}_p$  Measurements in the Fission of  $^{237}\text{Np}$  Nuclei by Neutrons

Neutron energy, MeV	Error in neutron energy (MeV)	$\bar{\nu}_p$	Statistical error
0.98	0.04	2.795	0.012
1.17	0.04	2.815	0.019
1.28	0.04	2.774	0.014
1.38	0.04	2.772	0.022
1.46	0.04	2.824	0.016
1.62	0.04	2.817	0.017
1.66	0.06	2.907 *	0.033
1.68	0.04	2.882	0.015
1.77	0.04	2.841	0.013
1.89	0.04	2.887	0.018
1.92	0.04	2.886	0.010
2.00	0.04	2.853	0.013
2.00	0.05	2.893 †	0.034
2.09	0.04	2.880	0.017
2.13	0.04	2.878	0.010
2.23	0.03	2.944	0.012
2.31	0.03	2.944	0.018
2.43	0.03	2.960	0.017
2.62	0.04	2.981	0.014
2.64	0.05	3.011 *	0.022
2.71	0.03	2.990	0.017
2.79	0.05	3.003 *	0.018
2.92	0.03	3.006	0.017
3.07	0.05	3.051 *	0.020
3.09	0.03	3.065	0.014
3.21	0.03	3.040	0.016
3.45	0.03	3.110	0.017
3.52	0.03	3.084	0.022
3.71	0.02	3.166	0.018
5.58	0.08	3.445	0.025
5.90	0.08	3.493	0.024

\* Results of measurements obtained with a fission chamber containing a single neptunium layer.

† Measurements made with a spiral-shaped fission chamber.

Figure 1 displays the results which we obtained. Each curve was determined with the least-square method applied to eight experimental points. The solid line corresponds to the case in which the sheet with the layer undergoing fission served as the collecting electrode. The dashed line corresponds to the reversed polarity of the chamber electrodes. The difference in the conditions of pulse shaping substantially manifests itself in the dependence under consideration.

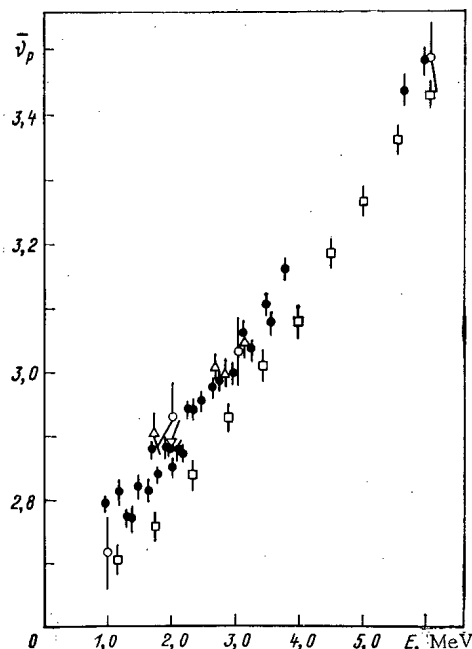


Fig. 2. Results of  $\bar{\nu}_p$  measurements in the fission of  $^{237}\text{Np}$  nuclei by neutrons: ○ [1]; □ [3]; ● data of [2] corrected in accordance with the present work; △) results of measurements made with fission-chamber sections containing a single neptunium layer; ▽) results of measurements made with a spiral-shaped fission chamber (only the statistical error of the measurements is shown for all the work).

The second chamber version [2] corresponds to the conditions under which the solid curve was obtained. The  $\bar{\nu}_p$  values in rel. units, measured in [2] with this chamber at the neutron energies 2.64 and 3.07 MeV, were renormalized and are shown in Fig. 1. Figure 1 includes the results of measurements performed with the first chamber version [2] at the same neutron energies. The result of a comparison of this data with the solid-line curve was a reduction of the correction for the discrimination of the fission events from 4.7 [2] to 3.7%.

The correction for the dependence of the measured  $\bar{\nu}_p$  value upon the thickness of the layer undergoing fission has been improved earlier. For the conditions of [2], the correction must be 0.3 instead of 0.1% of [2]. Thus, the results of the  $\bar{\nu}_p$  measurements indicated in [2] for  $^{237}\text{Np}$  must be reduced to 0.8%. Our investigation allowed us to determine the corrections for the discrimination of the fission events in the case of  $\bar{\nu}_p$  measurements made with the second chamber version and a recording efficiency of 80% of fission events at neutron energies of 1.66 and 2.79 MeV.

In our work we made measurements with a spiral-shaped ionization chamber for fission events in order to determine the optimal design of the fission chamber (combination of maximum recording efficiency of fission events with maximum loading of material undergoing fission). A neptunium layer with a thickness of 1 mg/cm<sup>2</sup> was applied to a 5-mm-broad aluminum foil. The gap between the electrodes was 0.5 mm, and the outer spiral diameter was 25 mm. The total amount of neptunium in the chamber was 55 mg. The chamber was filled with an argon-carbon dioxide mixture under a pressure of 304 kPa. Measurements were made for two efficiency values of recording fission fragments (45 and 70%) at a neutron energy of 2.0 MeV.

The corrected data of [2] and the results of our work are listed in Table 1. The assumption  $\bar{\nu}_p = 3.733$  was made for the spontaneous fission of  $^{252}\text{Cf}$ . The corrected  $\bar{\nu}_p$  values of [2] and the results of [1, 3] are compared in Fig. 2. Figure 2 also shows the  $\bar{\nu}_p$  values obtained in our work for  $^{237}\text{Np}$ . The systematic discrepancy between our results and the results of [3] still exists. The relative form of the energy dependence of  $\bar{\nu}_p$  is practically the same in the two investigations.

## LITERATURE CITED

1. L. Veaser, Phys. Rev., C17, No. 1, 385 (1978).
2. V. G. Vorob'eva et al., Problems of Atomic Science and Technology, Series "Nuclear Constants" [in Russian], No. 3(38), 44 (1980).
3. J. Frehaut, R. Bois, and A. Bertin, Note CEA-N-2196 (1981).
4. V. G. Vorob'eva et al., Problems of Atomic Science and Technology, Series "Nuclear Constants" [in Russian], No. 1(40), 62 (1981).
5. M. Soleilhac, J. Frehaut, and J. Gaurian, J. Nucl. Energy, 23, 257 (1969).
6. J. Frehaut, in: Neutron Physics [in Russian], Vol. 3, FEI, Obninsk (1974), p. 165.

AVERAGE NUMBER OF PROMPT NEUTRONS IN THE FISSION  
OF  $^{232}\text{Th}$  NUCLEI BY NEUTRONS

V. V. Malinovskii, V. G. Vorob'eva,  
B. D. Kuz'minov, V. M. Piksaikin,  
N. N. Semenova, V. S. Valyavkin,  
and S. M. Solov'ev

UDC 539.173

Measurements of the average number  $\bar{\nu}_p$  of prompt neutrons obtained in the fission of  $^{232}\text{Th}$  nuclei by neutrons have been described in [1-8]. An analysis of the results of [9] has shown that the experimental data do not suffice for developing a theory on the energy dependence of  $\bar{\nu}_p$  for practical applications and for considerations of the nuclear fission process per se. More particularly, the increase in  $\bar{\nu}_p$  found in the previous measurements of [4-6] in proportion to a decrease in excitation energy near the fission threshold has been denied in [7]. In the recently published paper [8], the effect was once more assumed to be real.

In our work we measured  $\bar{\nu}_p$  for the fission of  $^{232}\text{Th}$  nuclei by neutrons in the energy range 1.3-6.35 MeV (see Table 1). The measurement technique has been described in detail in [10, 11]. A set of sixteen  $^3\text{He}$ -filled counters mounted in a polyethylene moderator was used as the neutron detector. The nuclear fission events were recorded by an ionization chamber which comprised six sections with ten double-face layers in each. The layers with a thickness of 1.0 mg/cm<sup>2</sup> and a diameter of 30 mm were made from thorium dioxide. In order to obtain monoenergetic neutrons, the T(p, n) and D(d, n) reactions were used. The protons and deuterons were accelerated by an electrostatic accelerator operated in the steady mode. The error in the neutron energy

TABLE 1. Results of the  $\bar{\nu}_p$  Measurements in the Fission of  $^{232}\text{Th}$  Nuclei by Neutrons

Neutron energy, MeV	$\bar{\nu}_p$	Statistical error	Neutron energy, MeV	$\bar{\nu}_p$	Statistical error
1.35	2,194	0,022	2,70	2,234	0,024
1,50	2,208	0,019	2,80	2,200	0,027
1,60	2,142	0,022	2,90	2,232	0,027
1,70	2,145	0,020	3,00	2,233	0,025
1,80	2,155	0,024	3,10	2,274	0,021
1,90	2,169	0,020	3,20	2,276	0,019
2,00	2,215	0,015	3,30	2,270	0,030
2,10	2,202	0,019	3,40	2,328	0,022
2,15	2,224	0,022	3,50	2,316	0,027
2,20	2,213	0,024	3,60	2,310	0,026
2,30	2,223	0,025	3,70	2,387	0,044
2,40	2,185	0,020	5,60	2,683	0,030
2,50	2,226	0,031	5,90	2,689	0,022
2,60	2,232	0,026	6,35	2,887	0,026

Translated from Atomnaya Énergiya, Vol. 54, No. 3, pp. 209-211, March, 1983. Original article submitted July 12, 1982.

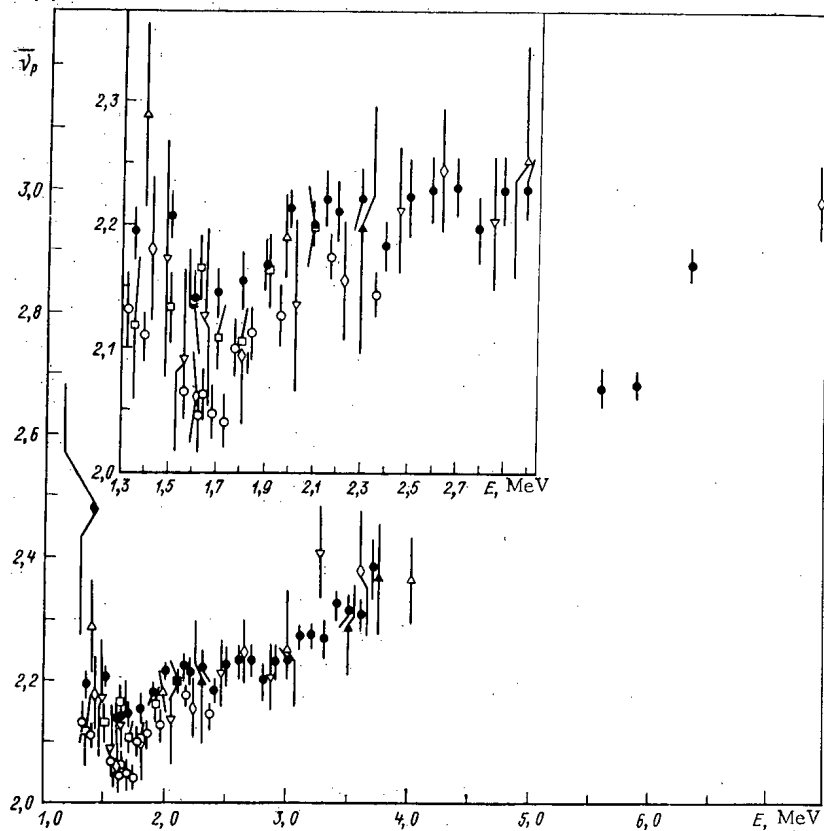


Fig. 1. Measurement of  $\bar{\nu}_p$  in the fission of  $^{232}\text{Th}$  by neutrons: ● our work; ▲ [1]; ◆ [2]; × [3]; ◇ [4]; Δ [5]; ▽ [6]; □ [7]; ○ [8].

was 30-40 keV at energies of up to 3.7 MeV and about 80 keV in the energy range 5-6 MeV. The  $\bar{\nu}_p$  measurements on  $^{232}\text{Th}$  were made relative to the value  $\bar{\nu}_p = 3.733$  in the spontaneous fission of  $^{252}\text{Cf}$ .

The meaning of the various corrections in terms of physics and the manner in which the corrections are brought into account in the results of the  $\bar{\nu}_p$  measurements have been previously described in [10, 11]. We modified only the manner of obtaining corrections which are associated with the incomplete recording of fission events. For this purpose the results of special investigations were used. The correction resulting from the amplitude discrimination of the pulses caused by fission fragments amounted in our work to  $(1.1 \pm 0.3)\%$ ; the correction which is associated with the loss of fragments in the layer undergoing fission was  $(0.4 \pm 0.1)\%$ . The results of our work and of the previous work of [1-8] is compared in Fig. 1, which also displays the statistical error of the measurements.

Despite the rather broad spread of the data shown in Fig. 1, a complicated energy dependence of  $\bar{\nu}_p$  is observed in the neutron energy range of 1.3-6 MeV. Of particular interest is the decrease in  $\bar{\nu}_p$  at increasing neutron energies near the fission threshold. This means that the fraction of the fission energy spent in the emission of neutrons decreases in proportion to the increase in the excitation energy of the nucleus undergoing fission, i.e., the fission energy is redistributed between the excitation energy and the kinetic energy of the fission fragments.

#### LITERATURE CITED

1. B. D. Kuz'minov, L. S. Kutsaeva, and I. I. Bondarenko, *At. Energ.*, **4**, No. 2, 187 (1958); B. D. Kuz'minov, in: *Neutron Physics* [in Russian], Atomizdat, Moscow (1971), p. 241.
2. A. Smith, R. Nobles, and S. Cox, *Phys. Rev.*, **115**, 1242 (1959).
3. J. Meadows and J. Whalen, *Rep. WASH-1033*, Vol. 2 (1961).
4. H. Conde and M. Holmberg, *Arkiv. Fys.*, **29**, 33 (1965).
5. D. Mather, P. Fieldhouse, and A. Moat, *Nucl. Phys.*, **66**, 149 (1965).
6. L. I. Prokhorova and G. N. Smirenkin, *Yad. Fiz.*, **7**, 961 (1968).
7. J. Caruana, J. Boldeman, and R. Walsh, *Nucl. Phys.*, **A285**, 217 (1977).

8. J. Trochon et al., Rep. Tenth Europ. Conf. on Physics and Chemistry of Complex Nuclear Reactions, Lillehammer (1981).
9. V. G. Vorob'eva and V. V. Malinovskii, Preprint FÉI-1124, Obninsk (1980).
10. V. G. Vorob'eva et al., Problems of Atomic Science and Technology, Series: Nuclear Constants [in Russian], No. 3(38), 44 (1980).
11. V. V. Malinovskii et al., Energy Dependence of the Average Number of Prompt Neutrons in the Fission of  $^{236}\text{U}$  by Neutrons [in Russian], Rep. of the Twelfth Conf. of the International Committee on Nuclear Data, Vienna, October 5-9 (1981). INDC/P(81)-47.

## ADJUSTMENT OF THE NEUTRON FLUX WITH THE AID OF ADSORPTION SYSTEMS

I. G. Gverdtsiteli, A. G. Kalandarishvili,  
M. N. Korotenko, S. D. Krivonosov,  
A. V. Nikonov, and N. N. Parkhomenko

UDC 621.039.515

The present work is a continuation of investigations concerning the adjustment of the thermal-neutron flux density in experimental channels of research reactors by means of sorption and desorption processes involving neutron-absorbing substances on neutron-transparent sorbents [1, 2].

The selection of materials to be used as sorbent and sorbate depends upon a number of thermodynamic and nuclear-physics constants and particularly upon the fact that the efficiency in the use of various sorption pairs is restricted to certain temperature intervals. The adsorption pair alkali metal-pyrolytic graphite proposed in [1] is efficient only in a too-high temperature interval (800-1000°K). In the selection of a sorption pair, it was attempted to reduce the interval of operational temperatures, and materials with a large absorption cross section of thermal neutrons were used as sorbates. Since cadmium [2] solves only the second part of the problem, the present work deals with results of research for using boron trifluoride as adsorbate. This makes it possible to reduce the interval of operational temperatures to 300-550°K and to obtain a large absorption cross section of thermal neutrons by the boron which is present in the adsorbate.

The investigations were made on the VVR-M reactor of the Institute of Nuclear Research of the Academy of Sciences of the Ukrainian SSR in a vertical channel which is situated in the beryllium reflector; a special tube with the adsorption pair: activated carbon-boron trifluoride (enriched with 92.2%  $^{10}\text{B}$ ) was employed.

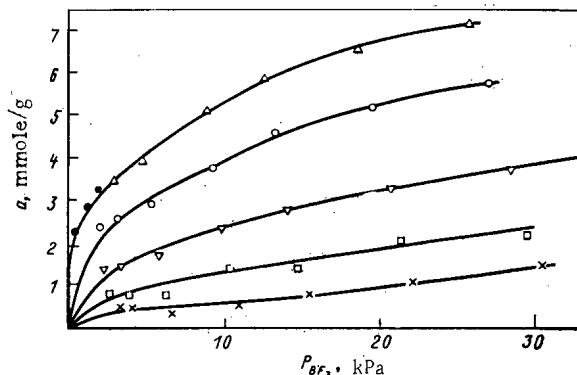


Fig. 1. Dependence of the adsorbed amount of boron trifluoride (1 mmole gas per gram activated carbon) upon the adsorbate pressure at the adsorbent temperature 290 ( $\Delta$ ,  $\bullet$ ); 330 ( $\circ$ ); 380 ( $\nabla$ ); 430 ( $\square$ ); and 485 °K ( $\times$ ).

Translated from *Atomnaya Énergiya*, Vol. 54, No. 3, pp. 211-212, March, 1983. Original article submitted July 16, 1982.

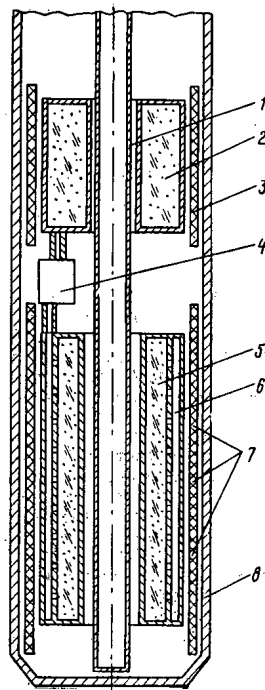


Fig. 2

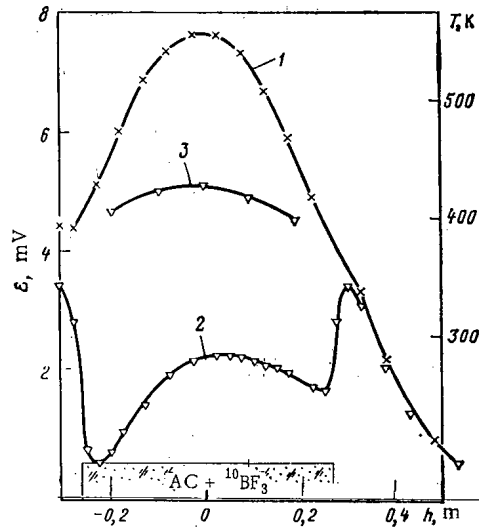


Fig. 3

Fig. 2. Scheme of the experimental sealed tube for regulating the neutron flux with an activated carbon-boron trifluoride ( $AC + {}^{10}BF_3$ ) system.

Fig. 3. Relative distribution of the neutrons over the height of the experimental channel: 1) with pure adsorbent; 2) after adsorption by boron trifluoride; 3) temperature distribution over the height of the regulator.

Before the reactor experiment, the adsorption isotherms of  $BF_3$  on activated carbon (Fig. 1) had been studied with a weighing method. This made it possible to select the necessary temperature conditions in the testing of the sealed tube. In the tests with the sealed tube, the neutron distribution at a thermal power of 1 MW of the reactor and at various concentrations of the boron trifluoride adsorbed on the activated carbon (filling the cavity of regulation) had to be measured. The neutron distribution was measured in the central tube of the channel with three techniques: moving a detector of direct charging, moving a sensor of thermal neutrons, and foil activation at various points distributed over the reactor core.

The sealed tube (Fig. 2) consisted of a central tube 1, a neutron-flux regulator 5, a boron trifluoride supply 2, a remote-control valve 4 protected by housing 8 and inserted between the regulator and the supply, and a temperature-regulating and checking system for the various components, the system having the form of electric heaters 3, 7 and a Chromel-Alumel thermocouple. The neutron-flux regulator was a cylinder with two coaxial cavities; one of the cavities (cavity 5) was filled with activated SKT-2 carbon (layer thickness 12 mm, density  $0.62 \text{ g/cm}^3$ ); the second cavity (cavity 6) served as the gas duct for the boron trifluoride. The neutron-flux regulator with the activated carbon was degassed at  $700^\circ\text{K}$  to a vacuum of 0.01 Pa and thereafter hermetically sealed. The adsorbate supply had the form of a hollow cylinder filled with the same amount of activated carbon as the regulator. After evacuation, boron trifluoride was adsorbed on the activated carbon of the supply to a concentration of 0.18 g trifluoride per gram activated carbon; after that, the supply was hermetically sealed. After measuring the initial neutron distribution and opening the remote-control valve, communication between the neutron-flux regulator and the adsorbate supply was established. A direct-charging detector was attached to the outer surface of the housing for measuring the neutron flux in the cell. The concentration of the boron trifluoride in the regulator was determined by measuring the equilibrium absorption concentration in dependence upon the temperature of both the regulator and the supply.

The measured distribution of the thermal-neutron flux density over the height of the experimental channel is depicted in Fig. 3. Curve 1 corresponds to the initial distribution measured with a thermal-neutron sensor with a sensitivity of  $6.2 \cdot 10^{-15} \text{ W} \cdot \text{cm}^2 \cdot \text{sec}/\text{neutron}$ . The neutron distribution (curve 2) was measured at an average

temperature of the regulator of 410°K. In this case the supply temperature was 360°K. The temperature distribution over the mantle of the regulator is represented by curve 3. The value 0.057 was obtained for the specific concentration of boron trifluoride adsorbed in the regulator; the quantity was determined from the condition that the BF<sub>3</sub> mass in the sealed tube must be constant over the adsorption isotherms. It was therefore possible to obtain a fourfold attenuation of the neutron flux relative to a uniform distribution over a path length of ~ 0.35 m. This confirmed that boron trifluoride is uniformly adsorbed on large quantities of the carbon. The slightly increased attenuation of the neutron flux in the region  $h = -0.2$  m seems to result from an increased layer density in the lower part of the regulator, wherein small carbon granules accumulate.

The neutron distributions determined with the aid of the direct charging detector and the thermal-neutron sensor over the height of the experimental channel are in good agreement except for sections with an increased gradient of the neutron flux density because, owing to the length of the sensor, the signal of the thermal-neutron sensor is an average signal over a length of 0.1 m.

Calculations have shown that after 100 h of continuous operation with an average thermal-neutron flux density of  $2 \cdot 10^{13}$  neutrons/(cm<sup>2</sup> · sec), the <sup>10</sup>B burnout amounts to 2.8% and to 24.4% after 1000 h. The burnout can be fully compensated for by a corresponding decrease in adsorbent temperature in the regulator or by an increase in adsorbent temperature in the supply. The latter implies an additional BF<sub>3</sub> adsorption in the regulator.

The pressure increase developing in the regulator from the reaction  $^{10}\text{BF}_3 + {}_0n' \rightarrow {}^7\text{Li} + {}^4\text{He} + 3\text{F}$  during 100 h irradiation time at the nominal power and an attenuation of 0.5 in a layer thickness of 1 cm amounts to 80 kPa, and to 700 kPa after 1000 h. Since the gas generated is distributed over the entire volume of the regulator system (this volume exceeds the activated-carbon volume in the regulator several times), in which the reaction takes place, the pressure in the system must be correspondingly reduced, i.e., for compensating for the pressure increase in the regulator one need not take special measures before a safe life of about 1000 h. The work capacity and efficiency of the neutron-flux regulating system based on the sorption pair activated carbon-boron trifluoride was therefore experimentally confirmed.

#### LITERATURE CITED

1. I. G. Gverdsiteli et al., *At. Energ.*, 48, No. 3, 187 (1980).
2. I. G. Gverdsiteli et al., *At. Energ.*, 53, No. 1, 36 (1982).

#### <sup>169</sup>Yb GAMMA SOURCES

A. V. Klinov A. V. Mamelin,  
and Yu. G. Toporov

UDC 621.039.8.002: 621.039.554

Because of its large output and high resolving power,  $\gamma$  flaw detection holds a firm position among methods of nondestructive testing, and the range of its application is being extended to more and more new classes of materials and products. To make  $\gamma$  flaw detectors highly effective it is necessary to produce specialized radiation sources with characteristics appropriate to the requirements of a specific problem.

Among the promising  $\gamma$  sources for detecting flaws in articles made of light alloys is <sup>169</sup>Yb, which emits low average energy  $\gamma$  rays (~ 93 keV) and has an acceptable half-life of 32 days [1]. For such a source to be practically useful, however, it must produce a high flux from a small volume, or in other words, it must have a specific activity of at least 100 TBq/q.\* It thus becomes necessary to determine how to optimize the conditions for the accumulation of <sup>169</sup>Yb.

The radionuclide <sup>169</sup>Yb is formed in the radiative capture of reactor neutrons by <sup>168</sup>Yb (in practice a mixture of Yb isotopes enriched in <sup>168</sup>Yb is used). Both the starting and accumulated nuclides have large capture cross sections for thermal neutrons and a pronounced resonance in the cross section in the epithermal region [2]. This means that an adequate prediction of the <sup>169</sup>Yb accumulation and the choice of irradiation regimes

\* 1 TBq =  $10^{12}$  Bq.

Translated from *Atomnaya Énergiya*, Vol. 54, No. 3, pp. 212-213, March, 1983. Original article submitted July 16, 1982.

TABLE 1. Two-Group Constants of Ytterbium Isotopes

Isotope	Cross section (b *) for neutron energy 0.0253 eV	Resonance integral $I_{\infty}$ for infinite dilution, b ( $E_{gr} =$ 0.215 eV)
$^{168}\text{Yb}$	$2200 \pm 170$	$24000 \pm 3000$
$^{169}\text{Yb}$	$3600 \pm 300$	$3500 \pm 500$

\*  $1 \text{ b} = 10^{-28} \text{ m}^2$ .

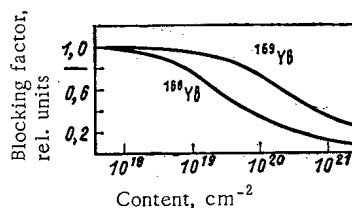


Fig. 1. Dependence of  $K_{b,l}$  of  $^{168}\text{Yb}$  and  $^{169}\text{Yb}$  on isotopic content of source.

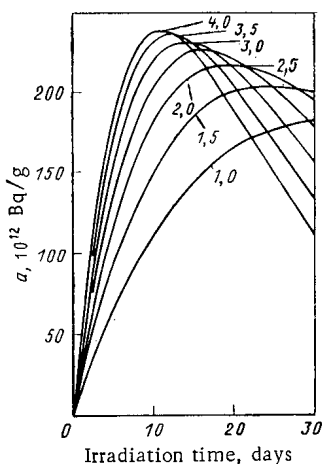


Fig. 2. Specific activity  $a$  of  $^{169}\text{Yb}$  as a function of irradiation time. Numbers on curves are values of thermal neutron flux  $\phi_T$ ,  $10^{14}$  neutrons/ $(\text{cm}^2 \cdot \text{sec})$ .

requires taking account of the burnup of the radionuclide formed and of the self-shielding of the irradiated material.

The accumulation of  $^{169}\text{Yb}$  was calculated with a computer program for the numerical solution of the system of differential equations describing the variation of the number of nuclei of the nuclides in the irradiation process. The nuclear reaction rates were calculated in the two-group approximation, using the constants (Table 1) obtained from data in [2]. The values of the effective resonance integrals of the ytterbium isotopes as a function of the isotopic concentration in the sample were calculated in the intermediate resonance approximation [3], taking account of the Doppler effect. Figure 1 shows the dependence of the blocking factors  $K_{b,l} = I_{\text{eff}}/I_{\infty}$  for  $^{168}\text{Yb}$  and  $^{169}\text{Yb}$  on the isotopic content of the source at  $300^\circ\text{K}$  calculated with resonance parameters from [2]. The initial content of  $^{168}\text{Yb}$  in the source was  $2.8 \cdot 10^{10} \text{ cm}^{-2}$ .

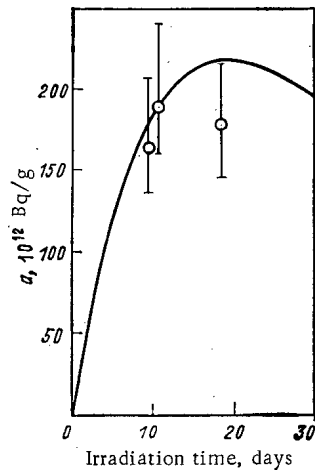


Fig. 3. Calculated and experimental data on the accumulation of Yb in a reflector channel of the SM-2 reactor.

The calculated values of the accumulation of  $^{169}\text{Yb}$  in facilities with various thermal neutron fluxes are shown in Fig. 2. The hardness index of the neutron spectrum (the ratio of the epithermal neutron flux per unit lethargy to the thermal neutron flux) was taken equal to 0.04, which corresponds to the typical neutron spectrum in irradiation channels in the beryllium reflector of the SM-2 reactor. The results obtained show that:

the irradiation time for maximum  $^{169}\text{Yb}$  yield decreases with increasing neutron flux;

the absolute value of the maximum yield of the radionuclide exceeds 150 TBq/g, and is insensitive to a change in the neutron flux in the range considered.

For an experimental test of the calculations, we irradiated several batches of preparations of sources in a channel of the beryllium reflector of the SM-2 reactor, where the thermal neutron flux  $\phi_T = 2 \cdot 10^{14}$  neutrons/(cm<sup>2</sup>·sec). The  $^{169}\text{Yb}$  activity was determined by measuring the  $\gamma$  spectrum of the source radiation, and took the value of the  $^{169}\text{Yb}$   $\gamma$  constant equal to 0.2 nA·m<sup>2</sup>/(kg·GBq) [1]. Figure 3 shows that there is satisfactory agreement of the experimental and calculated values. An estimate of the accuracy of the calculations must take account of the fact that the errors in the two-group cross sections of the Yb isotopes are  $\sim 10\%$ . The more than 150 TBq/g  $^{169}\text{Yb}$  activity attained opens up the possibility of the practical utilization of these sources in  $\gamma$  flow detectors.

#### LITERATURE CITED

1. Yu. V. Khol'nov et al., Radiation Characteristics of Radioactive Nuclides Use in the National Economy (Handbook) [in Russian], Atomizdat, Moscow (1980).
2. V. A. Anufriev et al., At. Energ., 49, No. 2, 116 (1980).
3. R. Goldstein, Nucl. Sci. Eng., 48, 248 (1972).

COMPARISON OF THE ONE-GROUP CONSTANTS OF THE ACTINIDES  
IN A TEST MODEL OF A FAST REACTOR

A. I. Voropaev, V. V. Vozyakov,  
A. I. Zinin, and A. G. Tsikunov

UDC 621.039.51

In 1979 the European-American Committee on Reactor Physics (NEACRP) proposed to carry out a comparison of the nuclear data of the actinides, used in physics calculations of fast reactors in different countries and mainly determining the radiation characteristics of irradiated and regenerated fuel.

The participants proposed the calculation of the one-group fission and radiative capture cross sections for 16 actinides at the center of the core of a two-dimensional test model of a fast reactor with a capacity of 1200 MW (elec.). Earlier, based on this model, the principal physical parameters determining the economics and safety of planned fast reactors were compared (critical loading, breeding, control and safety system efficiency, Doppler effect, etc.). [1].

Systematization of the results, presented from six countries, was carried out by specialists of the German Federal Republic [2]. The nuclear data libraries used by the participants for the calculations were: Great Britain - FGL-5; USA - ENDF/B-V; France - Carnaval-4; Federal Republic of Germany - KEDAK-3, and Japan - JENDL-2.

In the calculations of the Soviet Union, the nuclear data for  $^{235}\text{U}$ ,  $^{238}\text{U}$ ,  $^{239}\text{Pu}$ ,  $^{240}\text{Pu}$ ,  $^{241}\text{Pu}$ , and  $^{242}\text{Pu}$  correspond to the data of the BNAB-78 system of constants, and the constants for the other nuclides correspond to the recommendations of [3]. This constant guarantee is being used now in the Physicopower Institute for solving physics problems associated with the external fuel cycle of fast reactors. The normalized group fluxes, by which the cross sections have been averaged, calculated by a two-dimensional diffusion program, occurring in the block of programs for the complex calculation of fast reactors [4], are:

Energy	Neutron flux	Energy	Neutron flux
10,5-6,5 MeV	0,0015	21,5-10	0,0831
6,5-4	0,0088	10-4,65	0,0488
4-2,5	0,0215	4,65-2,15	0,0133
2,5-1,4	0,0415	2,15-1	0,0240
1,4-0,8	0,0511	1-0,465	0,0119
0,8-0,4	0,1264	465-215 eV	0,0033
0,4-0,2	0,1436	215-100	0,0389
0,2-0,1	0,1564	100-46,5	0,0313
100-46,5 keV	0,1479	46,5-21,5	0,0421
46,5-21,5	0,1153	21,5-10	0,051

TABLE 1. One-Group Fission Cross Sections of the Actinides at the Center of the Core of a Fast Reactor Two-Dimensional Test Model, b

Country	$^{234}\text{U}$	$^{235}\text{U}$	$^{238}\text{U}$	$^{238}\text{U}$	$^{237}\text{Np}$	$^{238}\text{Pu}$	$^{239}\text{Pu}$	$^{240}\text{Pu}$	$^{241}\text{Pu}$	$^{242}\text{Pu}$	$^{241}\text{Am}$	$^{242}\text{Am}$	$^{243}\text{Am}$	$^{242}\text{Cm}$	$^{243}\text{Cm}$	$^{244}\text{Cm}$
Soviet Union	0,31	2,08	0,095	0,039	0,31	1,13	1,90	0,36	2,65	0,22	0,27	3,20	0,21	0,16	2,4	0,40
Great Britain	0,29	1,98	0,088	0,043	0,31	1,13	1,83	0,35	2,69	0,22	0,31	3,33	0,19	1,23	2,9	0,38
USA	0,32	2,00	0,099	0,040	0,32	1,14	1,86	0,36	2,63	0,25	0,28	3,61	0,22		2,8	0,40
France	0,30	1,94	0,092	0,040	0,33	0,84	1,81	0,33	2,53	0,22	0,29	3,70	0,20	2,05	3,4	0,45
Federal Republic of Germany		2,00		0,041	0,32	1,03	1,87	0,36	2,54	0,24	0,26	3,86	0,20		2,5	0,43
Japan		2,10		0,045		1,12	1,88	0,37	2,61	0,28	0,30		0,23			0,43
Average for foreign laboratories	0,30	2,00	0,093	0,042	0,32	1,05	1,85	0,35	2,60	0,24	0,29	3,62	0,21	1,64	2,9	0,42

Translated from Atomnaya Energiya, Vol. 54, No. 3, pp. 214-215, March, 1983. Original article submitted August 2, 1982.

TABLE 2. One-Group Radiative Capture Cross Sections of the Actinides at the Center of the Core of a Fast Reactor Two-Dimensional Test Model, b

Country	<sup>234</sup> U	<sup>235</sup> U	<sup>238</sup> U	<sup>238</sup> U	<sup>237</sup> Np	<sup>238</sup> Pu	<sup>239</sup> Pu	<sup>240</sup> Pu	<sup>241</sup> Pu	<sup>242</sup> Pu	<sup>241</sup> Am	<sup>242</sup> Am	<sup>243</sup> Am	<sup>242</sup> Cm	<sup>243</sup> Cm	<sup>244</sup> Cm
Soviet Union	0,66	0,63	0,60	0,31	1,70	0,81	0,58	0,62	0,50	0,52	1,91	0,46	1,76	0,42	0,36	0,93
Great Britain	0,61	0,53	0,59	0,29	1,95	0,45	0,55	0,63	0,62	0,39	2,01	0,11	1,73	0,51	0,10	0,49
USA	0,66	0,62	0,61	0,31	1,86	0,80	0,57	0,61	0,50	0,48	1,89	0,10	1,20		0,27	0,91
France Federal Republic of Germany	0,35	0,59	0,51	0,29	1,44	0,54	0,57	0,55	0,50	0,63	2,02	0,70	1,60	0,59	0,50	0,85
Japan		0,60		0,31	1,64	0,68	0,57	0,57	0,50	0,50	1,93	0,46	1,53		0,18	0,65
Average for foreign laboratories		0,64		0,31		0,91	0,61	0,62	0,55	0,41	1,69		1,65			0,66
	0,54	0,60	0,57	0,30	1,72	0,68	0,57	0,60	0,53	0,48	1,91	0,34	1,54	0,55	0,26	0,71

The results of the comparison of the calculations from all the participants are presented in Tables 1 and 2. The following conclusions can be drawn from the results presented:

1. The constants for the fission and radiative capture cross sections of the principal actinides, used in the Physicopower Institute, on the whole coincide well with the recent estimates of ENDF/B-V and JENDL-2.
2. There is a significant spread in the data for <sup>242</sup>Am and curium isotopes.
3. When solving problems associated with the external fuel cycle of fast reactors, reliable data about the (n, 2n) reaction cross sections of plutonium and neptunium are essential. It is desirable to also carry out a representative comparison of these data.

## LITERATURE CITED

1. A. I. Voropaev et al., At. Energ., 48, No. 6, 356 (1980).
2. H. Küsters, in: Proceedings of an International Conference on Nuclear Cross Sections for Technology, Knoxville, USA, October 22-26, 1979, NBS-595 (1980).
3. A. P. Voropaev et al., Problems of Nuclear Science and Technology. Series Nuclear Constants [in Russian], No. 3 (1979), p. 34.
4. A. P. Zinin et al., Mathematical Model of a Fast Reactor, Preprint FÉI-1086, Obninsk (1980).

## PURIFICATION OF THE BR-10 SODIUM COOLANT FROM CESIUM RADIONUCLIDES

V. P. Vaizer, I. A. Efimov,  
É. E. Konovalov, A. I. Lastov,  
and V. S. Shereshkov

UDC 621.039.534...24: 621.039.738

During the operation of fast reactors it has been established that the radioactivity of the sodium coolant of the primary circuit after the decay of  $^{24}\text{Na}$  is determined mainly by  $^{22}\text{Na}$  and  $^{137}\text{Cs}$ . The activity of the latter can exceed the activity of  $^{22}\text{Na}$  by an order or more, and can exceed that of the corrosion products by several times. The contribution of  $^{137}\text{Cs}$   $\gamma$  radiation to the exposed dose intensity from the sodium pipelines and the plant of the primary circuit of the shut-down reactor can attain 90% of the total dose from fission and corrosion products. Therefore, the purification of the sodium coolant from radionuclides of cesium is of great practical importance. As applicable to the problem posed, it is most advantageous to use the capability of cesium to form layer compounds with graphite - graphitides. This unique solution, proposed for the first time in [1-3], already has attained practical realization [4, 5].

In the present paper, the results of laboratory investigations of the interaction of cesium impurities in the sodium with different graphites and other materials and the results of tests of traps for the purification of the BR-10 sodium coolant from radionuclides of sodium are described. The laboratory investigations were conducted in static isothermal conditions. For this the equilibrium distribution coefficients of  $^{137}\text{Cs}$  between the sodium melt and the materials being investigated were measured:  $K = A_s/A_{\text{liq}}$  ( $\text{m}^3/\text{kg}$ ), where  $A_s$  and  $A_{\text{liq}}$  are the specific activities of  $^{137}\text{Cs}$  in the solid ( $\text{Bq}/\text{kg}$ ) and liquid ( $\text{Bq}/\text{m}^3$ ) phases. The results of the isothermal tests are presented below, illustrating the capability of different materials to absorb cesium radionuclides from the sodium melt. The equilibrium distribution coefficients of  $^{137}\text{Cs}$  in the systems sodium-graphitic materials and sodium-sorbents at  $300^\circ\text{C}$ ,  $\text{m}^3/\text{kg}$ , are shown:

Activated carbons (BUA, KAD, AR-3, SKT) . . . . .	2.2-4.3
Vitreous carbon SU-200. . . . .	4.5
Graphite gauze . . . . .	2.8
Graphite ARV . . . . .	6.3 ( $260^\circ\text{C}$ )
Reactor graphite . . . . .	0.72
Isotropic pyrographite:	
low density . . . . .	3.1
high density . . . . .	1.9
Anisotropic graphite, high density . . . . .	0.86
Pyrographite MPG-8 . . . . .	8.3 ( $230^\circ\text{C}$ )
Pyrographite MPG-6 . . . . .	23.0
Alumogel AG-100 . . . . .	0.40
Zeolite (NaA, NaX, CaA, CaX) . . . . .	0.22-0.28
Metal-ceramic nickel filter, pore size $12\ \mu\text{m}$ . . . . .	0.01

In the experiments the cesium concentration in the sodium melt did not exceed  $10^{-5}$  mass %. It can be seen from the data given that graphitic materials are the most efficient absorbers of cesium.

The results of nonisothermal investigations of the interaction between  $^{137}\text{Cs}$  and pyrographites and vitreous graphite are represented in Fig. 1. Interaction takes place by a chemisorption mechanism. The presence of a maximum confirms the participation of activation processes in the absorption [6]. It follows from the course of the curves in Fig. 1 that the optimum temperature of the graphite in cesium traps should not exceed  $250\text{-}300^\circ\text{C}$ . Above it, the distribution coefficient decreases in accordance with the requirements of thermodynamics.

It is advantageous to use the most simple forms of graphitic materials as the sorbent for a cesium trap - pyrographites or vitreous carbon - in order to reduce to a minimum the loss of carbon particles into the sodium

Translated from *Atomnaya Énergiya*, Vol. 54, No. 3, pp. 215-216, March, 1983. Original article submitted August 9, 1982.

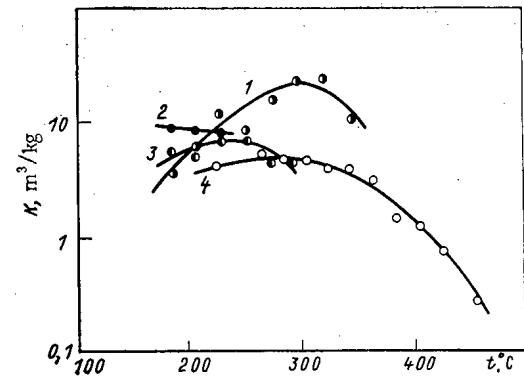


Fig. 1. Temperature dependence of the distribution coefficients of <sup>137</sup>Cs between sodium and MPG-6 (●); MPG-8 (●); SU-200 (●); and PGI (○).

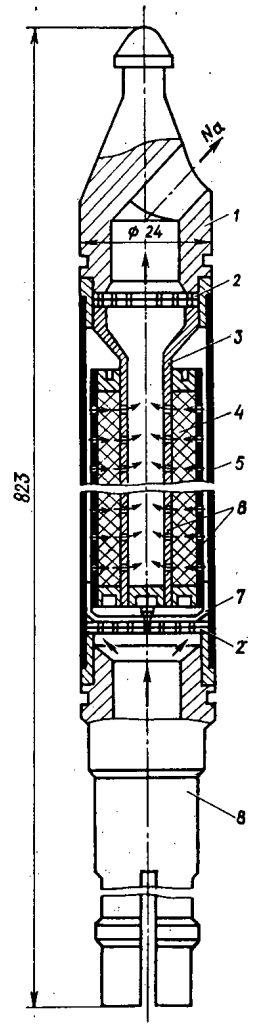


Fig. 2. Filter-trap for cesium radionuclides of the BR-10 reactor: 1) cap; 2) filter gauze; 3) cone; 4) carbon material; 5) housing; 6) perforated tubes; 7) centering retainer; 8) shaft.

coolant. It is known that the alkali metals reduce the strength of graphite [7]. This phenomenon is related with the Rebinder effect: The mechanical strength of solid materials is reduced by the action of surface-active substances. The particles of graphite, carried into the coolant stream, can serve as carriers of cesium radionuclides, and also develop chemical activity in the hot sections of the circuit.

For the reactor investigations of the sorption of radionuclides, including  $^{137}\text{Cs}$  and  $^{134}\text{Cs}$ , and also for the improvement of maintenance work conditions on the pipelines and plant of the BR-10 primary circuit, purification of the sodium coolant was carried out by means of traps filled with isotropic pyrographite (PGI) and SKT-6. In the development of the design of the traps and the carrying out of work on the purification of the coolant, the experiments of similar work on the BOR-60 [4] was extremely useful. The traps (Fig. 2) were installed in the central channel of the BR-10, having an autonomous coolant feed, instead of the experimental fuel-element assembly. For this purpose, the cap and shaft of a normal fuel-element assembly were used in the design, and instead of the hexagonal fuel-element assembly, a tube with a diameter of 24 mm was used. The sorbent being tested was located between two perforated tubes with diameters of 20 and 8 mm at a height of 550 mm. The sodium entered the trap from below and passed through the layer of sorbent in the radial direction to the central tube. Having moved through it upwards, the sodium exited through an opening in the cap and was mixed with the normal flow from the core.

The investigations were conducted before shutdown of the reactor for thorough overhaul. The volume of sodium in the primary circuit amounted to  $1.65 \text{ m}^3$ , the temperature of the sodium and sorbent was  $240^\circ\text{C}$ , and the coolant flow rate through the trap was  $1.0 \text{ m}^3/\text{h}$ , which corresponded to a rate of sodium filtration through the sorbent of 2.2 to 5 cm/sec. The traps with pyrographite and activated carbon were installed alternately in the central channel. The mass of sorbent in the traps amounted to 140.5 and 61 g, respectively. For this the multiplicities of the sodium exchange were 100 and 81. The  $\gamma$ -radiation dose intensity at the surface of the primary-circuit pipelines before the start of the experiment attained  $400 \mu\text{R}/\text{sec}$  ( $1 \text{ R} = 2.58 \cdot 10^{-4} \text{ C}/\text{kg}$ ), and 50% was due to  $^{137}\text{Cs}$  and  $^{134}\text{Cs}$ , and 30% to  $^{22}\text{Na}$ . The initial concentrations of  $^{137}\text{Cs}$  were  $1.7 \cdot 10^8$  and  $1.3 \cdot 10^7$  Bq/kg sodium, respectively.

In addition to purification of the sodium coolant, at the end of the experiments the walls of the primary circuit were partially cleansed from radioactive cesium. By switching on the electrical heating, the temperature of the primary circuit was raised to  $340\text{--}370^\circ\text{C}$ , and the cesium trap with activated carbon continued to function at a temperature of  $240^\circ\text{C}$ . In consequence of this, part of the radioactive cesium was transferred from the walls of the circuit into the trap - approximately 1.2 Ci ( $1 \text{ Ci} = 3.700 \cdot 10^{10} \text{ Bq}$ ), which amounted to more than one half of the radioactive cesium existing on the walls of the circuit. A gamma-scan of the extracted traps over the height of the sorption layer showed that the design of the trap with radial filtration ensures a quite uniform distribution of the activity over its height.

In the case of purification of the coolant with the traps with pyrographite PGI and with carbon SKT-6, the  $\gamma$ -radiation dose intensity was reduced by a factor of 3, and the contribution to it of cesium radionuclides was reduced by a factor of 10. After purification the contribution to the dose intensity from cesium radionuclides became less than the contribution from corrosion products by a factor of five, and became an order less than the contribution from  $^{22}\text{Na}$ . Purification of the coolant allowed the concentration of  $^{137}\text{Cs}$  to be reduced by a factor of 18. When analyzing samples of sodium before and after purification, it was found that its filtration through carbonaceous sorbents during 180 h was not accompanied by an increase of the content of carbon in the coolant (limit of carbon detection was  $4 \cdot 10^{-6}$ ).

Based on the experiments on the BR-10, a provisional estimate was made of the amount of graphitic materials necessary for a tenfold reduction of the concentration of cesium radionuclides in the primary circuit of the BN-600. The calculation showed that for conditions similar to those used in the BR-10, 10 kg of pyrographite PGI are required in one or several traps.

#### LITERATURE CITED

1. J. Clifford, *Trans. Am. Nucl. Soc.*, 10, 1, 336 (1967).
2. J. Clifford, J. Williams, and J. McCuir, in: *Proceedings of an IAEA Symposium "Behavior of Fission Products in Sodium"*, Alkali Metal Coolants, Vienna, 759 (1967).
3. W. Clough and S. Wade, *J. Nucl. Energy*, 25, No. 9, 445 (1971).
4. N. V. Krasnoyarov, V. I. Polyakov, and Yu. V. Chechetkin, in: *Proceedings of an International Conference on Liquid-Metal Technology in Energy Production*, Champion, USA, 30 (1976).

5. W. Olsen and M. Ruthe, Nucl. Technol., 46, No. 2, 318 (1979).
6. A. A. Zhukhovitskii and L. A. Shvartsman, Physical Chemistry [in Russian], Metallurgiya, Moscow (1976), p. 296.
7. P. A. Rebinder, Surface Phenomena in Dispersed Systems. Physicochemical Mechanics. Selected Papers [in Russian], Nauka, Moscow (1979), p. 222.

**MEASUREMENT TECHNIQUES**

*Izmeritel'naya Tekhnika*  
Vol. 25, 1982 (12 issues) ..... \$400

**MECHANICS OF COMPOSITE MATERIALS**

*Mekhanika Kompozitnykh Materialov*  
Vol. 18, 1982 (6 issues) ..... \$330

**METAL SCIENCE AND HEAT TREATMENT**

*Metallovedenie i Termicheskaya Obrabotka Metallov*  
Vol. 24, 1982 (12 issues) ..... \$420

**METALLURGIST**

*Metallurg*  
Vol. 26, 1982 (12 issues) ..... \$435

**PROBLEMS OF INFORMATION TRANSMISSION**

*Problemy Peredachi Informatsii*  
Vol. 18, 1982 (4 issues) ..... \$320

**PROGRAMMING AND COMPUTER SOFTWARE**

*Programmirovaniye*  
Vol. 8, 1982 (6 issues) ..... \$135

**PROTECTION OF METALS**

*Zashchita Metallov*  
Vol. 18, 1982 (6 issues) ..... \$380

**RADIOPHYSICS AND QUANTUM ELECTRONICS**

*Izvestiya Vysshikh Uchebnykh Zavedenii, Radiofizika*  
Vol. 25, 1982 (12 issues) ..... \$400

**REFRACTORIES**

*Ogneupory*  
Vol. 23, 1982 (12 issues) ..... \$380

**SIBIRIAN MATHEMATICAL JOURNAL**

*Sibirskii Matematicheskii Zhurnal*  
Vol. 23, 1982 (6 issues) ..... \$495

**SOIL MECHANICS AND FOUNDATION ENGINEERING**

*Osnovaniya, Fundamenty i Mekhanika Gruntov*  
Vol. 19, 1982 (6 issues) ..... \$380

**SOLAR SYSTEM RESEARCH**

*Astronomicheskii Vestnik*  
Vol. 16, 1982 (4 issues) ..... \$275

**SOVIET APPLIED MECHANICS**

*Prikladnaya Mekhanika*  
Vol. 18, 1982 (12 issues) ..... \$400

**SOVIET ATOMIC ENERGY**

*Atomnaya Energiya*  
Vols. 52-53 (12 issues) ..... \$440

**SOVIET JOURNAL OF GLASS PHYSICS AND CHEMISTRY**

*Fizika i Khimiya Stekla*  
Vol. 8, 1982 (6 issues) ..... \$175

**SOVIET JOURNAL OF NONDESTRUCTIVE TESTING**

*Defektoskopiya*  
Vol. 18, 1982 (12 issues) ..... \$485

**SOVIET MATERIALS SCIENCE**

*Fiziko-khimicheskaya Mekhanika Materialov*  
Vol. 18, 1982 (6 issues) ..... \$345

**SOVIET MICROELECTRONICS**

*Mikroelektronika*  
Vol. 11, 1982 (6 issues) ..... \$195

**SOVIET MINING SCIENCE**

*Fiziko-tekhnicheskie Problemy Razrabotki Poleznykh Iskopaemykh*  
Vol. 18, 1982 (6 issues) ..... \$420

**SOVIET PHYSICS JOURNAL**

*Izvestiya Vysshikh Uchebnykh Zavedenii, Fizika*  
Vol. 25, 1982 (12 issues) ..... \$400

**SOVIET POWDER METALLURGY AND METAL CERAMICS**

*Poroshkovaya Metallurgiya*  
Vol. 21, 1982 (12 issues) ..... \$435

**STRENGTH OF MATERIALS**

*Problemy Prochnosti*  
Vol. 14, 1982 (12 issues) ..... \$495

**THEORETICAL AND MATHEMATICAL PHYSICS**

*Teoreticheskaya i Matematicheskaya Fizika*  
Vols. 50-53, 1982 (12 issues) ..... \$380

**UKRAINIAN MATHEMATICAL JOURNAL**

*Ukrainskii Matematicheskii Zhurnal*  
Vol. 34, 1982 (6 issues) ..... \$380

Send for Your Free Examination Copy

Plenum Publishing Corporation, 233 Spring St., New York, N.Y. 10013

In United Kingdom: 88/90 Middlesex St., London E1 7EZ, England

Prices slightly higher outside the U.S. Prices subject to change without notice.

# RUSSIAN JOURNALS IN THE PHYSICAL AND MATHEMATICAL SCIENCES

AVAILABLE IN ENGLISH TRANSLATION

## ALGEBRA AND LOGIC

*Algebra i Logika*

Vol. 21, 1982 (6 issues) ..... \$270

## ASTROPHYSICS

*Astrofizika*

Vol. 18, 1982 (4 issues) ..... \$320

## AUTOMATION AND REMOTE CONTROL

*Avtomatika i Telemekhanika*

Vol. 43, 1982 (24 issues) ..... \$495

## COMBUSTION, EXPLOSION, AND SHOCK WAVES

*Fizika Goreniya i Vzryva*

Vol. 18, 1982 (6 issues) ..... \$345

## COSMIC RESEARCH

*Kosmicheskie Issledovaniya*

Vol. 20, 1982 (6 issues) ..... \$425

## CYBERNETICS

*Kibernetika*

Vol. 18, 1982 (6 issues) ..... \$345

## DIFFERENTIAL EQUATIONS

*Differentsial'nye Uravneniya*

Vol. 18, 1982 (12 issues) ..... \$395

## DOKLADY BIOPHYSICS

*Doklady Akademii Nauk SSSR*

Vols. 262-267, 1982 (2 issues) ..... \$145

## FLUID DYNAMICS

*Izvestiya Akademii Nauk SSSR,*

*Mekhanika Zhidkosti i Gaza*

Vol. 17, 1982 (6 issues) ..... \$380

## FUNCTIONAL ANALYSIS AND ITS APPLICATIONS

*Funktsional'nyi Analiz i Egò Prilozheniya*

Vol. 16, 1982 (4 issues) ..... \$320

## GLASS AND CERAMICS

*Steklo i Keramika*

Vol. 39, 1982 (6 issues) ..... \$460

## HIGH TEMPERATURE

*Teplofizika Vysokikh Temperatur*

Vol. 20, 1982 (6 issues) ..... \$400

## HYDROTECHNICAL CONSTRUCTION

*Gidrotekhnicheskoe Stroitel'stvo*

Vol. 16, 1982 (12 issues) ..... \$305

## INDUSTRIAL LABORATORY

*Zavodskaya Laboratoriya*

Vol. 48, 1982 (12 issues) ..... \$400

## INSTRUMENTS AND EXPERIMENTAL TECHNIQUES

*Pribory i Tekhnika Éksperimenta*

Vol. 25, 1982 (12 issues) ..... \$460

## JOURNAL OF APPLIED MECHANICS AND TECHNICAL PHYSICS

*Zhurnal Prikladnoi Mekhaniki i Tekhnicheskoi Fiziki*

Vol. 23, 1982 (6 issues) ..... \$420

## JOURNAL OF APPLIED SPECTROSCOPY

*Zhurnal Prikladnoi Spektroskopii*

Vols. 36-37 (12 issues) ..... \$420

## JOURNAL OF ENGINEERING PHYSICS

*Inzhenerno-fizicheskii Zhurnal*

Vols. 42-43, 1982 (12 issues) ..... \$420

## JOURNAL OF SOVIET LASER RESEARCH

*A translation of articles based on the best Soviet research in the field of lasers*

Vol. 3, 1982 (4 issues) ..... \$95

## JOURNAL OF SOVIET MATHEMATICS

*A translation of Itogi Nauki i Tekhniki and Zapiski Nauchnykh Seminarov Leningradskogo Otdeleniya Matematicheskogo Instituta im. V. A. Steklova AN SSSR*

Vols. 18-20, 1982 (18 issues) ..... \$680

## LITHOLOGY AND MINERAL RESOURCES

*Litologiya i Poleznye Iskopaemye*

Vol. 17, 1982 (6 issues) ..... \$420

## LITHUANIAN MATHEMATICAL JOURNAL

*Litovskii Matematicheskii Sbornik*

Vol. 22, 1982 (4 issues) ..... \$205

## MAGNETOHYDRODYNAMICS

*Magnitnaya Gidrodinamika*

Vol. 18, 1982 (4 issues) ..... \$325

## MATHEMATICAL NOTES

*Matematicheskie Zametki*

Vols. 31-32, 1982 (12 issues) ..... \$400

continued on inside back cover